Numerical Simulations of Rotating Stall in Axial Flow Compressors

Yan-Ling Li

Department of Engineering and Design

University of Sussex

A thesis submitted for the degree of

Doctor of Philosophy

September 2013

Declaration

The work presented in this thesis is, to the best of the candidate's knowledge and belief, original and the candidate's own work, except as acknowledged in the text. The material has not been submitted, either in whole or in part, for a degree or comparable award of University of Sussex or any other university or institution.

Author _____

Yan-Ling Li

Date _____

UNIVERSITY OF SUSSEX

Yanling Li, Doctor of Philosophy

Numerical Simulations of Rotating Stall in Axial Flow Compressors

Summary

Gas turbine compressor performance may encounter deterioration during service for various reasons such as damage by debris from the casing or foreign objects impacting on the blades, typically near the rotor's tip. Moreover, mal-schedule of Variable Stator Vanes (VSVs) during start-up may also result in performance deterioration and reduction in the surge margin. Ability to assess the effect of compressor deterioration using Computational Fluid Dynamics (CFD) is important at both design stage and in service. Compressor blade damage breaks the cyclic symmetry and the VSVs mal-schecule creates mis-match between stages together with geometric variations, thus computations are desirable to be performed using full annulus assemblies. Furthermore, downstream boundary conditions are also unknown during rotating stall or surge and simulations become difficult.

This research presents unsteady time-accurate CFD analyses of compressor performance with tip curl blade damage in a single stage axial flow compressor and VSVs mal-schedule in a 3.5 stage axial flow compressor. Computations were performed near stall boundary to predict rotating stall characteristics. The primary objectives are to characterise the overall compressor performance and analyse the detailed flow behaviour. Computations for the nominal blade configurations were

also performed for comparison purposes for both compressors. All unsteady simulations were performed at part speeds with a variable nozzle downstream representing an experimental throttle.

For the blade damage study, two different degrees of damage for one blade and multiple damaged blades were investigated and compared with the results from the undamaged case. For the VSVs mal-schedule study, the first two stators were assumed to be variable and were used to create mal-schedule vane settings for the investigation. The effects of blade damage and VSVs mal-schedule on the aerodynamics performance and rotating stall characteristics for both compressor assemblies were investigated respectively and discussed in detail.

Acknowledgements

Firstly, I would like to express my great gratitude to my principal supervisor Professor Abdulnaser Sayma for his technical and non-technical support throughout my time at University of Sussex. He substantially influenced the direction of my work and taught me so much during the many in-depth discussions, and also for being so understanding of my situation as an international student. I am extremely thankful, he continued to offer his support and encouragement during the final stage of this work, after he took up an academic post at City University London.

I would like to thank Dr Zhijun Peng as he kindly agreed to act as my official supervisor for a short period before he took up an academic post at University of Hertfordshire after Naser's move. Thanks are due to Dr Zhiyin Yang who kindly agreed to act as my supervisor for the short period after Dr Peng's move. Special thanks are due to Dr Herwart Honen from RWTH Aachen University for providing the IDAC compressor geometry and experimental data. I would like to thank Dr Shaobin Li who was a visiting fellow in 2011 at University of Sussex from Beihang University, China. He kindly provided the CFX steady state solutions of the IDAC compressor for the VSVs mal-schedule study in this research. He also provided very valuable discussions in compressor aerodynamics and CFD simulations.

I would like to thank Dr Xia Hao for valuable discussions we had about CFD simulations. Thanks are due to Dr Vasudevan Kanjirakkad with whom I had valuable discussions about compressor aerodynamics and instabilities. I would also like to thank my colleague Mr Pascal Nucara for the interesting discussions we had and Mr Harri Koivisto a colleague who always gave me useful advice and support throughout my studies. Special thanks to all other staff in TFMRC who gave me non-academic support. The financial support of University of Sussex funding this project is gratefully acknowledged.

I would like to dedicate this thesis to my parents and friends who supported me in the long journey, especially for my father's financial and non-financial support throughout my studies.

Contents

List of Figures

List of Tables

Nomenclature

Greek Symbols

$\Delta\tau$	pseudo-time step
Γ	boundary of the control volume
γ	constant specific heat ratio
μ	total viscosity of the fluid
Ω	control volume
ω	rotational speed of rotor bladerow
ρ	fluid density
σ	viscous stress tensor

Subscripts

δ_{ij}	Kronecker delta function
μ_l	molecular viscosity
μ_t	turbulent eddy viscosity
Ω_I	area of the control volume constructed by connecting the dual median of the cells surrounding node I
I,J_1,...,J_n	node index in the mesh
n_S	number of sides connected to node I

Pr_l	laminar Prandtl number
Pr_t	turbulent Prandtl number
$\mathbf{B}_i$	boundary integral
$\mathbf{F}_{IJ_S}$	inviscid fluxes along side IJ_S
$\mathbf{G}_{IJ_S}$	viscid fluxes along side IJ_S
$\mathbf{S}_I$	rotational source term at node I
$\mathbf{U}_\tau$	pseudo-time derivative term
$\mathbf{U}_I$	solution vector at node I
η_{IJ_S}	side weight

Other Symbols

e	specific total energy of the fluid
H	total enthalpy of the fluid
n	time level
p	pressure of the fluid
x	rotational axis of the compressor
$\mathbf{F}$	inviscid flux vector
$\mathbf{G}$	viscous term
$\mathbf{n}$	outward normal unit vector of the control volume boundary Γ
$\mathbf{S}$	source term
$\mathbf{U}$	conservative variable
$\mathbf{u}$	absolute velocity of the flow

v	fluid velocity in the relative frame of reference

Acronyms / Abbreviations

CDA	controlled diffusion airfoils
CFD	computational fluid dynamics
DES	detached eddy simulation
FOD	foreign object damage
IDAC	inversely designed Aachen compressor
IP	intermediate pressure
LES	large eddy simulation
MCA	multiple circular arc
OGV	outlet guide vane
PR	total pressure ratio
RANS	Reynolds-Averaged Navier-Stokes
RWTH	Rheinisch-Westfalische Technische Hochschule
TFMRC	Thermo-Fluid Research Centre
TR	total temperature ratio
URANS	unsteady Reynolds-Averaged Navier-Stokes
VSVs	variable stator vanes

Chapter 1

Introduction

1.1 Background

Axial flow compressors are the principal type of compressors commonly used in gas turbines for aircraft and power generation. To meet the needs of gas turbines, the demanding requirements of axial flow compressors are high efficiency, high flow capacity within a relatively small structure, high pressure ratio, reasonable manufacturing costs, robustness and reliability. For a compressor in service, it is found to be difficult to maintain the originally designed aerodynamic performance when deterioration occurs (Levine [1998]). Compressor performance plays an important role in gas turbine engines. Any change could influence the efficiency and power output both of which are essential factors. It is normally characterised by a map in the form of pressure rise versus mass flow function as partially shown in Figure 1.1. The operating range of the compressor is bounded by the choke and surge boundaries as seen from the figure. It is well known that the region between the working line and surge line is defined as surge margin. Flow under most of the operating conditions on the map is normally steady, in the rotor's frame of reference, and axisymmetric.

As seen in Figure 1.1, the characteristic curve tends to be vertical at high flow, indicating the maximum mass flow going into the compressor which is also known as the choke boundary; at low flow, it tends to be more horizontal, indicating the maximum pressure rise with minimum mass flow in the compressor which is also

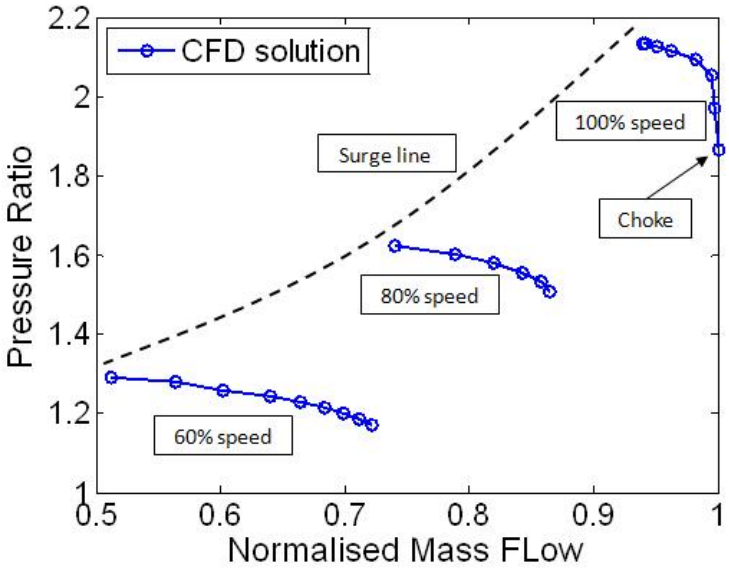

Figure 1.1: Axial flow compressor characteristics at given rotational speeds (NASA Rotor 37)

known as the surge boundary. When compressors operate near the surge boundary, mass flow is reduced and excessive positive incidences on the rotor blades occur. When the incidence reaches a critical value, instability may be encountered in the form of flow separation. If the situation becomes worse, it may lead to surge. Surge limits the maximum pressure ratio and minimum flow conditions for stable operation. It is a global phenomenon which is normally characterised by large mass flow rate fluctuation or flow reversal. There are two types of surge commonly reported in the literature: classic surge and deep surge. Classic surge normally occurs with large oscillation of mass flow being pressurised and unpressurised periodically. The latter one, deep surge, is a more severe phenomenon possibly with flow reversal. Deep surge is also typically manifested by high abnormal noise or flames reaching the inlet; in which case leading to compressor destruction as reported by Levine [1998]. More details regarding the classification of surge can be referred to Greitzer [1981] and de Jager [1995]. The degree of stability of the compressor is represented by the slope of the characteristic curve. As the slope of the tangent line of the curve tends to be zero, compressor stability diminishes and the flow tends to be unstable and the chance for surge increases.

Another phenomenon compressors normally encounter, rotating stall, will be the focus of this study. Rotating stall is normally found at compressor part-speeds during start-up process. It is normally the precursor of surge and the compressor could be in operation with rotating stall if a new equilibrium for the flow can be established. However, it is frequently accompanied with pulsating loads and extra blade vibrations due to stall cells rotating around the annulus. At extreme conditions, this can lead to component failure. Compared to surge, rotating stall is a localised phenomenon to a particular rotor or particular stages in which a compressor could operate without failure and may recover from. It commonly consists of one or more stall cells covering one or more blade passages that propagate in the same direction of the rotor rotation at some fraction of the shaft speed. The number of stall cells and the propagation speed may vary at different operating conditions in different compressors, but typically, the propagation speed is around half of the shaft speed.

The mechanisms of rotating stall initiation and its characteristics are still the subject of continuous scientific debate; however, for clarity it may be explained by reference to Figure 1.2. A localised flow perturbation could cause blade 2 to encounter higher positive incidence more than the neighbouring blades and the flow separates on its suction side lead to the formation of a stall cell which reduces the flow passing into the passage above that blade. This may occur either due to the impurity of the inflow, manufacturing tolerance or different numbers of blades in each bladerow. Then the blocked flow diverts flow around the blade so that the incidence increases on blade 1 and decreases on blade 3. This leads to the stall cell moving to the passage above blade 1. At a subsequent time, due to blockage above blade 1, blade 2 encounters lower positive incidence leading to the recovery of the passage above, while blade 1 will have higher positive incidence leading to stall in the passage above. This is the start of propagation of stall cells around the annulus. Therefore, a very strong reason to avoid rotating stall is the consequent blade excitation which may lead to high cycle fatigue damage as claimed by Walsh and Fletcher [2004].

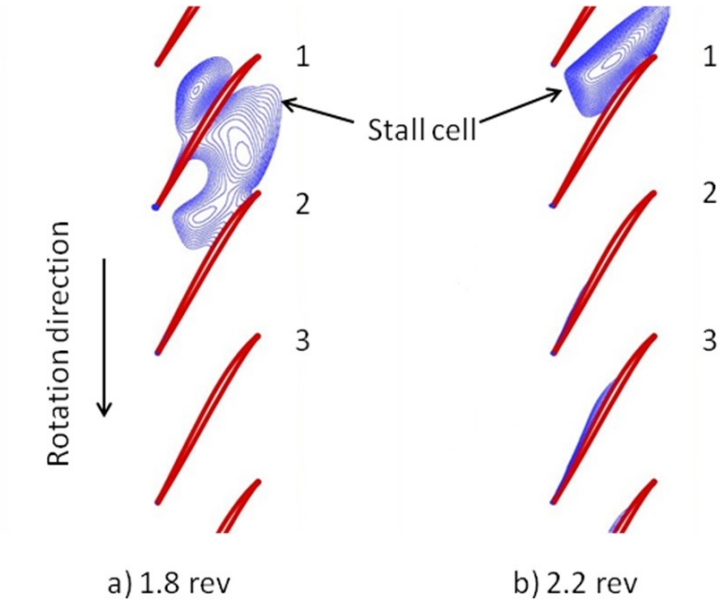

Figure 1.2: Propagation of rotating stall in NASA Rotor 37

As discussed above, surge and rotating stall are two common instability phenomena which compressors could encounter when they operate close to the surge line. There are various reasons which may cause compressor instabilities, for instance engine deterioration or Foreign Object Damage (FOD). Surge could be initiated from stall of compressor blades. Stall of compressor blades is caused by the flow separations on the suction sides of blades as mentioned above. When blades stall, flow through the compressor is blocked and becomes unstable. When the condition becomes worse, it may lead to a situation that the compressor can no longer provide pressure rise as expected. When the compressor reaches the deep surge condition, the compressed high-pressure reversal flow behind the stall goes forward through the compressor and out from the inlet. The whole process is usually fast, rapid and often quite audible along with a 'bang noise' in the engine. Engine surge can be accompanied by a visible flash forward out from the inlet.

Based on its characteristic on the compressor map, stall can be classified into two categories as reported by Gong [1999]: progressive or abrupt stall. For progressive stall, pressure ratio will drop gradually by reducing the mass flow. Rotating stall occurring consequently is normally formed of more than one stall cell in part span

pattern in the radial direction. On the other hand abrupt stall normally results from a discontinuous drop in pressure ratio and efficiency. Rotating stall observed in this case normally consisted of one single cell in full span pattern in the radial direction.

Based on inception condition, it has been observed that rotating stall can be initiated by two types of inception: the long length-scale or modal type and the short length-scale or spike type, which was reported by Camp and Day [1998]. They could be distinguished by the type of initial perturbation in static pressure or velocity signal. Modal inception normally has a small amplitude disturbance with long wavelength seen in the pressure/velocity time histories and needs a large number of revolutions to develop. With modal inception, stall cells can rotate at 30% to 50% of rotor speed. Spike inception normally has larger amplitudes in the initial perturbation with a propagation speed of stall cells at 70% to 80% of the rotor speed (Vo et al. [2008]).

As mentioned above, rotating stall could result from or be affected by compressor deterioration. Although investigations on rotating stall drew attention since the 1950's and a lot of work in this area has been done so far, surge and/or rotating stall continue to occur for the reasons listed below which are not exhaustive (Levine [1998]):

- Rotating stall due to Inlet Guide Vanes (IGV), Variable Stator Vanes (VSVs) and bleed valves that do not operate properly during start-up.
- Surge or stall due to deterioration of the compressor condition such as fouling, erosion and roughness.
- Surge or stall due to deterioration of the compressor condition such as blade damage caused by ice or foreign object injection.
- Surge due to operation beyond the recommended operating limits.

As a result of the limited time scale in this research, only blade damage effects and the effects of VSVs mal-schedule were investigated.

Compressor blades may encounter damage during service for various reasons such as loose casing liner, Foreign Object Damage (FOD) or ice formation at the intake. FOD from other sources, such as tire fragments, injection of bird (bird strike) and runaway debris or animals, may also be encountered. This may result in deterioration of the compressor performance and in extreme conditions, may cause compressor stall or surge. During the design process, it is important to be able to predict the aerodynamic behaviour of the compressor in such events to enable the design of robust blades capable of coping with these events.

During start-up process, the flow may pass through the regions of potential stall and beyond surge margin. For multi-stage compressors, flow condition is controlled during start-up by using Variable Inlet Guide Vanes (VIGVs) or VSVs and/or bleed valves to avoid compressor instabilities. By changing VSVs settings, it allows compressors to operate in a safe region on its characteristic map without stall or surge. In detail, during the start-up process, the flow density is low in the rear stages, resulting in a mismatch of the aerodynamic design which needs to avoid stall at all speeds. To overcome this mismatch, VSVs are commonly used to reduce the air flow at low speeds and thereby reduce the flow velocities in the rear stages to avoid stall and surge (Levine [1998]). Approaching the design point, VSVs are opened to allow more flow in to achieve the expected mass flow. Normally, the design schedule of VSVs is a function of corrected engine speed at different shaft speeds and ensure the compressor is operating near the peak efficiency region (Campbell [1958]). However, improper settings and malfunction of VSVs systems could lead to rotating stall or surge. The malfunction operation of VSVs will be termed as mal-schedule of VSVs in this thesis.

1.2 Objectives

In this thesis, issues regarding the effects of blade damage and mal-schedule of VSVs were investigated. As explained in the previous section, bird strikes or ice ingestion and FOD are common issues which could happen in aero engines. They may also

cause fan or compressor blade damage which may initiate rotating stall or surge. Although there were investigations published on blade damage effects on compressor performance, the influences from aerodynamics point of view have been overlooked. Meanwhile, VSVs are commonly used in front stages in multi-stage compressors. The control mechanism of VSVs may malfunction in some circumferences which could change the performance completely. There are very few investigations regarding the effects of VSVs mal-schedule on compressor aerodynamics and rotating stall characteristics. Therefore, the specific objectives in this research are:

1. To gain a fundamental understanding of the impact of blade damage on a single stage axial flow compressor aerodynamic performance and its rotating stall characteristics at off-design condition, in particular:
    - To investigate compressor performance and rotating stall characteristics with nominal blade settings.
    - To investigate effects of different degrees of one damaged blade on compressor performance and rotating stall characteristics.
    - To investigate effects of multiple damaged blades on compressor performance and rotating stall characteristics.
2. To investigate the effects of VSVs mal-schedule on the performance of a multi-stage axial flow compressor and its rotating stall characteristics, in particular:
    - To investigate whether steady state solutions close to stall boundary have precursors for potential stall.
    - To characterise compressor performance near stall boundary with nominal blade settings.
    - To investigate compressor performance at near stall boundary with VSVs mal-schedule which might provide information regarding the resilience of the compressor.

1.3 Contributions

The key contributions of this thesis are:

- Most of the work related to blade damage in the literature was performed on fan blades and/or investigations from aeroelasticity point of view. The effects on compressor aerodynamics performance and rotating stall characteristics have been overlooked. This thesis presents the first account of impact of compressor rotor blade damage on compressor aerodynamics performance and rotating stall characteristics. It was found that compressor assemblies with mild damage on the blade(s) do not have significant effects on the overall performance.

- There are very few studies regarding VSVs mal-schedule effects on compressor performance, as reviewed in Chapter 2. This thesis presents one of the first few accounts of the effects of VSVs mal-schedule on compressor aerodynamics performance and rotating stall characteristics, to improve understanding of the problem. It seemed that the assembly with VSVs mal-schedule was more stable than the one with nominal blade settings based on available data which do not represent the general case and requires further investigation.

1.4 Structure of the thesis

This thesis is divided into seven chapters, including this one which provides the background information and objectives of this research. A literature review will be presented in Chapter 2. Studies including experimental and numerical (mainly CFD related) on rotating stall have been reviewed. The physical mechanisms behind rotating stall of both modal and spike inception as proposed will be summarised as well. In chapter 3, the numerical methodology used in this research will be described and validated using a transonic axial flow compressor. Grid independence study has been also investigated to determine the suitable meshes for code validation and

unsteady analyses to compromise the accuracy of the solution and computing time needed.

The thesis consists of two main parts. The first part, the blade damage study, will be presented in Chapters 4 and 5. Before discussing blade damage effect near stall boundary, it is better to have the understanding of the flow behaviour without any damaged blade. Therefore, in Chapter 4, the unsteady simulation with nominal blade settings near stall boundary will be presented first. Then, in Chapter 5, the blade damage effects will be analysed, including different degrees of one damaged blade and multiple damaged blades with identical degree of damage. The second part of the thesis, VSVs mal-schedule effects, will be presented in Chapter 6. Two cases are compared in order to investigate the VSVs mal-schedule effect: compressor assemblies with nominal blade settings and VSVs mal-schedule. Finally, Chapter 7 summarises the main findings and the outcomes of this research. Suggestions for future work will then be provided based on the discussion and analyses from the results obtained.

1.5 Publications

Selected parts of this thesis have been published which is listed as the following paper:

- Part of the blade damage study was presented at the conference of ASME Turbo Expo 2012, Copenhagen, Denmark, 11-15 June 2012 (Li and Sayma [2012]).
- Part of the VSVs mal-schedule study was accepted for the conference of ASME Turbo Expo 2014, Dusseldorf, Germany, 16-20 June 2014 (Li and Sayma [2014]).

Chapter 2

Literature review

2.1 About this chapter

In this chapter, literature which is relevant to the objectives of this research will be reviewed. Firstly, studies including experimental and numerical (mainly CFD related) on rotating stall have been summarised. Both influencing factors which may cause rotating stall and investigations regarding the mechanisms of rotating stall are presented. Secondly, reviews of blade damage studies and VSVs studies are given separately. At the end, concluding remarks regarding the reviewed literatures are presented.

2.2 Rotating stall studies

There are two main routes for rotating stall studies in the literature: experimental and numerical, both will be included in this chapter. Within numerical studies, there are two commonly used methods: Computational Fluid Dynamics (CFD) and analytical method. In the past two decades CFD has become popular for the following reasons: 1) Full scale experiments are normally difficult and extremely expensive to perform; 2) Experiments are not possible at the design stage; 3) CFD could provide the flow details within the computational domain which may lead to a better understanding of the flow behaviour. Reviews on numerical work will be

focusing on CFD related issues which are relevant to this research. Thus, the relevant analytical work could be referred to Longley [1994], Greitzer [1976], Moore and Greitzer [1986], Greitzer and Moore [1986] and Abed et al. [1991] which will not be reviewed in this chapter. The review of experimental work provides understanding of the physics of the phenomenon. Although the work in this research is investigated using CFD, it is also worthwhile to understand rotating stall through experimental investigations. Rotating stall is observed either when the compressor operates close to stall boundary at specific rotational speed or it is caused by other features in the compressor such as inflow with foreign object injection.

Theoretically, studies on rotating stall could be divided into three aspects: 1) inception; 2) development; 3) fully developed pattern. Studies on rotating stall inception aim at finding the working mechanism and causes for rotating stall initiation. It is also important to find the indicators for rotating stall to help developing active control system for its avoidance. For information about rotating stall avoidance which is not the concern of this research, one can refer to the techniques on early stall warnings such as the work done by Tahara et al. [2004]; and stall detection systems, design of control or avoidance systems are also beyond the scope of this research. More information can be found in Bindl et al. [2009], Feulner et al. [1996], Schulze and Hennechke [1998] and Christensen et al. [2008].

In the next subsection, influencing factors or possible causes which could be responsible for rotating stall will be presented. Previous efforts which resulted in better understanding of the mechanisms of rotating stall are discussed afterwards.

2.2.1 Influencing factors

The early rotating stall studies date back to the 1950's. One of the early experiments was performed by Benser [1953] in a high pressure ratio multi-stage compressor at Lewis Flight Propulsion Laboratory. Part span rotating stall was observed. Results showed that the influence from stage interaction could result in performance discontinuities in later stages when rotating stall was observed in the inlet stage. Since

then, a large amount of work has been done such as rotating stall inception, criteria for two different types of rotating stall inception, flow behaviour during rotating stall and rotating stall avoidance or recovery systems. Despite that, the mechanisms of rotating stall are still with lack of understanding.

Rotating stall is commonly observed at lower rotational speeds (Lewis et al. [1954]) and is generally three dimensional in nature (Beknev et al. [1973]). That indicates 3D numerical simulations are necessary. A 3D unsteady Euler equations based solver was used by Nakano et al. [1999] because it was not possible to apply 3D unsteady Navier-stokes solver within the whole flow regions in multi-stage compressors with the capability of supercomputers at that time. Simulations were conducted at 100% speed to match the condition for the available experimental data. Results had a good agreement with the experimental data for the 6-stage transonic compressor. The 3D calculation was performed on the 3-stage transonic compressor and spike type disturbance was predicted as in the experiment. Results showed that three-dimensional simulations were necessary when rotating stall was initiated by short length scale disturbances.

Rotating stall is a very complex phenomenon because it could be affected by many factors. The testing environment is one factor which has significant effect on rotating stall characteristics. An experiment was carried out by Longley and Hynes [1990] using a refurbished C106 compressor at the Whittle Laboratory Cambridge University. The experiment aimed at finding out how much the compressor performance (characteristics) including stall was affected by the testing environment. A compressor stage was tested operating separately and also as a part of the whole compression system. Results showed that when the compressor stage operated both separately and with two identical downstream stages, the pressure ratio characteristic rise monotonically until stall; while when the compressor stages operated with two mismatched downstream stages, instability occurred at a much lower pressure ratio and mass flow. They also found out that the stall characteristic of a stage was affected by the whole compression system in multi-stage compressors. Therefore,

the rotating stall characteristic in an isolated rotor is different from the one when the rotor is part of the multi-stage compressor which indicates that to accurately investigate rotating stall in multi-stage compressors, a model of the whole compression system is desirable.

For isolated rotor stage test rigs, rotating stall is not only relying on the specifications of the rotor, but also the stator vanes located downstream. An experiment was carried out by Montgomery and Braun [1957] in a single stage compressor. Rotating stall was observed both with and without stator blades. With stator blades, it was found that there was less stall cells observed and rotating stall tended to occur at a higher mass flow. Thus, the stator used downstream would influence the rotating stall characteristics.

Another factor which may influence rotating stall is the stator/rotor gap. An experiment in a low speed compressor was conducted by Inoue et al. [2002]. The rotating stall process was similar for a large gap and a mild gap: first spike type rotating stall was observed and then it turned into modal wave rotating stall. For the small gap, it was initiated with modal wave rotating stall and then spike type rotating stall was observed; eventually it was formed to be a modal wave stall cell.

Boundary layers also have influence on rotating stall characteristics. As proposed by Lakhwani [1973], different boundary layers on the casing would lead to different stall patterns in an isolated rotor bladerow test rig. When the casing wall boundary layer was increased, rotating stall took place at higher mass flow rate and it was highly likely to obtain a progressive type stall. It was also found that the entry boundary layer thickness had no effect on the propagation speed of rotating stall. Choi et al. [2008] investigated the effects of inlet boundary layer thickness on rotating stall in an axial subsonic compressor using a three-dimensional numerical simulation. The in-house code is based on compressible Reynolds-Averaged Navier-Stokes (RANS) equations. The unsteady simulation was performed on a sector of the annulus which was two sevenths of total blade passages with 4.2 million nodes. It was found that the inlet boundary layer thickness had obvious effect on both the

flow coefficient at stall inception and the size of the rotating stall cell.

Rotating stall could be affected by the operating conditions as well, such as the rotational speed. A Rolls Royce VIPER Mk522 was tested by Freeman [1992] to study the inception of stall at a range of speeds and analyse the post stall behaviour. Part-span rotating stall was found when the compressor was operating at or below 62% of design speed and front stages were severely stalled. A 3D RANS code was used by Cai et al. [2004] to investigate rotating stall in a low speed fan. Results showed that the propagation speed of rotating stall cells depends on the compressor operating speed. Spanwise contour plots showed the flow detail which agrees with the experimental data. That also demonstrated the capability of accurately modelling rotating stall using CFD.

The effects of fan speed on rotating inception was also investigated by Choi et al. [2011] in an axial flow fan using an implicit, time-accurate 3D compressible RANS solver. The computational domain was simulated in a full annulus fashion at 70%, 80% and 90% speed. The fan speed was found to be a critical factor to determine the final pattern of rotating stall. When the fan speed was increased, the number of rotating stall cells was reduced and their size enlarged while the propagation speed was reduced. They reported that the flow incidence difference at different fan speed could be the reason for the different flow patterns.

Stall inception was investigated in full-scale engine tests by Hoss et al. [2000]. The engine used is a two-spool turbofan engine. Different types of stall precursor were found at different shaft speeds: spike-type at low speed and modal wave at mid-speed. At higher speeds, the rotor shaft imbalance was found to be the key to the stall inception.

Another factor that could be responsible for rotating stall is the radial loading distribution of rotor blades. The relevant effect on the stall inception pattern was investigated experimentally by Nie [2003] using a single stage low speed compressor. With low loading distributions near the tip regions, modal stall inception was observed; while high loading distributions near the tip regions would lead to spike

type inception. They also found that loading distributions near the hub regions had no effects on the stall inception pattern.

Effects of radial loadings on stall inceptions in a low speed compressor were also numerically and experimentally investigated by Zhang et al. [2009a]. Results showed that different radial loadings had significant effects on the stall limit. The compressor became more unstable when the distortion was closer to the blade tip. The position of radial distortion would lead to different rotating stall characteristics: hub distortion to modal inception rotating stall while centre and tip distortion to spike inception rotating stall.

Inflow conditions could also contribute to rotating stall inception. Experimental investigations on fourteen different stages from low speed compressor were performed by Cyrus [2000]. It was found that the rotor bladerow played the main role on the inception of rotating stall; and the onset was also affected by the stage inlet flow condition. Inlet distortion was also proved to be one of the causes of rotating stall by Lin et al. [2005] and Jiang et al. [2009]. The role of tip leakage flow under inlet distortion to trigger rotating stall was investigated by Zhang et al. [2009b]. It was also found that tip clearance flow played an important role in the development of stall regions near the casing in most of the cases. Due to the rotor-stator interaction influence, separations were also found in the stator bladerow near the casing. This also showed that stator downstream could influence the rotating stall characteristics.

Another important influencing factor is the tip clearance flow. The interaction of tip clearance flow with flow in adjacent blades could be one of the causes which lead to rotating stall as reported by Mailach et al. [2001]. A full annulus 3D time-accurate simulation was conducted on a compressor by Hah and Rabe [2001]. They found that rotating stall may be caused by the interaction of tip clearance vortex and passage shock. The role of tip clearance flow on stall inception was also numerically and experimentally investigated by Bennington and Du [2010] using a transonic compressor. It was believed by the authors that their work was also the validation for the spike inception criteria proposed by Vo et al. [2008]. The criteria related to

the role of tip clearance flow will be summarised in the next subsection.

The relationship between unsteady behaviour of tip leakage vortex and a rotating disturbance was numerically investigated by Yamada et al. [2008]. The simulation was performed on one ninth of the whole annulus with about 5.4 million points. Rotating disturbances were predicted to be initiated by the fluctuation of tip leakage flow in the rotor.

Flow injection can also contribute to inception of rotating stall. A time-accurate CFD code was used to simulate the stall inception in the compression system of the T700 engine used in Army Blackhawk Helicopeter in the US by Hathaway et al. [2004]. In that study a high speed compressor was investigated. The simulation used three bladerows which consist of an injector, a rotor and a stator bladerow. Two conditions were studied: one with injection and the other without injection. Stall inception was predicted under injection condition. With an injection of 5.9% of the design mass flow (20.34 kg/s), the results showed it can stabilise the unstable flow which may be responsible for the stall inception. Results showed that injection was one effective way to avoid rotating stall under certain conditions.

To sum up, rotating stall is three dimensional in nature and could depend on the testing environment, casing boundary layer thickness, operating condition such as rotational speed, radial loading distributions on rotor blades, inlet distortion, tip clearance flow and flow injection. Those made the phenomenon more complicated and less understood. In the next section, efforts which have been made to get better understanding of the mechanisms behind rotating stall will be presented.

2.2.2 Investigations of mechanisms of rotating stall

Although rotating stall characteristics would be distinct with different operating conditions in different compressors and could be affected by many factors, Day [1993] proposed that there were two types of rotating stall based on its inception route: modal-wave and spike type initiation. They can be distinguished by the type of initial disturbances in the unsteady pressure or velocity signals. Modal

inception normally has a small amplitude disturbance with long wavelength seen in the pressure/velocity time histories and needs a large number of revolutions to develop. Spike inception normally has larger amplitudes with a propagation speed of 70-80% of the rotor speed. Compared to modal wave rotating stall, spike type rotating stall is less understood which is the reason that many efforts have been devoted to investigate the mechanisms behind it. In this subsection, previous work will be reviewed in historical order.

In a multi-stage compressor, spike inception was highly likely to be observed in the first rotor as reported by Longley et al. [1996]. Also in multi-stage compressors, when rotating stall was found in the front stage(s), it would act as an inlet rotating distortion for the downstream stages and could influence their stability. On the other hand, it also suggested that the testing environment was important for the formation of rotating stall.

The spike type rotating stall was investigated both experimentally and numerically by Hah et al. [1999]. An unsteady time-accurate three-dimensional viscous Navier-Stokes code was used for the numerical simulations. The computation was performed on the full annulus of a low speed compressor which contained about 1.7 million nodes. A standard two-equation turbulence model was applied. Spike type inception was predicted from the unsteady simulation which matched the experiment. The propagation speed of rotating stall was between 60% to 80% of rotor speed which requires more accurate prediction. Results showed that the inception was very similar to the one observed from the experiment.The role of the local flow structures on rotating stall inception was unknown including tip clearance flow based on the available data.

A 2D unsteady Navier-Stokes simulation was conducted by Outa et al. [1999] for a compressor cascade stage of rotor and stator to investigate the evolution of rotating stall under uniform inlet conditions. An implicit time-marching scheme was applied in the solver. The stator stalled first and led to the formation of stall cells in the rotor. Rotating stall cells were mainly contained in a vortex upstream the

rotor and that caused a spike fluctuation in the inflow velocity. The limitation of 2D analysis was that the mass flow during rotating stall and stall cell from initial vortex were not correctly predicted. Also the 3D effects of the unsteady flow including tip clearance flow was excluded.

The propagation of spike type rotating stall cells in a low speed compressor was experimentally investigated by Inoue et al. [2000]. Under mild stall state, five rotating stall cells were observed with a rotating speed of approximately 72% of rotor speed. By throttling the compressor further, it turned to a modal wave with one large cell under deep stall condition with a rotating speed of 29% of rotor speed. The spike type rotating stall cell was formed a low pressure bubble with a leg travelling ahead of the rotor. The leg was linked to a blade suction surface while changing the blade in turn as the pressure bubble travelled. The mechanism was believed to be that the vortex leg broke down with the bubble and merged with a new one as it travelled.

Mechanisms of rotating instabilities in a low speed compressor was numerically and experimentally investigated by Marz et al. [2002]. The numerical simulation was performed on the full annulus of the compressor rotor without the downstream stator using a 3D time-accurate unsteady Navier-Stokes code. A modified two-equation turbulence model was used with wall function near the wall. The computational domain contained about 3.5 million nodes. Results showed that the code was able to capture similar flow behaviour as in the measurements. Results also showed that a rotating instability vortex was formed near the leading edge resulting from the interaction of tip clearance flow, axially reversed flow and the inflow. This was believed by the authors to be the precursor of the rotating stall.

Spike type rotating stall inception in a transonic compressor was experimentally investigated by Bergner et al. [2006]. When the compressor was operating near stall, unsteadiness showed a strong fluctuation of tip clearance flow; and the inception of rotating stall was believed to be initiated by the resulting spill forward of the tip clearance flow. The spike disturbances could be caused by the upstream motion

of one blade passages shock based on the available data. With the development of new techniques in experimental instrumentation, attempts have been made to investigate flow features inside rotating stall cells by Lepicovsky and Braunscheidel [2006]. Results showed that the measurement methodology used was capable to determine the unsteady flow parameters inside a rotating stall cell. It was also found that the compressor used which was operating at design speed had a rotating stall with one cell propagating at 50.6% of the rotor speed.

The stability of NASA Stage 35 was numerically investigated using a 3D unsteady CFD code by Chima [2006]. The code used is a multiblock Navier-Stokes solver which uses an explicit finite difference scheme. The Baldwin-Lomax turbulence model was used. Rotating stall with two part-span stall cells was observed from the unsteady simulation. It was shown that the code was capable of predicting rotating stall inception and its recovery. No detailed discussions regarding rotating characteristic and the relevant mechanism were provided.

A quasi 3D code based on solving the Navier-Stokes equations on stream surfaces was used by Gourdain et al. [2006a] to investigate rotating stall in an axial single stage low speed compressor. The Baldwin-Lomax turbulence model was used. Two rotating stall cells with a propagation speed of 48% of rotor speed were observed. Results showed that Baldwin-Lomax model could not predict the stability limit of the compressor accurately.

A full annulus unsteady 3D simulation was performed in a single stage low speed compressor by Gourdain et al. [2006b]. It was also validated by experimental measurements. The solver used solves the RANS equations using a finite volume method. The Sparlart-Allmaras turbulence model was used. The computational domain contained approximately 31 millions nodes. Two types of rotating stall were observed in this compressor stage with the same throttle parameter. The first was caused by the interaction between the tip clearance flow, in-passage separation vortex at mid-span and inflow. It had a propagation speed of 75% of the rotor speed. The second was the modal wave rotating stall which was observed later. The stall point

matched well with experiment, but the number of stall cells was not well predicted.

An experimental study of rotating stall inception was performed in a single stage low speed compressor by Simpson and Longley [2007]. Results showed that spike type inception could be correlated to the incidence in the tip region of the rotor blade. Both rotor geometry and the flow around it will determine the critical incidence for rotating stall inception.

Full annulus CFD simulations of pre-stall behaviour using NASA Stage 35 was performed by Chen et al. [2007] using high-performance parallel computations. The solver uses the unsteady Navier-Stokes equations with decoupled k-ϵ turbulence model. The computational domain contained about 67 million points and simulations were performed on an IBM P4 cluster using 328 CPUs for 24 hours. Spike type inception was predicted. The spike was caused by the interaction between the tip clearance vortex and the dual-shock flow structure in the passage. That study also demonstrated the capability of CFD methods to investigate this type of flow problems.

Criteria for spike type rotating stall were firstly proposed by Vo et al. [2008]. One criterion is that the interface between the tip clearance flow and the inflow becomes parallel to the leading edge plane of the rotor. The other one is the flow through some passages turns into the adjacent passages at the trailing edge of the blades. The work showed that their hypothesis agreed with all published observations of this type of rotating stall initiation in axial flow compressors at that time.

An investigation using Large Eddy Simulation (LES) was performed on a single passage model by Hah [2009] to investigate the mechanisms behind the spike type rotating stall inception in a transonic compressor. Their reason to use LES was to capture unsteady flow features which can not be accurately computed by RANS model. Non-reflecting boundary conditions were applied at the inlet and the exit boundaries. They found that when the compressor operated at the near stall condition, the unsteadiness was caused by the interaction between the tip clearance vortices and the in-passage shock. That also confirmed the theory proposed

by Bergner et al. [2006] which was also believed by the authors to be the natural phenomenon in a transonic compressor. When the in-passage shocks were fully detached from the leading edge, spike type rotating stall started. Results from LES simulations showed that flow features obtained were more close to the real flow physics for the single passage simulations. The numerical simulations agreed well with the measurements for the circumferential size of the rotating stall cell and its propagation speed. Due to the limitations of single passage simulations, it was not possible to know the number of rotating stall cells and their distributions.

An experimental investigation was conducted using the Notre Dame Transonic Axial Compressor by Bennington and Du [2010]. An interface between the tip-leakage flow and the incoming axial flow was observed. When the compressor was operating at near stall condition, that interface moved upstream and when it reached the leading edge of the rotor rotating stall was initiated. That confirmed the proposal by Vo et al. [2008].

Stall inception in a two-stage low-speed compressor was numerically and experimentally investigated by Tu et al. [2010] using 3D unsteady computations. The solver is based on three-dimensional unsteady Euler equations and the three-dimensional multi actuator-disks model. The simulation was performed on full annulus geometry. Results showed that stall cells were firstly observed in the second stage and the propagation speed of the fully developed stall cells were about 40.4% of rotor speed which agreed with the experimental data. However, the type of rotating stall could not be determined with the available data since the development of rotating stall happened within very short time according to the authors.

Rotating stall was simulated in the full annulus of a compressor stage using an URANS code by Gourdain et al. [2010]. The Spalart-Allmaras turbulence model was used because it was shown to be capable of providing a good compromise between cost and accuracy. By comparing with experimental data, it showed that the code was capable of predicting the phenomenon of spike type rotating stall. However, the number of rotating stall cells and their propagation speed were not correctly pre-

dicted. Also the development process was quite different which also needed further improvement on the code or inlet boundary conditions. That could be because the inlet boundary conditions for experiment were not well known and were different from the simulation.

The full annulus of an isolated rotor was numerically and experimentally investigated by Wu et al. [2011]. The solver is based on URANS methods. The Spalart-Allmaras was employed to calculate the eddy viscosity. The negative slope near stall boundary from the computational results indicated that spike type rotating stall inception could be encountered and that was also proved by the experimental data. The unsteady simulation also showed that spike type rotating stall was observed. It propagated at approximately 33.3% of rotor speed which matched with the experimental data. Each stall cell covered approximately 2-3 rotor pitches in the circumferential direction and less than 30% span in the radial direction. Features of rotating stall cell in both the circumferential and radial directions agreed well with the experimental data.

Numerical stall simulations were validated by Choi et al. [2011b] with experimental data at 60% and 95% of the shaft speed in a modern transonic fan. An implicit, time-accurate 3D compressible RANS solver was used. The numerical study was based on 3D unsteady full annulus simulations. When a fully developed spike initiated rotating stall was obtained in the simulation, solutions of mass flow rate, number of rotating stall cell and their propagation speed were well matched with the experimental data. It provided the confidence in using CFD simulations in this type of flows.

Detailed experimental measurements of spike-type rotating stall inception were presented by Weichert and Day [2012]. The measurements were done in a single stage compressor at the Whittle Laboratory Cambridge University. It was found that a radial vortex was involved in the spike inception. It also showed that with the development of instrumentation techniques experiments could reveal the flow better in the three dimensional sense which provides very good validation data for

CFD solutions. However, this type of measurements are still very expensive.

Pullan et al. [2012] tried to describe the evolution from spike inception to rotating stall and to explain the physical mechanism behind them from numerical simulations. Simulations were performed by using an unsteady RANS code with one-equation Spalart-Allmaras turbulence model. NASA E^3 rotor was used in their simulations. It was performed in 2D and 3D full annulus with and without tip clearance. All cases have similar general features that spikes were formed from flow separation near the blade leading edge on the suction side. It was also found that radial vortex was involved in the spike formation. The comparisons of all solutions and also with experimental data suggested that the spike formation did not necessarily depend on tip leakage flow in their cases.

The unsteady behaviour and three-dimensional flow structure spike-type stall inception in a low-speed compressor rotor was numerically and experimentally investigated by Yamada et al. [2012]. The in-house code solves 3D compressible Navier-Stokes equations using Detached Eddy Simulation (DES) for flow modelling. The numerical solutions showed that the spike disturbance was caused by a vortex which was caused by the separation at the leading edge near the rotor tip.

2.3 Blade damage studies

A literature search showed that there are very few published research work about flow behaviour in blade damaged compressors. Most of the available material concerns about fan blades damaged by bird strike. Bird impact analysis on aeroengine fan blades was investigated by Audic et al. [1999] without analyses of aerodynamics performance. A 3D simulation of a bird-damaged aero-engine fan assembly was investigated by Kim et al. [2001]. The fan assembly had two blades with different degrees of damage. The simulations were performed at two points on the compressor characteristic map which were at higher mass flow/lower pressure ratio and at lower mass flow/higher pressure ratio respectively. It was found that flutter stability was reduced and stall was observed at higher mass flow compared to the undamaged

fan.

Another investigation by Frischbier and Kraus [2005] using advanced numerical methods was reported on bird ingestion in a multiple stage turbofan. However, the results showed that the model had a considerable loss of accuracy with the mass flow of the low pressure compressor. Recent studies using the commercial code ANSYS/LS-DYNA by Meguid et al. [2008] and Guan et al. [2008] were about analysis of structural deformation of fan blades caused by bird strikes and no aerodynamics studies were attempted.

A study of the performance, forced response and surge caused by ice-damaged blades in Intermediate Pressure (IP) compressor assemblies were investigated by Dhandapani et al. [2008]. Results showed that surge margin was reduced by increasing the number of damaged blades and the severity of performance degradation depended on both the number of damaged blades and their distributions around the annulus. However, no information about unsteady flow simulation was presented in their paper.

An aerodynamics study of bird strike using NASA Rotor 67 was investigated by Bohari and Sayma [2010] using Computational Fluid Dynamics (CFD). Two damaged assemblies were simulated at different rotational speeds. It was found that the surge margin has deteriorated at higher rotational speeds and stall was found before the working line for both assemblies. No unsteady time accurate simulations for rotating stall were attempted.

2.4 Variable Stator Vanes studies

For given Variable Stator Vanes (VSVs) in a specific compressor, there is a limit of varying the range for their scheduling. In the XJ79-GE-1 turbojet engine, it was found by Campbell [1958] that when VSVs were closed halfway, the peak compressor efficiency was reduced by 0.02%. However, if the VSVs were further closed, the peak compressor efficiency would drop sharply. The net thrust was affected by closing VSVs slightly. While the specific fuel consumption can be only affected when VSVs

were closed more than halfway with significantly reduced compressor peak efficiency.

Kau [1998] proposed that the challenge of the VSVs system was the positional accuracy and hysteresis. And VSVs fault can be manual errors caused by installation and mal-function of the control system. Work has been done on fault diagnosis of VSVs system by Muir et al. [1989], Eustace et al. [1994], Merrington [1994] and Stamatic et al. [1990]. All of those works were focused on the development of techniques used to identify VSVs system fault without analyses of their effects on compressor aerodynamics effects.

Goebel et al. [2004] investigated few faults including sensor faults and actuator faults where an actuator was used to control the schedule of VSVs system. In their paper, those faults were chosen to be tested for general diagnostic techniques. It was found that if the VSVs failed in a fully open condition, the engine could not maintain its operability. If the VSVs failed in an inter-medium condition, the operation condition could be changed to cope with the situation which may keep the operability of the engine.

A 3D viscous time-accurate flow solver was used to model rotating stall and surge by Vahdati et al. [2008]. A variable-area nozzle was used at the back instead of a fixed back pressure. This model can simulate the steady flow near stall and can also represent a simplified axial surge event. It allows a total flow reversal. In the rotating stall case, rotating stall was induced by geometrically mis-tuning the rotor blade. The first three bladerows have variable-angle vanes using datum and mal-scheduled vane settings. The front nine bladerows were modelled in a whole-annulus fashion and the rest bladerows were modelled in a single passage fashion. It has a grid of 60 million points. After 13th revolutions, the variation of the static pressure upstream of rotor 1 showed that rotating stall was observed for the mal-scheduled case. There were about 10 to 13 rotating stall cells.

Effect of VSVs schedule on rotating stall inception in multi-stage compressor at part speed was numerically investigated by Peng [2011]. An eight-stage compressor was chosen for this study. VSVs were located at the front three stages. Spike type

rotating stall was observed from the unsteady simulation. It had 10 cells with a propagation speed of about 69% of rotor speed. However, the analysis was focused on structural behaviour rather than aerodynamic performance. It can be concluded that the aerodynamic effects and flow detail with blade damage and VSVs mal-schedule were overlooked.

2.5 Concluding remarks

The following points could be drawn from the above literature reviews that are most relevant to the current research:

1. Rotating stall in different types of compressors with different testing environments has been thoroughly studied both experimentally and numerically. Results show that rotating stall could be influenced by many factors. Amongst those, tip clearance flow seems to be one of the most important influencing factors commonly for hub-tip-ratio approximately 0.7 or lower. One of the criteria for spike type initiated rotating stall proposed by Vo et al. [2008] is that the interface between the incoming flow and tip clearance flow moves upstream and aligns with the leading edge plane of the rotor, i.e. spike type rotating stall could be initiated with one condition is that the flow separations blocked the entire passages near the tip of particular blades. In the past years, due to limitation of instrumentations it was not straightforward to investigate the role of tip clearance flow during rotating stall experimentally. It was recently shown by Weichert and Day [2012] that tip clearance flow can be characterised during stall inception by using sufficient instrumentation to achieve high spatial and temporal resolution. However, this type of experiments is far more expensive compared with CFD investigations. The work reported by Pullan et al. [2012] suggests that tip clearance flow is not necessary for spike formation in their cases. The reason could be that the compressors they investigated have a rather larger hub-to-tip ratio of approximately 0.85 and other design

parameters of the compressor could also be responsible for the flow features. To conclude, the consideration of tip clearance flow is potentially very important for the rotating stall investigations which has to be born in mind for the case studies.

2. It is concluded from the literatures that rotating stall investigations through CFD methods require the code to be capable of modelling flow separation and capturing time dependent unsteady flow features. CFD codes based on RANS equations together with the one equation Spalart-Allmaras turbulence model for calculating the eddy viscosity has been shown to be capable of simulating this type of phenomenon with good agreement with experimental data. They also provide a good compromise between solution accuracy and computational costs. Although attempts have been made to investigate rotating stall using Large Eddy Simulation (LES) or RANS together with Detached Eddy Simulation (DES), those are still not commonly applicable due to the fact that it requires large amount of storage and computing power. As discussed before, testing environments have significant effects on rotating stall characteristics. To truly represent rotating stall in a given compressor, the model of the whole compression system is desirable. This has to be taken into consideration, especially for rotating stall investigations in multi-stage compressors. The fast development in computing technology makes the large scale simulations possible through parallel computations.

3. As discussed in the background information in Chapter 1, blade damage and VSVs mal-schedule are common issues in compressor deterioration which could alter compressor performance. The designers should take these situations into account and compressors should be designed to be able to cope with them. However, with very few studies in the literature related to these matters as presented earlier, their effects on compressor aerodynamics performance are less understood.

Chapter 3

Numerical method and validation

3.1 About this chapter

In this chapter, validation of the in-house CFD code SURF is presented using a transonic axial compressor rotor. Firstly, the flow model used in this research is described. Secondly, grid independence study is performed to make sure that validation, done using experimental data, is not affected by the mesh quality. At the end, the numerical method is validated by comparing the results with the experimental data. All results presented in this chapter were obtained using steady state simulations.

3.2 Flow model

3.2.1 Governing equations

The unsteady, compressible Reynolds-averaged Navier-Stokes equations for a 3D bladerow rotating with angular velocity ω along the x-axis of an inertial Cartesian coordinate system which is also the absolute frame can be recast in terms of the absolute velocity $\mathbf{u}$ in a relative non-inertial reference frame rotating with the blade. The governing flow equations in the conservative compressible form for a control volume Ω with boundary Γ can be written as

$$\frac{d}{dt}\int_{\Omega}\mathbf{U}d\Omega + \oint_{\partial\Omega}(\mathbf{F} - \frac{1}{Re}\mathbf{G}) \bullet \mathbf{n}d\Gamma = \int_{\Omega}\mathbf{S}d\Omega \tag{3.1}$$

where $\mathbf{n}$ represents the outward normal unit vector of the control volume boundary Γ which is given by

$$\mathbf{n} = \begin{pmatrix} n_1 \\ n_2 \\ n_3 \end{pmatrix} \tag{3.2}$$

The solution vector of conservative variables $\mathbf{U}$ in Equation 3.1 is given by

$$\mathbf{U} = \begin{bmatrix} \rho \\ \rho\mathbf{u} \\ \rho e \end{bmatrix} \tag{3.3}$$

where ρ is the fluid density and e is the specific total energy.

The inviscid flux vector $\mathbf{F}$ in Equation 3.1 has the following components

$$\mathbf{F} = \mathbf{U}\mathbf{v} + \begin{bmatrix} 0 \\ p\delta_{ij} \\ u_j p \end{bmatrix} \tag{3.4}$$

where δ_{ij} represents the Kronecker delta function and $\mathbf{v}$ is the velocity in the relative frame of reference. p is the pressure which can be obtained from the following relations for ideal gas

$$p = (\gamma - 1)\rho[e - \frac{|\mathbf{u}|^2}{2}] \tag{3.5}$$

$$H = e + \frac{p}{\rho} \tag{3.6}$$

where γ is the constant specific heat ratio and H is the total enthalpy for the fluid.

The viscous term $\mathbf{G}$ in Equation 3.1 has been scaled by the reference Reynolds number for non-dimensionalization purposes and has the following components

$$\mathbf{G} = \begin{bmatrix} 0 \\ \\ \sigma_{ij} \\ \\ u_k\sigma_{ik} + \frac{\gamma}{\gamma-1}(\frac{\mu_l}{Pr_l} + \frac{\mu_t}{Pr_t})\frac{\partial T}{\partial x_i} \end{bmatrix} \tag{3.7}$$

where σ_{ij} is the viscous stress tensor. By applying the eddy viscosity concept, it is assumed that the turbulent stresses are proportional to the mean velocity gradient and the following relation can be obtained

$$\sigma_{ij} = \mu(\frac{\partial u_i}{\partial x_j} + \frac{\partial u_j}{\partial x_i}) + \lambda\delta_{ij}(\bigtriangledown \bullet \mathbf{u}) \tag{3.8}$$

μ_l in Equation 3.7 represents the molecular viscosity which is determined by the Sutherland's formula, while μ_t denotes the turbulent eddy viscosity which is why an appropriate turbulence model is needed. In this thesis, the eddy viscosity is calculated using the one-equation turbulence model of Sparlart and Allmaras (Spalart and Allmaras [1992]). As discussed in Chapter 2, it was shown that the model was adequate for compromising between the accuracy and computing time for rotating stall investigations. In Equation 3.8, $\mu = \mu_l + \mu_t$ is the total viscosity of the fluid.

The value of λ is related to μ by the Stokes relation $\lambda = -\frac{2}{3}\mu$. Pr_l is the laminar Prandtl number which is taken as 0.7 for air while the turbulent Prandtl number Pr_t is taken as 0.9.

The source term $\mathbf{S}$ on the right-hand side of Equation 3.1 is given by

$$\mathbf{S} = \begin{bmatrix} 0 \\ 0 \\ \rho\omega u_2 \\ \rho\omega u_3 \\ 0 \end{bmatrix} \tag{3.9}$$

Further details of the code with test cases are reported by Sayma et al. [2000a], [2000b] and [2000c].

3.2.2 Numerical discretisation

The three dimensional spatial domain is then discretised using semi-unstructured grids which apply unstructured meshes in the blade-to-blade direction and then they are connected in a structured manner in the radial direction. The mesh is represented using an edge based scheme with solution vector stored at the vertices of the computational mesh. In this approach, the code uses a mesh representation of node pairs connected by edges which will be illustrated on a 2D mesh for clarity purpose. Assume that node I is connected to the surrounding nodes $J_1, ..., J_n$ as shown in Figure 3.1. Then the semi-discrete form of Equation 3.1 for node I can be written as

$$\frac{d(\Omega_I \mathbf{U}_I)}{dt} + \sum_{S=1}^{n_S} \frac{1}{2} |\overrightarrow{\eta}_{IJ_S}| (\mathbf{F}_{IJ_S} - \mathbf{G}_{IJ_S}) + \mathbf{B}_i = \Omega_I \mathbf{S}_I \tag{3.10}$$

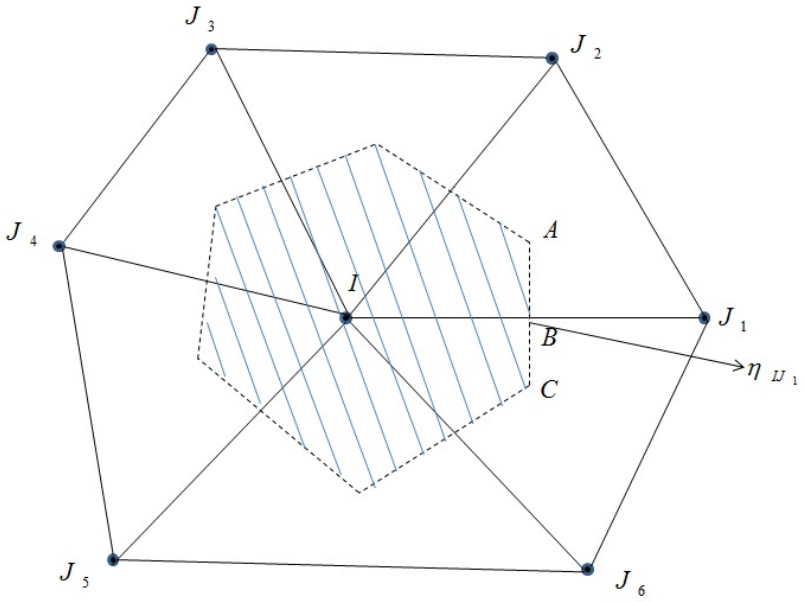

Figure 3.1: Typical 2D control volume

where Ω_I is the area of the control volume constructed by connecting the dual median of the cells surrounding node I (shaded area in Figure 3.1). $\mathbf{U}_I$ is the solution vector at node I. $\mathbf{S_I}$ is the rotational source term at node I. n_S is the number of sides connected to node I. $\overrightarrow{\eta}_{IJ_S}$ is the side weight which is given by the summation of the two dual median lengths around the side times their normals. $\mathbf{F}_{IJ_S}$ and $\mathbf{G}_{IJ_S}$ are the inviscid and viscous fluxes along side IJ_S and $\mathbf{B}_i$ is the boundary integral.

The inviscid fluxes $\mathbf{F}_{IJ_S}$ in Equation 3.10 are treated using a central difference formulation with a suitable artificial dissipation. While the viscous fluxes $\mathbf{G}_{IJ_S}$ are expressed using the edge weights η_{IJ_S} and calculating the gradients of the primitive variables at the mesh nodes. Further details are reported by Sayma et al. [2000a].

The system of equations is advanced in time using first order, implicit time integration. Steady flow calculations are achieved by using a point relaxation procedure with Jacobi iterations. While unsteady, time-accurate flow computations are treated by a dual time stepping procedure (Arnone et al. [1995]). In addition to the internal Jacobi iterations with a pseudo-time step, time accuracy is ensured with external Newton iterations (Chakravarthy [1984]). This is achieved by rewriting Equation 3.10 as

$$\frac{d}{dt}(\Omega_I \mathbf{U}_I) = \mathbf{R}(\mathbf{U}_I) \tag{3.11}$$

For both first order and second order scheme, Equation 3.11 can be rewritten as

$$\frac{(1+\chi)((\Omega_I \mathbf{U}_I)^{n+1} - (\Omega_I \mathbf{U}_I)^n) - \chi((\Omega_I \mathbf{U}_I)^n - (\Omega_I \mathbf{U}_I)^{n-1})}{\Delta t} = \mathbf{R}^{n+1} \tag{3.12}$$

where n represents the time level. When $\chi = 0$, it is the first order scheme and when $\chi = \frac{1}{2}$, it is the second order scheme. The implicit nonlinear system of equations represented in Equation 3.12 has to be solved at each time step. Therefore, an iterative equation can be achieved by adding a pseudo-time derivative term $\mathbf{U}_\tau$ to the left-hand side of Equation 3.12. By linearising the residual term, the pseudo-time integration which advances the solution from t_n to t_{n+1} becomes

$$(\frac{1}{\Delta\tau} + \frac{1+\chi}{\Delta t} - \mathbf{J}^m)\Delta(\Omega_I \mathbf{U}_I) = \mathbf{R}^m - \frac{1+\chi}{\Delta t}{\Omega_I}^{n+1}{\mathbf{U}_I}^m - {\mathbf{E}_I}^n \tag{3.13}$$

where $\Delta\tau$ is the pseudo-time step. $\mathbf{J}^m$ is the Jacobian appearing in the linearisation of $\mathbf{R}^{m+1}$. While $\Delta(\Omega_I \mathbf{U}_I) = {\Omega_I}^{n+1}({\mathbf{U}_I}^{m+1} - {\mathbf{U}_I}^m)$ where ${\mathbf{U}_I}^m$ is the mth approximation of ${\mathbf{U}_I}^{n+1}$ and ${\mathbf{E}_I}^n$ involves the physical time derivative at previous time steps and is constant during the iteration process, represented by

$${\mathbf{E}_I}^n = \frac{(1+\chi)(\Omega_I \mathbf{U}_I)^n - \chi((\Omega_I \mathbf{U}_I)^n - (\Omega_I \mathbf{U}_I)^{n-1})}{\Delta t} \tag{3.14}$$

Equation 3.13 is solved iteratively until the term $\Delta(\Omega_I \mathbf{U}_I)$ is sufficiently small. Within this iteration level, the linearised system of equations expressed in Equation 3.12 is solved by the Jacobi iteration procedure. It can be performed using traditional acceleration techniques such as local time stepping and residual smoothing.

The time accuracy is guaranteed by the outer iteration level with a fixed time step throughout the solution domain.

3.3 Description of the rotor

A transonic axial compressor rotor, NASA Rotor 37, was chosen for the code validation and to study effects of blade damage on axial compressor performance because of the availability of the geometry and experimental data in the public domain. It also has been validated by many researchers using CFD such as the work done by Khalil and Hongwei [2009] and Ameri [2010]. It was one of a series of rotors designed as the inlet rotor for an eight stage core compressor of an aircraft engine at NASA Lewis Research Centre in the late 1970's (Moore and Reid [1980]). A single rotor blade is shown in Figure 3.2. The rotor has 36 multiple-circular-arc (MCA) blades, a tip speed of 454.14 m/s and a design pressure ratio of 2.106 at the mass flow rate of 20.19 kg/s. It has an aspect ratio of 1.19. The rotor inlet relative Mach number varies from 1.493 at the tip to 1.125 at the hub. The diffusion factor of the rotor is approximately 0.56 at both the hub and tip with a maximum value of 0.58 at 85% span. The main characteristics of Rotor 37 are listed in Table 3.1 (Reid and Moore [1978]).

3.4 Boundary conditions

In this section, boundary conditions used will be defined. Before that, the computational geometry and flow domain for steady state simulations will be presented. The typical mesh used for the rotor is shown in Figure 3.3. The computational domain of one single passage for the steady state simulations is shown in Figure 3.4. The inlet boundary was placed at approximately 76% chord length upstream from the hub. As the compressor approaches stall boundary, it is very sensitive to downstream pressure variations. Therefore, the rotor was connected to an outlet guide vane (OGV) downstream which was designed to remove the flow swirl and a variable

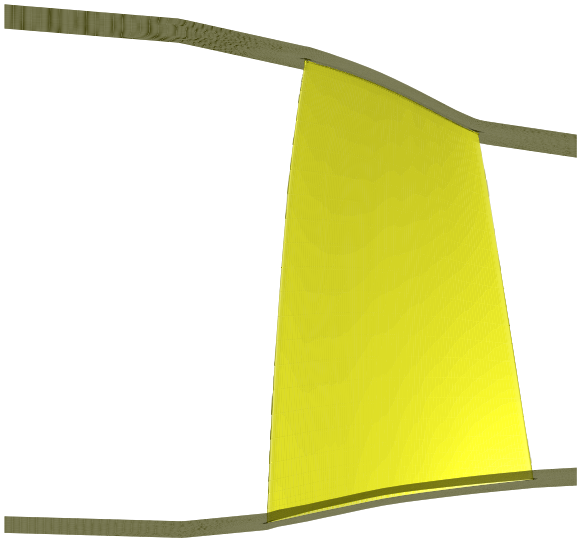

Figure 3.2: View of one Rotor 37 blade

Table 3.1: Specifications of Rotor 37

Rotor inlet hub to tip diameter ratio	0.7
Rotor blade aspect ratio	1.19
Rotor tip relative inlet Mach number	1.48
Rotor hub relative inlet Mach number	1.13
Rotor tip solidity	1.29
Blade airfoil sections	MCA
Number of blades	36
Design wheel speed(rad/s)	1,800
Tip speed (m/s)	454
Rotor total pressure ratio	2.106
Rotor efficiency (adiabatic)	0.877
Measured choking mass flow rate (kg/s)	20.93
Reference temperature (K)	288.15
Reference pressure (kN/m^2)	101.33

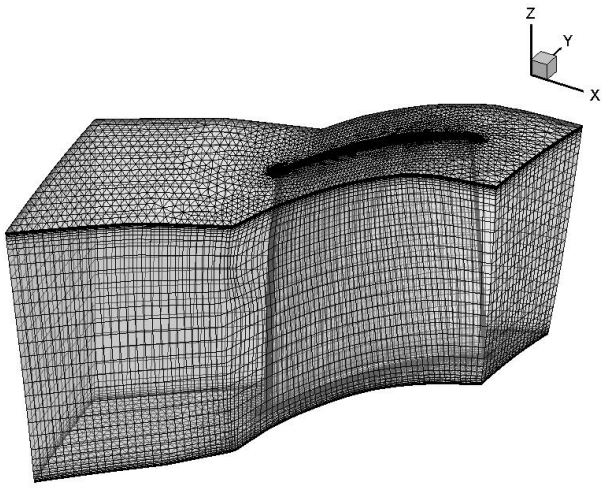

Figure 3.3: Typical mesh for Rotor 37

Figure 3.4: Geometry demonstration for single passage steady state analysis

nozzle which represented an experimental throttle. Mixing planes were used at the interfaces between bladerows. Generally speaking, boundary conditions applied in the simulation should be the same as the ones obtained in the experiment. However, the exact boundary conditions were not known for this case. Therefore, using the geometry as shown in Figure 3.4, uniform axial flow with ambient air conditions were applied at the inlet and outlet. Total pressure and temperature with zero flow angles were used at the inlet and static pressure was used at the outlet.

3.5 Grid independence study

It is well known that the axisymmetry of flow will be broken during rotating stall. Therefore, the simulations would require a model with full annulus. Typically, it

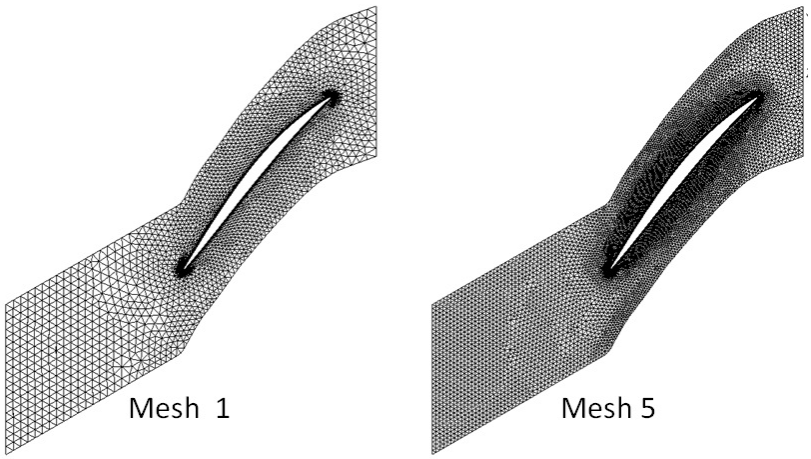

Figure 3.5: Mesh comparison in the blade to blade direction

is performed for at least several engine rotations requiring extensive computational resources. Hence it is important to strike a balance between the grid refinement and the required accuracy of the solutions so that fundamental flow features pertinent to rotating stall are not affected by the grid quality and the investigation could be completed within the required time scale. An extensive investigation was carried out during this study to choose a suitable grid quality for both the code validation and unsteady computations.

Although the primary purpose of this study is to perform unsteady computations, it was more practical to conduct a grid independence study using steady state single passage analyses. All the simulations were performed at the design speed for an operating point close to peak efficiency. Five different grids with gradual refinement in both blade section and span-wise directions were used. The mesh comparison in the blade section for mesh 1 and mesh 5 was shown in Figure 3.5. The number of grid points and a summary of the results of global flow parameters are shown in Table 3.2, where PR indicates the total-to-total pressure ratio and TR represents the total-to-total temperature ratio. It can be concluded from the table that the overall performance for mass flow rate, total pressure ratio, total temperature ratio and efficiency are very similar for all five grids.

Blade to blade Mach number contour comparisons at three different spans are shown in Figures 3.6, 3.7 and 3.8. These figures provide qualitative information

Table 3.2: Overall performance comparisons for different grids

Cases	Mesh points	mass flow (kg/s)	PR	TR	Efficiency
Mesh 1	165,504	20.6	2.097	1.27	0.87
Mesh 2	266,421	20.5	2.095	1.27	0.87
Mesh 3	390,585	20.4	2.095	1.27	0.87
Mesh 4	608,354	20.4	2.095	1.27	0.87
Mesh 5	1,224,335	20.4	2.096	1.27	0.87

regarding the flow which shows that the flow features are the same for all five grids. As seen in Figure 3.6 and 3.7, there is a single bow shock observed. The bow shock is just attached to the leading edge of the blade. At mid-span, a passage shock is observed instead with an expansion at the leading edge. At 95% and 90% span, the shock wave is closer to the trailing edge and it is closer to the leading edge at 50% span. The flow is decelerated near the suction surface until the shock wave and is diffused towards the trailing edge. However at 95% span, there is a low momentum flow region which forms a 'slip line' near the pressure side of the blade. The 'slip line' is caused by the interaction between the flow deceleration after the shock wave and the tip leakage flow. The low momentum flow is pushed towards the pressure side of neighbouring blade by the tip leakage flow. This feature is important for rotating stall investigations as mentioned in the literature review. It can be seen that the code is capable to capture this feature well even with the very coarse grid. At each span, the shock patterns are very similar and the boundary layer thickness is slightly reduced when the grid is refined which is consistent with the results reported by Denton [1996]. Figure 3.9 shows pressure contour plots on the suction side of the blade. It can be seen that the shock is across the whole blade. It can also be seen that the shock is closer to the trailing edge at the tip and moves towards the leading ledge at the hub. To sum up, results for the Mach number contours and pressure distribution contours are very similar for different grids including the shock pattern, position, before and post shock flow behaviour. The detailed positions for shock will be verified using quantitative results.

Mach number contours for mesh 1 and mesh 5 was also compared at near stall

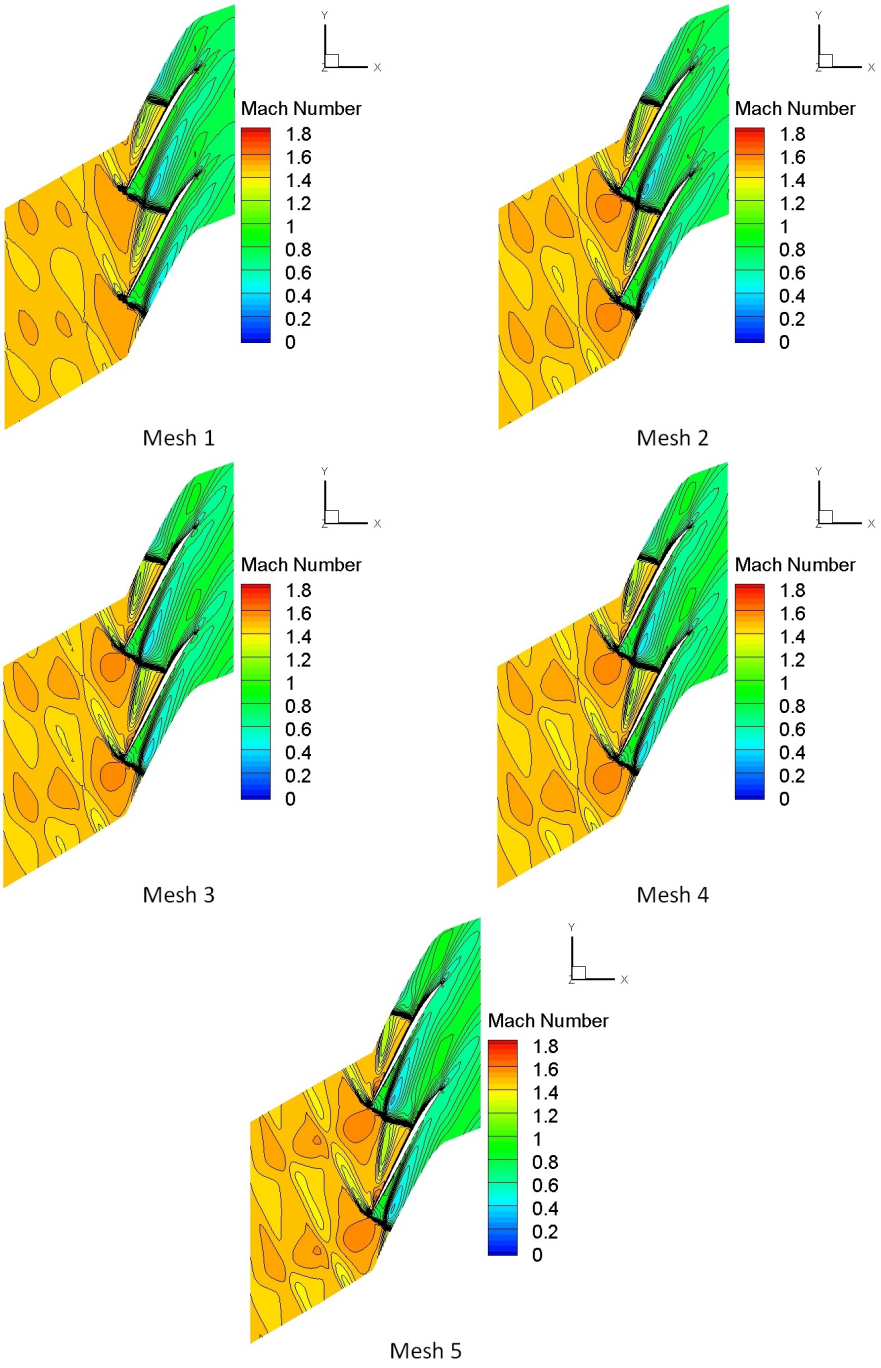

Figure 3.6: Mach Number Contour Comparison at 95% span

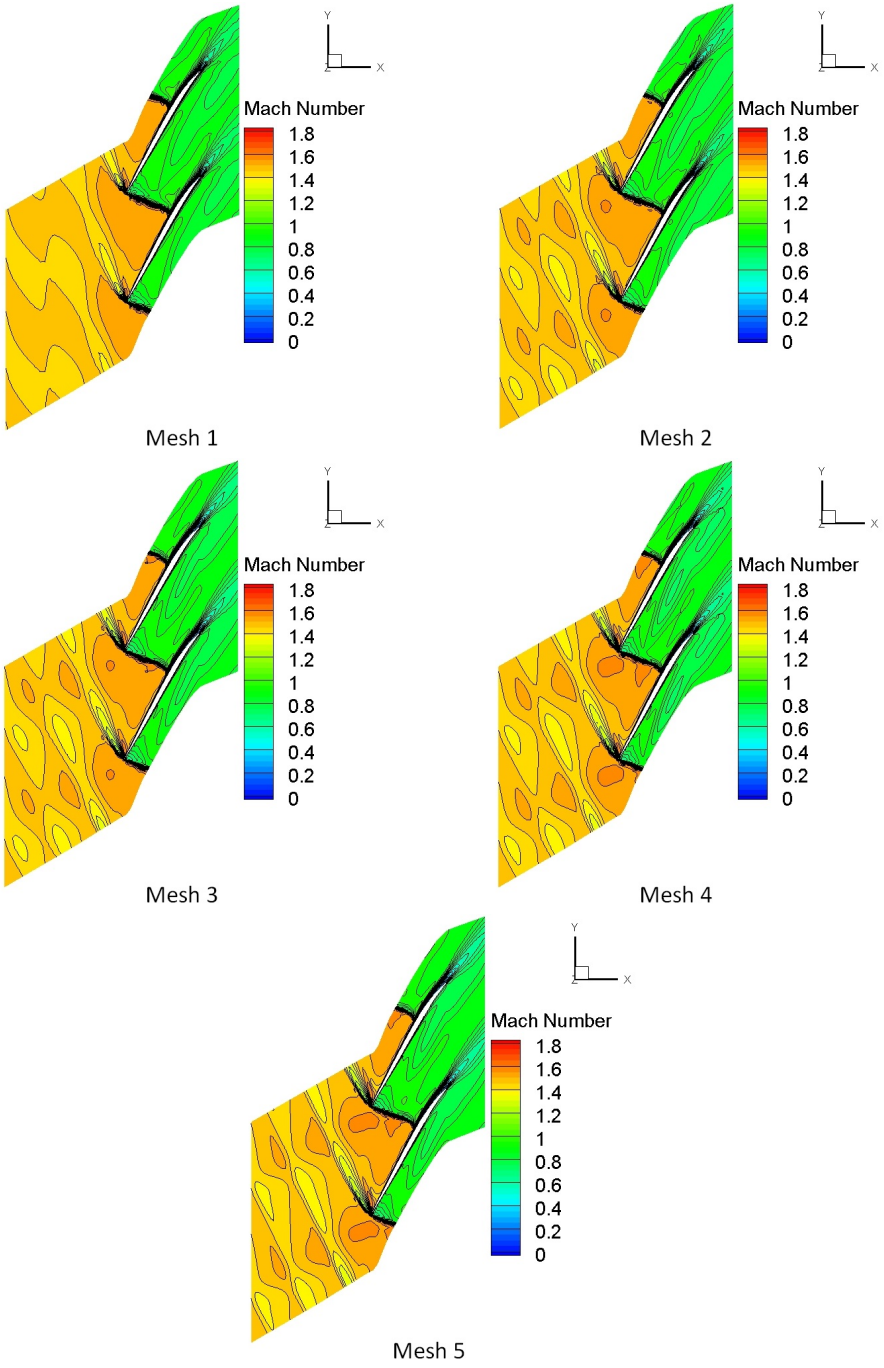

Figure 3.7: Mach Number Contour Comparison at 90% span

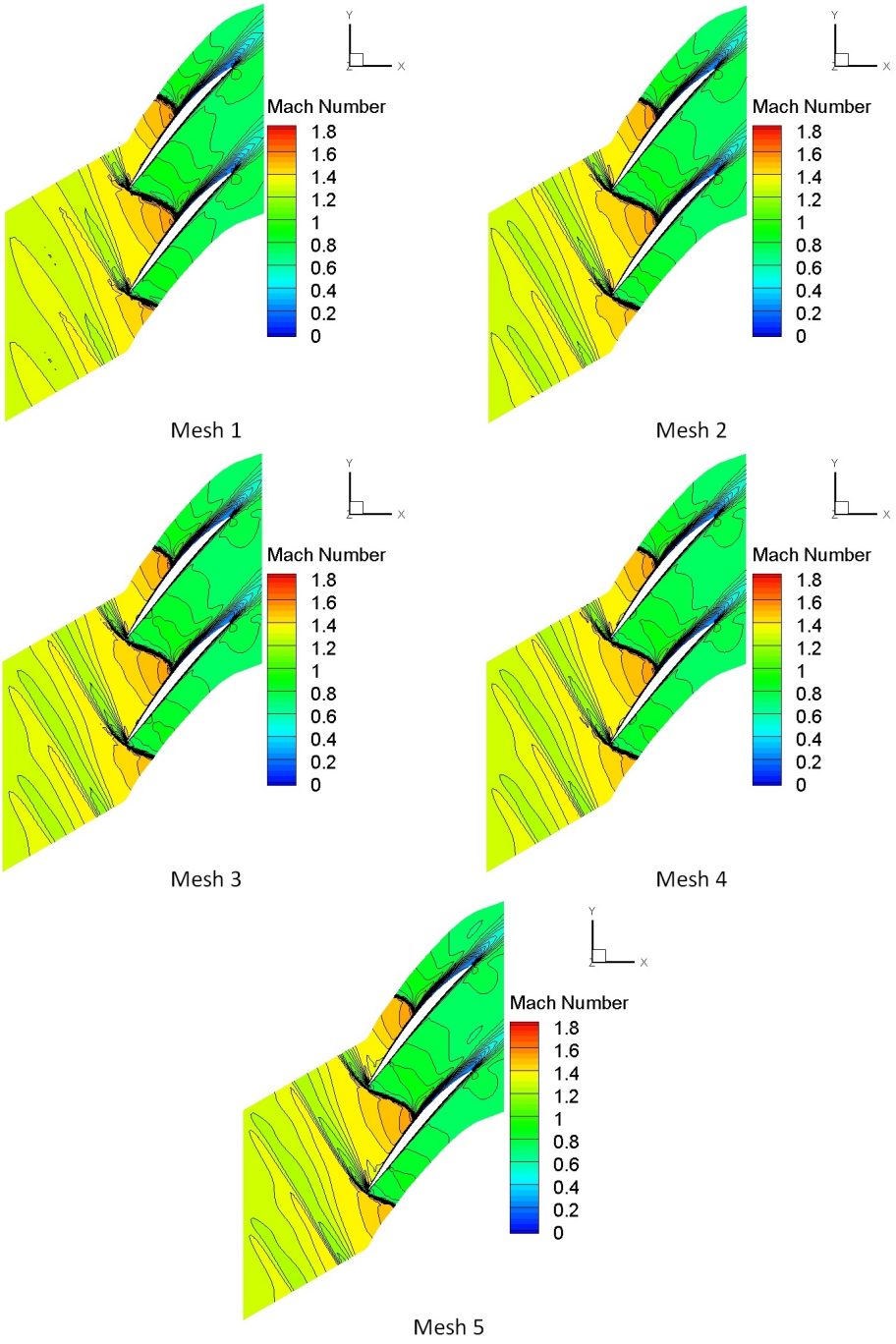

Figure 3.8: Mach Number Contour Comparison at 50% span

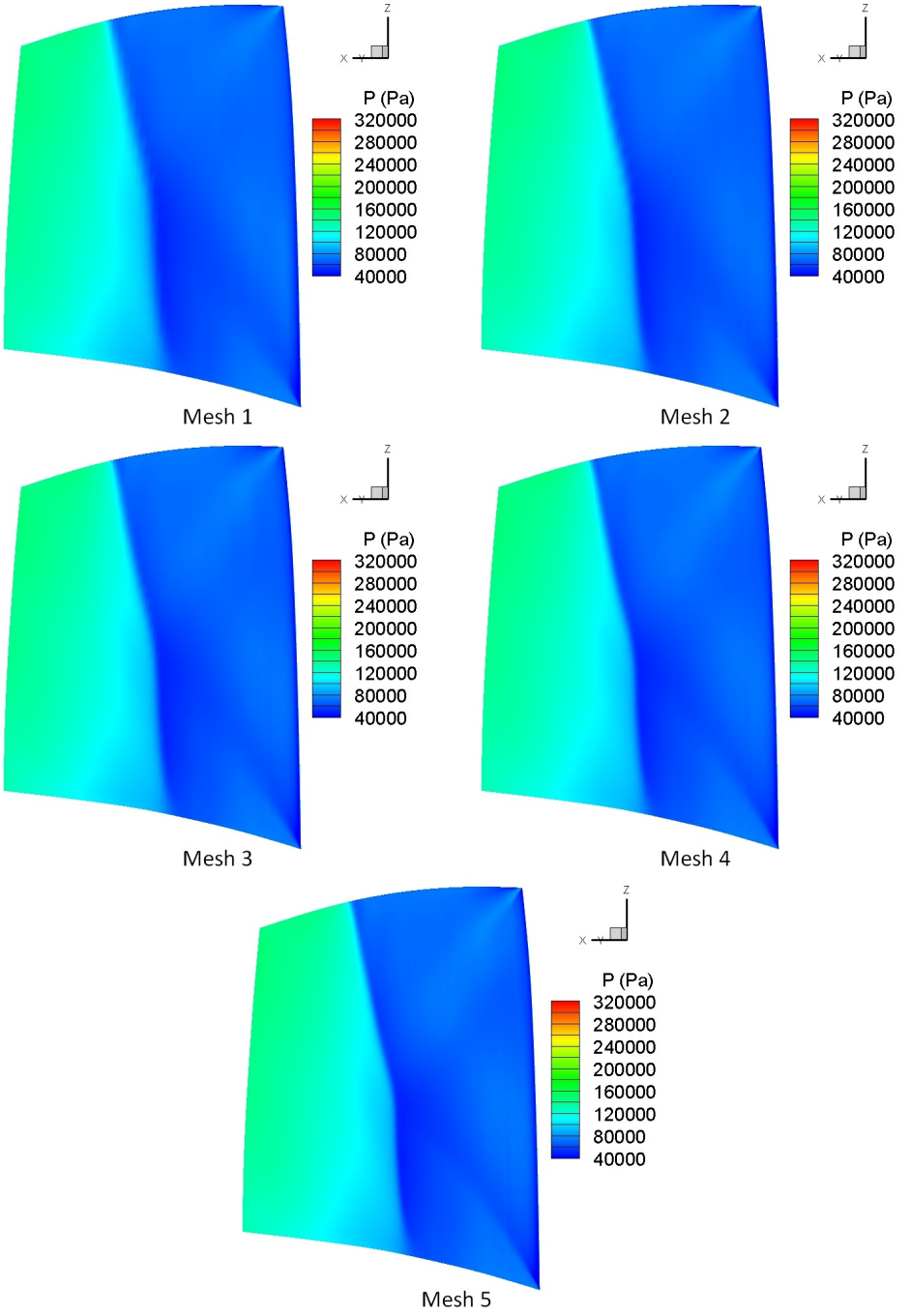

Figure 3.9: Pressure Contour Comparison on the suction side of the blade

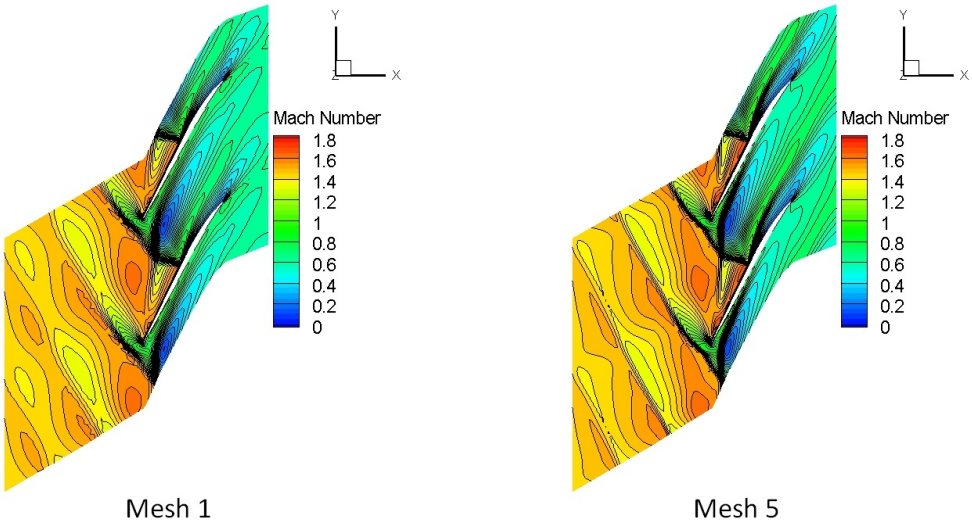

Figure 3.10: Mach Number Contour Comparison at 95% span at near stall condition

condition at design speed which is shown in Figure 3.10. The flow pattern was similar for both mesh 1 and mesh 5. Flow was decelerated before shock and a separation bubble was captured after the shock which is indicated by the low Mach number region. The boundary layer near the trailing edge was resolved better with finer grid. Nevertheless, it can be concluded that the key features of the flow can be predicted with the coarsest mesh, mesh 1.

Pressure profile comparisons at different spans are shown in Figures 3.11, 3.12 and 3.13 while the span-wise variations of the circumferentially averaged pressure ratio and temperature ratio at outlet of the rotor are shown in Figure 3.14. The results show that there is very little difference in these flow features amongst the grids used, with the differences mainly around the shock area and close to hub and tip in the radial profiles. Close examination of the differences show that they decrease as the grid is refined. Although it is difficult to infer from this to the quality of the best grid required for the unsteady computations, it was decided that mesh 3 presents a good accuracy, and thus it was used for the code validation. Solution on mesh 1 differed most in several aspects compared to other grids. However the maximum difference is less than 1%. As discussed before, the key features of the flow at near stall can be captured with mesh 1 which is similar as the finest mesh. Therefore,

as a compromise between accuracy and computational costs, it was decided to use mesh 1 for the unsteady simulations.

3.6 Validation with experimental data and discussion

In this section, solutions at different working conditions are compared with the experimental data as reported by Suder [1997]. In the experiment, the rotor was tested at three different shaft speeds with relevant tip gap clearance for each speed. Thus, in both steady state and unsteady simulations, the rotor was simulated with the same tip clearance as reported in the experiment.

Comparisons at three different rotational speeds are shown in Figure 3.15. From the pressure ratio characteristics, it can be seen that CFD solutions have a good agreement with the experimental data. It can also be seen from the figure that near stall points are also well predicted for all three speeds. However, efficiencies at all three speeds are under predicted yet with a good prediction in the general shape of the profile. This could be explained firstly by referring to Denton [1996]. Measurements do not accurately capture the high loss regions in the annulus boundary layer due to limitations of the instrumentation, which also explains why the pressure ratio matching is much less affected. Secondly annulus line geometry behind the rotor was not available to a sufficient distance, and there could have been differences between the computational and actual geometry in that region affecting flow diffusion and hence end wall losses. Thirdly, nominal uniform tip clearance values are used for the three speeds, which are likely to have differences from those prevailing during the experiment. Denton [1996] also reported that the tip clearance value given from the experiment can be inaccurate since the actual tip edge of the rotor was rounded by erosion. Furthermore, for this test case, as reported by Moore and Reid [1980], the flow was axial at the inlet of the test rig and was turned perpendicularly twice to reach the inlet of the rotor. That would cause a flow distortion at the inlet during

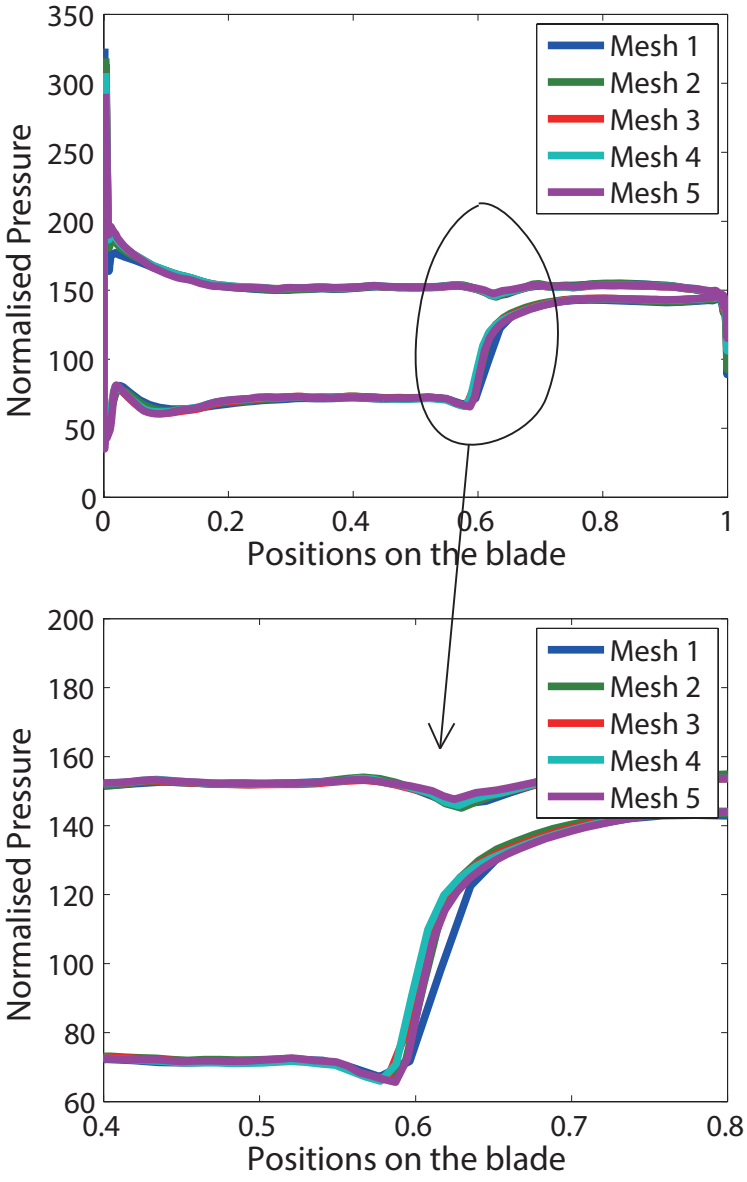

Figure 3.11: Pressure profile comparison at 95% span

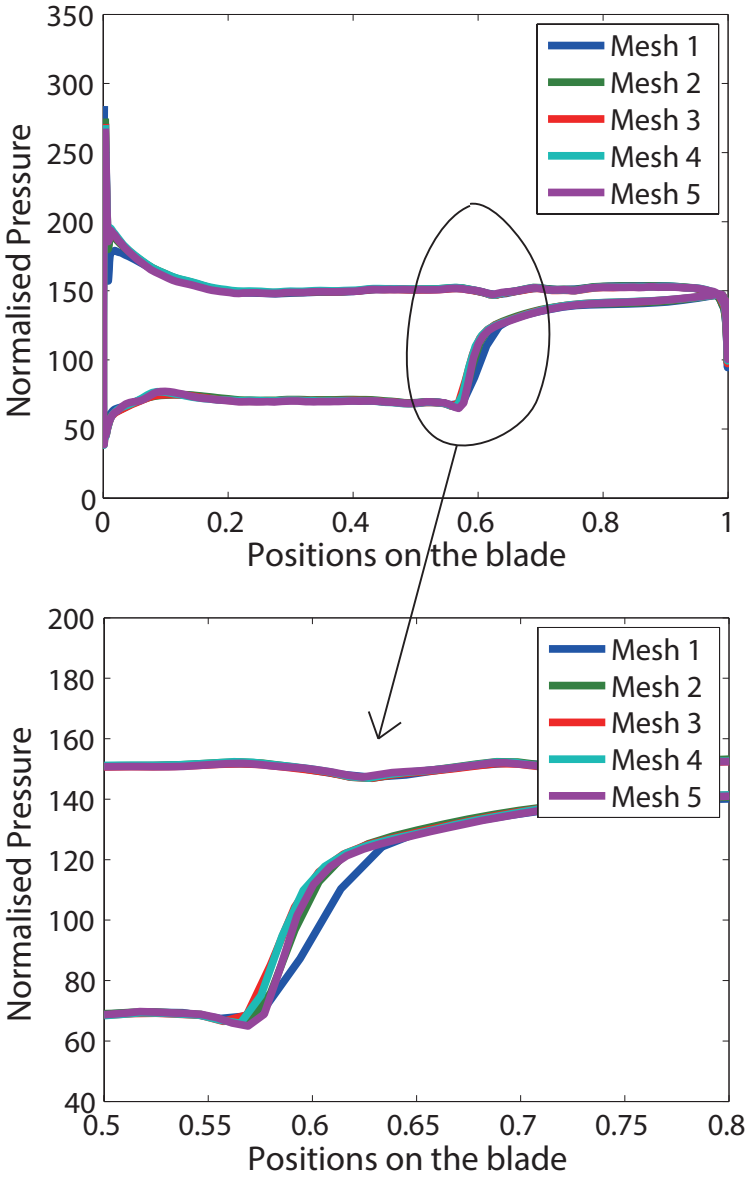

Figure 3.12: Pressure profile comparison at 90% span

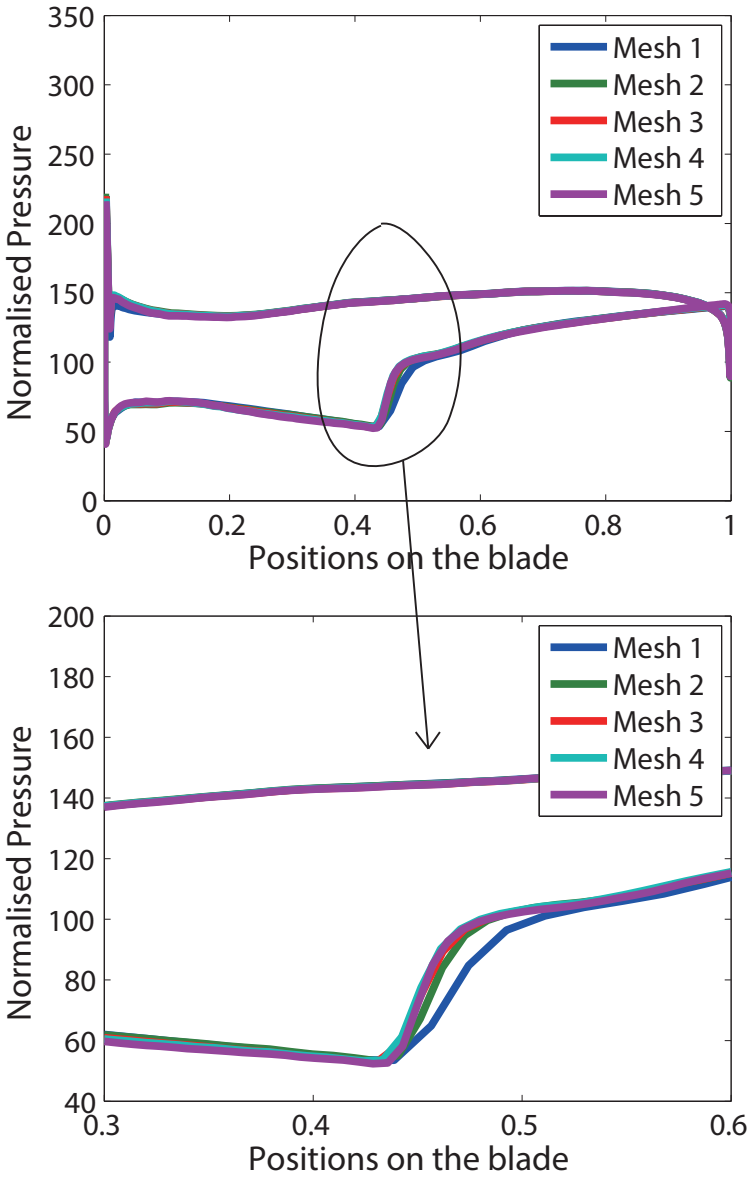

Figure 3.13: Pressure profile comparison at 50% span

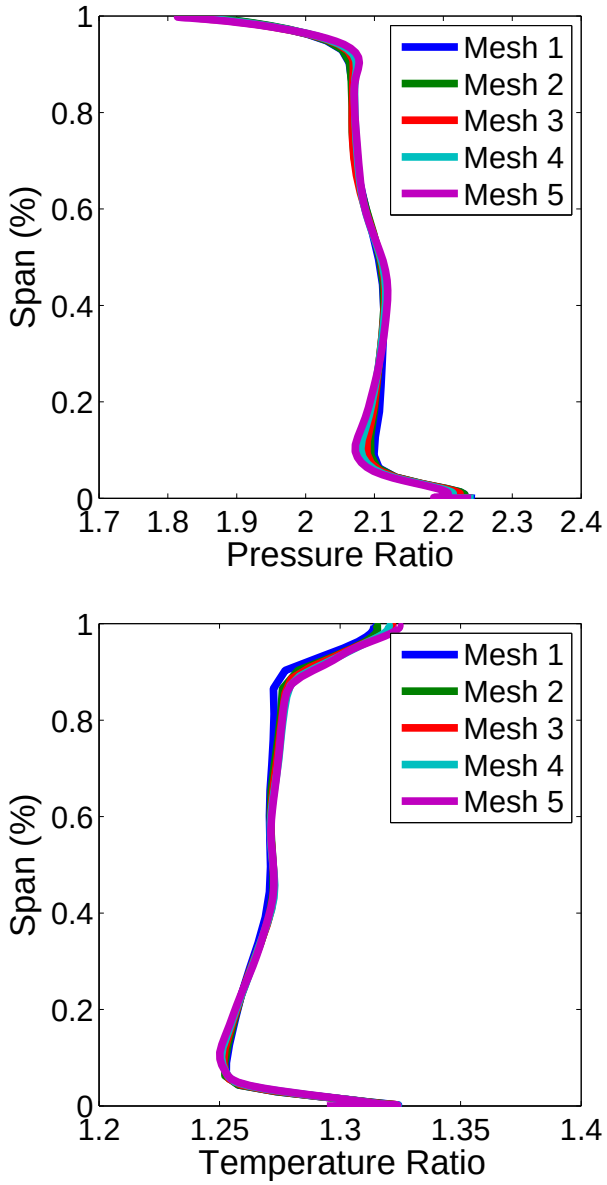

Figure 3.14: Radial distribution of circumferentially averaged pressure and temperature ratios at downstream of the rotor

the experiment while uniform flow was assumed in the simulations. In addition, CFD predictions may contain certain degrees of inaccuracy such as the use of wall functions and one-equation turbulence model. A combination of these factors may have contributed to the differences in the efficiencies.

Mach number contour plots are compared with experimental data (Suder [1997]) at 95% span at both high flow and low flow condition at design speed marked in the compressor map. A comparison at the high flow condition is shown in Figure 3.16. The solution from CFD simulation is similar to the experiment. A single bow shock was observed from both experimental and CFD data. The post shock Mach number from the CFD solution is slightly lower than the one in the experiment however the flow pattern is well predicted. A region with lower Mach number which forms 'slip line' is observed for both experiment and numerical predictions. This feature was also found in the LES investigation of this rotor reported by Hah [2009]. A comparison of Mach number contour plots at the low flow condition is shown in Figure 3.17. As shown in the figure, there was also a single shock. A clear region with lower Mach number was observed in the passage after the shock wave. That is caused by the interaction of larger positive flow angle, flow deceleration after shock and tip leakage flow. By comparing Figure 3.16 and 3.17, it can be seen that the shock wave moves towards the outside of the passage at low flow condition which increases shock loss. The boundary layer is thickened after shock on the suction side with less flow due to the larger positive incidence. That would increase the profile loss. The combination of those two leads to lower efficiency towards to stall boundary. Figure 3.18 shows the comparison of Mach number contour along the 70% span at low flow condition for design speed. A single shock was observed which is in similar pattern and position on the blade. As in the zoomed figure, flow was similar as the experiment including shock pattern and boundary layer thickness. A boundary layer was built up after the shock wave and towards the trailing edge. The post shock Mach number from CFD solution was slightly smaller than the one in the experiment but with the same general flow pattern.

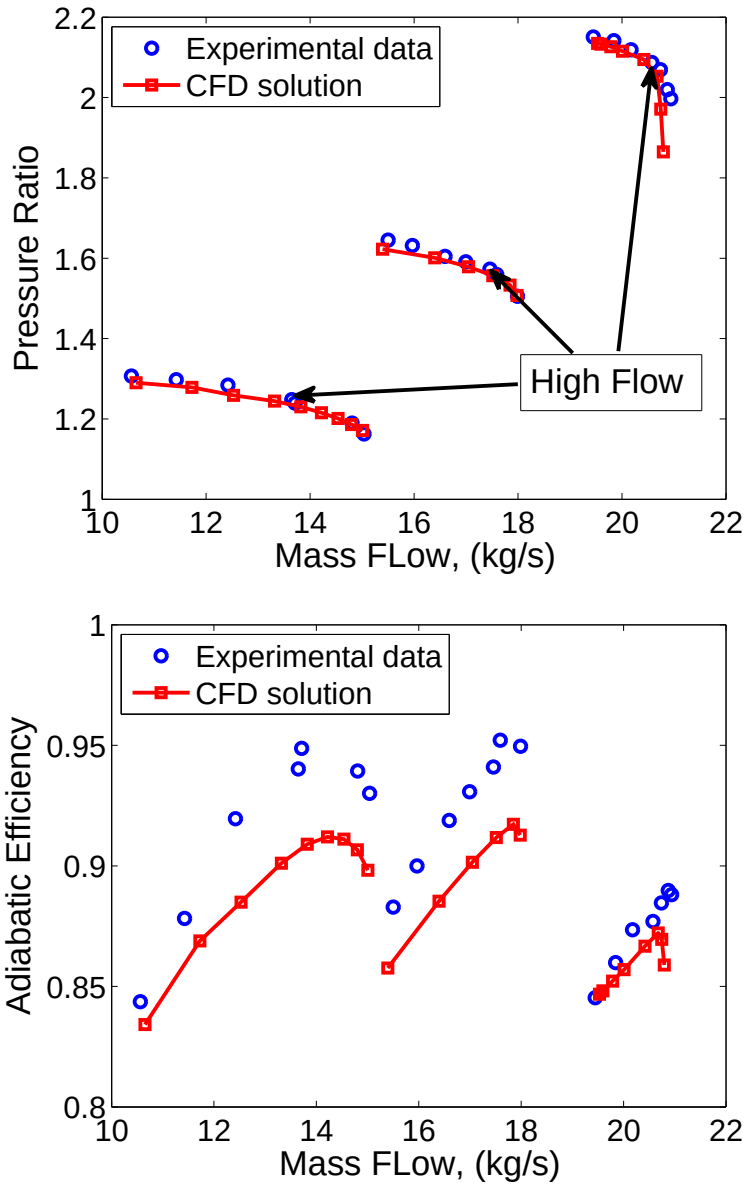

Figure 3.15: Comparisons of Overall Characteristics with Experimental Data (Left to right: 60% speed, 80% speed and 100% speed)

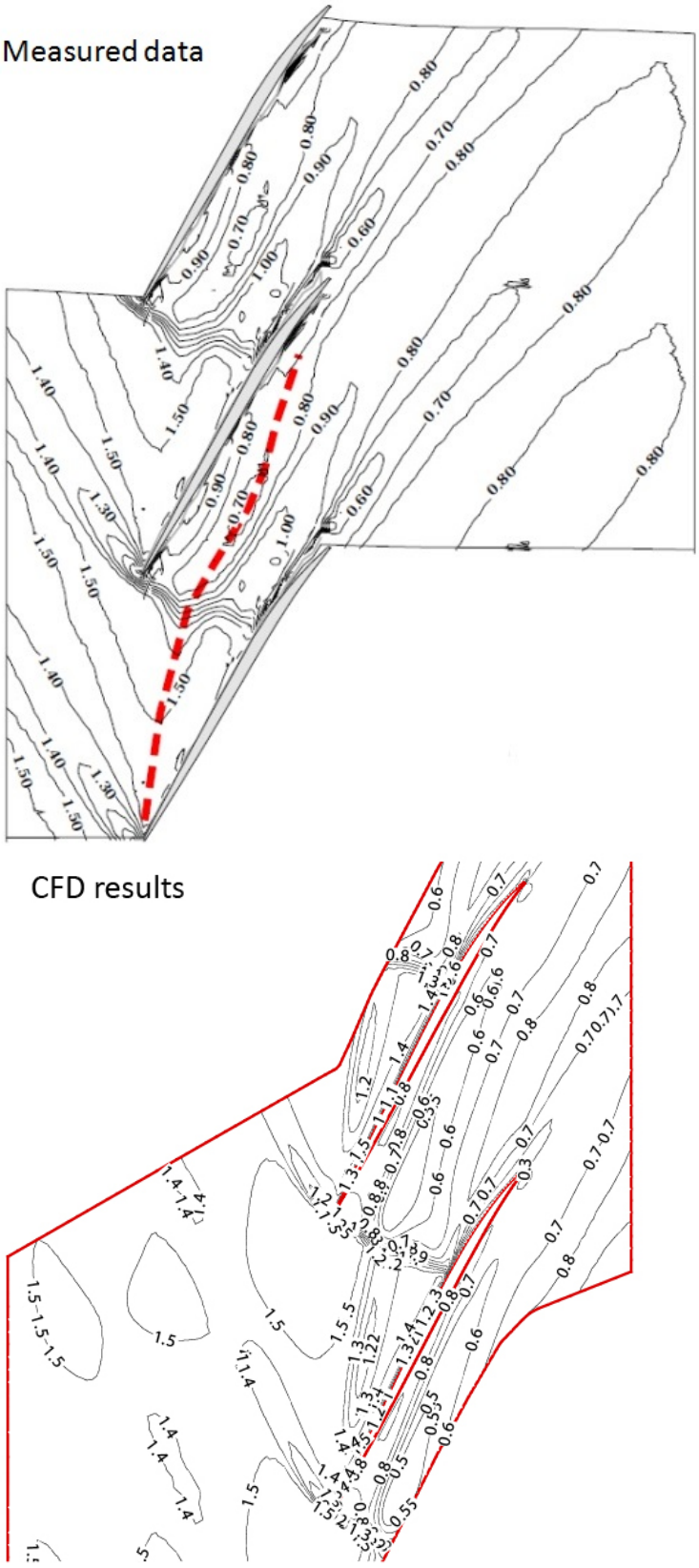

Figure 3.16: Contours of Mach number in a blade-to-blade view along the 95% span at high flow condition for design speed(Measured data is from Suder [1997])

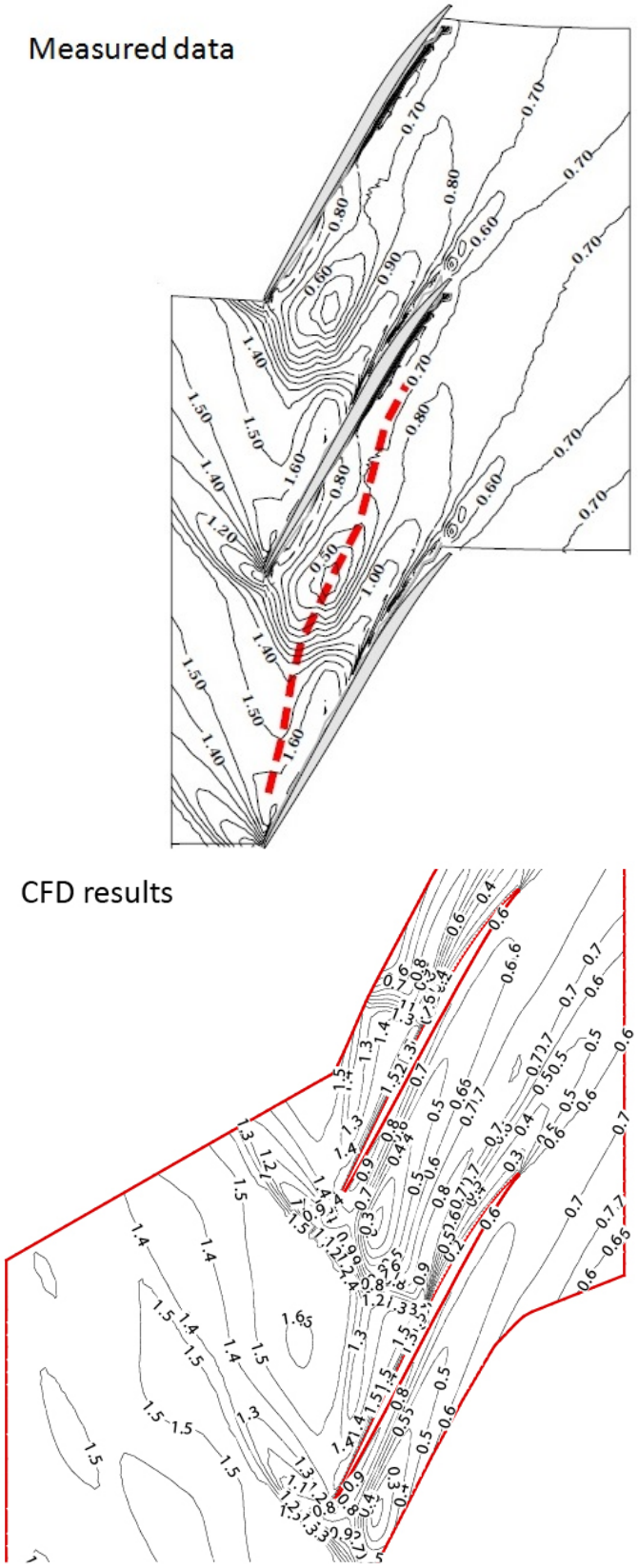

Figure 3.17: Contours of Mach number in a blade-to-blade view along the 95% span at low flow condition for design speed(Measured data is from Suder [1997])

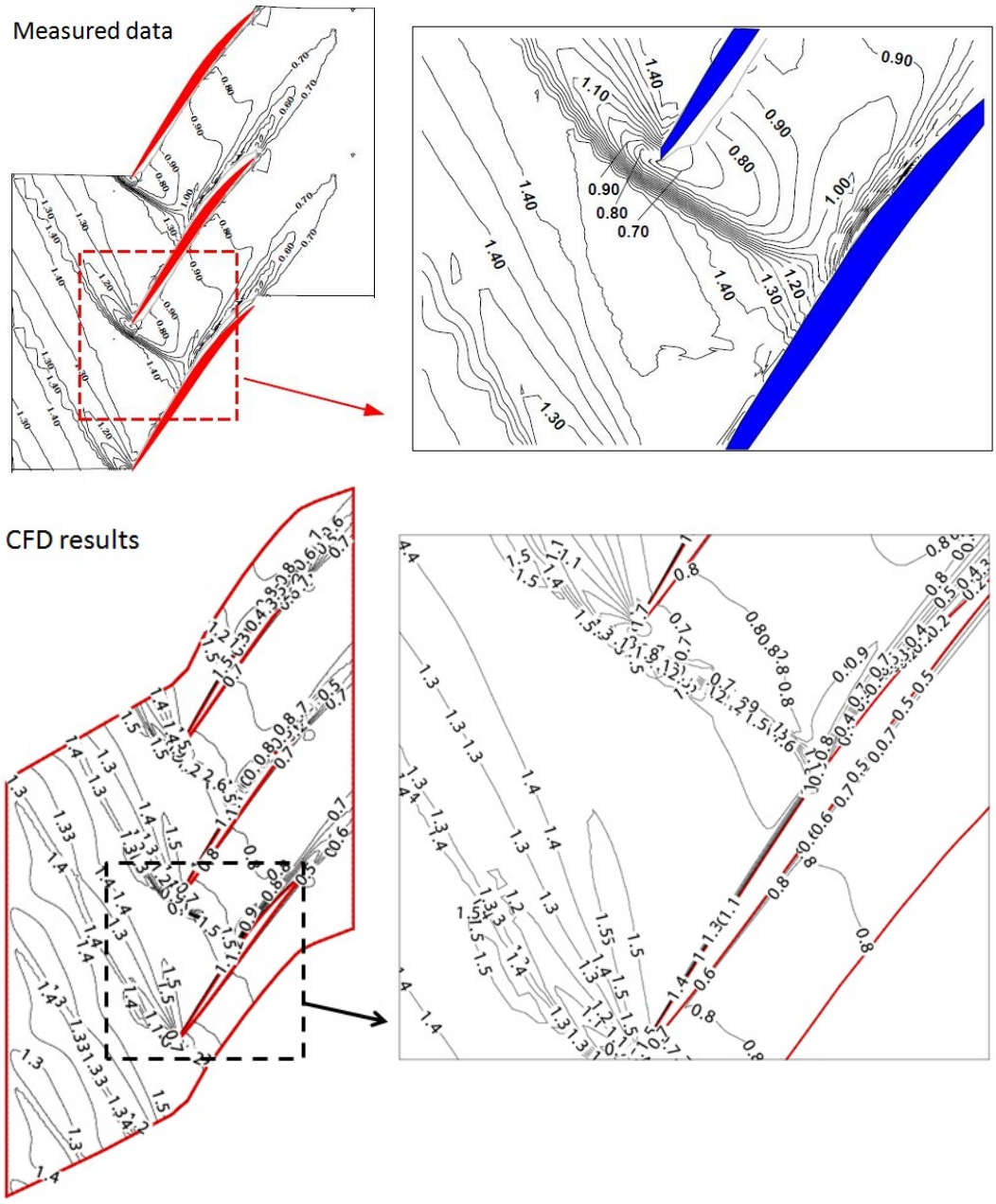

Figure 3.18: Contours of Mach number in a blade-to-blade view along the 70% span at low flow condition for design speed(Measured data is from Suder [1997])

The circumferentially averaged total pressure ratio and temperature ratio distributions in the span-wise direction downstream the rotor for all three speeds are shown in Figure 3.19. Those distributions are obtained at high flow operating conditions which are marked in the pressure ratio map in Figure 3.15. The CFD results agree fairly well with the measured data. The general shapes of the profiles are in a very good agreement. It can also be seen that the code is capable of predicting a typical pressure deficit at the tip and hub. This general and detailed agreement with the experimental data gave confidence in the ability of the code to perform accurate predictions for the present study. There is no unsteady experimental data available, so further validations using this case are not possible.

3.7 Summary

In this chapter, a transonic compressor rotor was chosen to validate the in-house CFD code used in this research. The flow model used was firstly described. To find a compromise between accuracy and computational costs, grid independence study was then performed. Decisions were made for appropriate meshes for both steady state validation and unsteady rotating stall investigations. From the validation study, the overall performance has good agreement with experimental data including the general profile of pressure ratio and efficiency. However, the efficiency was under predicted for all three speeds which was explained in the discussion. The near stall points at all three speeds were also well predicted. Detailed examination of blade to blade Mach number contours showed that the flow was well predicted from CFD including the general flow pattern, shock pattern, its position and pre and post shock flow behaviour. Good agreement was also obtained for the span-wise variations of pressure ratio and temperature ratio. It can be concluded that the CFD code provided good agreement with the experimental data. That provides confidence in the ability of the code to perform accurate predictions for unsteady rotating stall calculations for the present study.

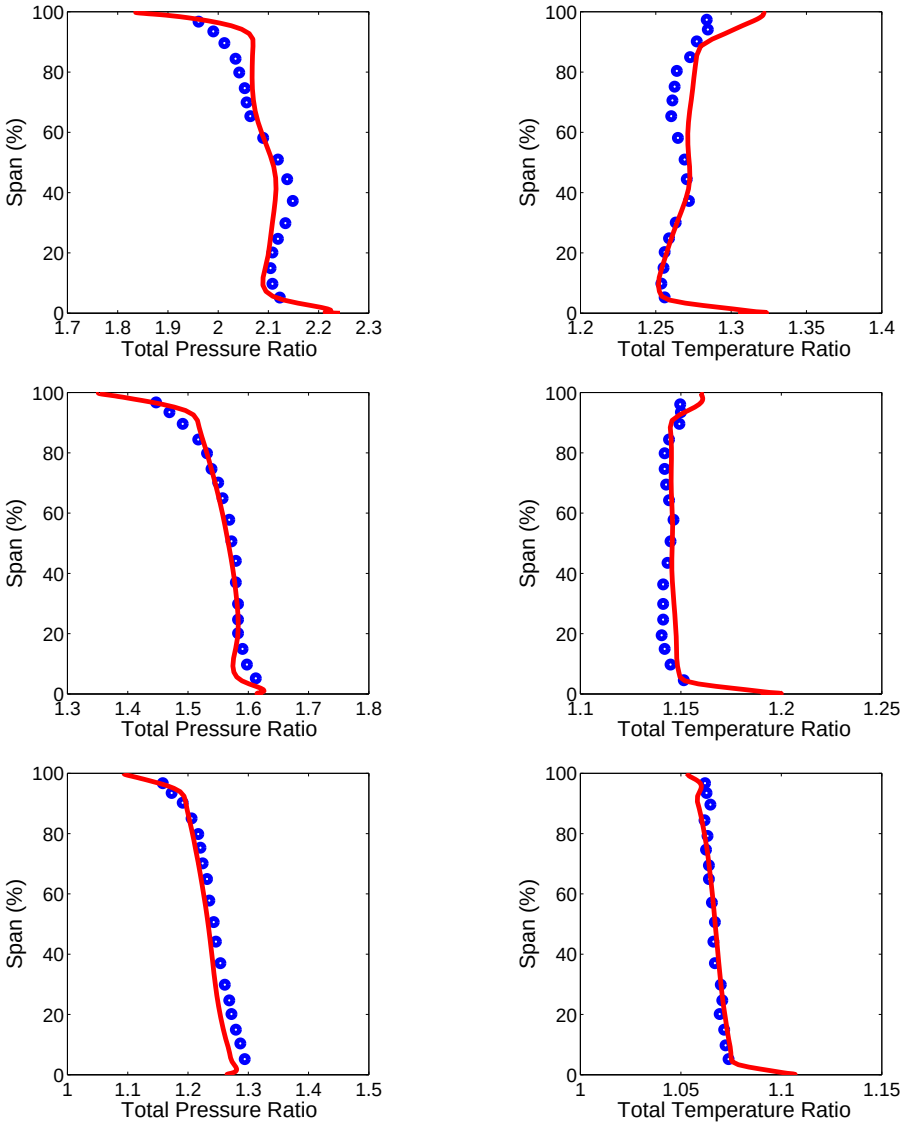

Figure 3.19: Comparisons of Radial Flow Characteristics

Chapter 4

Rotating stall of a single stage axial flow compressor with nominal blade settings

4.1 About this chapter

In this chapter, a time-accurate unsteady CFD simulation performed near the stall boundary is presented. The simulation was performed on a transonic axial compressor, NASA Rotor 37, which was used for model validation in Chapter 3. This chapter is a part of the blade damage study. To investigate the blade damage effects, it is beneficial to get an understanding of rotating stall characteristics without any damaged blade. Before investigating the flow behaviour near stall, another case was also performed to investigate the flow characteristics under an operating condition which was away from the surge line to verify the unsteady simulations using compressor full annulus model. It was then compared with steady state analysis solution at the same operating condition on the compressor map.

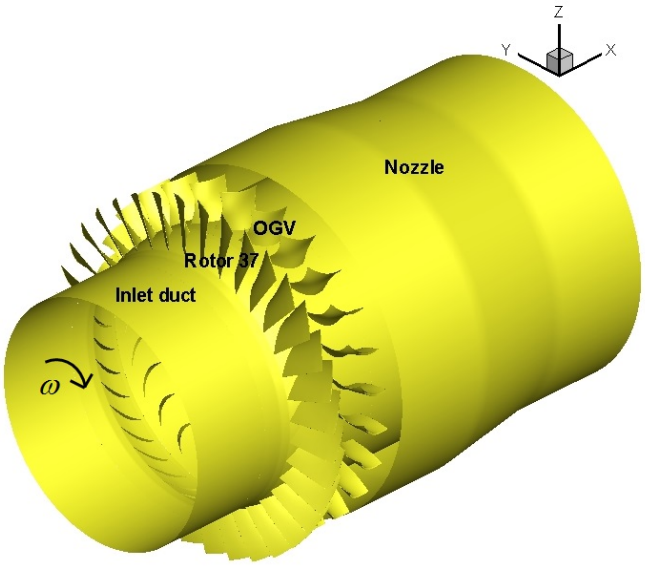

Figure 4.1: Computational geometry for unsteady simulation

4.2 Computational domain and boundary conditions

In this section, the computational domain and boundary conditions used will be presented. It is normally assumed that flow is axisymmetric when the compressor is operating under most of the conditions on the performance map. When the operating condition approaches the stall boundary, compressors could encounter rotating stall before stalling completely or going into surge. Therefore during rotating stall, the axisymmetry of the flow is broken due to the existence of stall cells. Although it is possible to model rotating stall using a sector of the compressor assembly which may require some priori knowledge such as the number of stall cells according to the purpose of the investigation. Consequently, because this is generally an unknown parameter, a full annulus model as shown in Figure 4.1 is desirable. All the unsteady simulations in this study were performed at 60% of rotor speed. The main reason is that rotating stall is commonly found at part speed reported in literatures as discussed in Chapter 2.

All unsteady simulations presented in this chapter start from converged steady

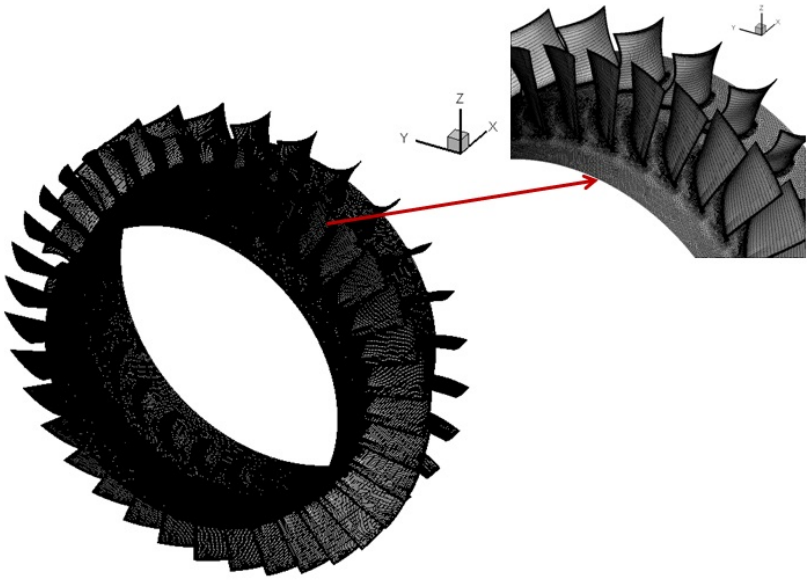

Figure 4.2: Partial view of the mesh used for full annulus simulations

state solutions. A view of the unsteady computational geometry is shown in Figure 4.1. It consists of an inlet duct, Rotor 37, Outlet Guide Vanes (OGVs) and a variable nozzle. The rotor is rotating with a rotational speed of ω in the clockwise direction along the x axis as indicated in the figure. Sliding planes are used at the interfaces of the blade rows. They are boundaries typically used for unsteady flow simulations. Those two planes between the rotor and stator blades moves relative to each other. The solutions on those planes are determined by obtaining stator and rotor fluxes for rotor and stators respectively, using specific interpolations. The corresponding flow data exchanged between two planes via specifically functions at the end of each time step. More details regarding mechanisms regarding to sliding planes could be referred to Vahdati et al. [2008]. The computational domain used contains approximately 10 million points which is partially shown in Figure 4.2.

A major problem in rotating stall simulations is that it is difficult to specify the downstream boundary conditions when there are fluctuations in mass flow and pressure rise. In this investigation, a methodology reported by Vahdati et al. [2005] was applied using a variable nozzle at the back representing an experimental throttle to control downstream flow boundary conditions. More details regarding this

strategy rather than applying fixed static pressure downstream is reported by Wu et al. [2003]. The inlet boundary is located at approximately three chord lengths upstream of the rotor blade. Therefore, both inlet and outlet boundaries were extended upstream and downstream respectively. The reason for that is to avoid numerical reflections from boundaries which is also discussed by Wu et al. [2003]. The one dimensional non-reflection boundary conditions are applied in the numerical scheme to prevent any spurious reflections of the outgoing waves. At inlet, air with ambient condition is assumed and total pressure and temperature are applied with zero flow angles. Different performance conditions on the compressor characteristic map can be achieved by adjusting the size of the downstream nozzle.

Another difficulty is how to initiate rotating stall with the least computing time. In actual geometries, there are small manufacturing or assembling tolerances which are believed to contribute to the onset of rotating stall at specific locations in the compressor rotor or stage assembly. Numerical geometries resulting from repeating a single passage mesh are, however, perfectly symmetric. Previous numerical simulations on perfectly symmetric assemblies, expected to experience rotating stall, showed that rotating stall simulations are possible; however, this requires many rotor rotations before the onset of rotating stall happens. It is likely that accumulated floating point errors eventually lead to some differences among passages and hence rotating stall may start. It is also found that introducing small asymmetry of the same order of manufacturing tolerances could lead to a much quicker onset of rotating stall in the numerical simulations resulting in significant computer time savings. In this case, all blades as shown in Figure 4.1 were arbitrarily staggered between -0.2° and 0.2° which is within the manufacturing tolerances, to create some asymmetry and thus reduce the number of rotor revolutions required for the initiation of rotating stall.

The chosen operating condition is the near stall point predicted from steady state simulation. That performance point (Rotor speed: 10313.2 rpm, mass flow: 10.09 kg/s, pressure ratio: 1.286) is labelled as A in Figure 4.3. Then it was used

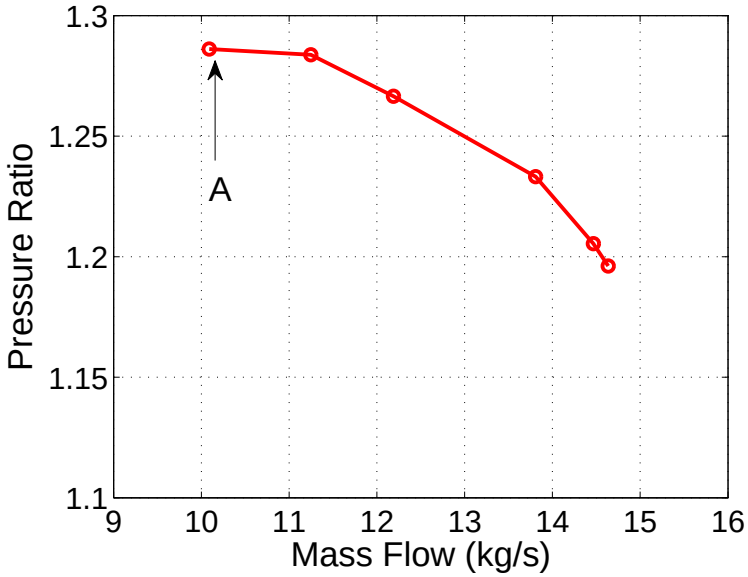

Figure 4.3: Steady state solution at 60% of rotor speed

as a starting solution for the unsteady simulation. The unsteady simulation of one rotor revolution requires approximately 25 hours real time using 32, 2.5 GHz Intel Xeon cores. For reference, approximately 1350 time steps per rotor revolution were used in all unsteady simulation for this rotor. Unsteady simulation away from stall boundary will be discussed first in the next section.

4.3 Unsteady simulation away from stall boundary

Before investigating flow behaviour at near stall boundary, an unsteady simulation is performed away from stall boundary to verify the unsteady simulations compared with the steady state solution at the same operating condition. Eight sets of numerical sensors were chosen in the stationary frame upstream of the rotor. The circumferential positions of those sensors are shown in Figure 4.4. Numerical sensors at the same locations are used for all unsteady simulations. They are all placed at approximately 76% of chord length upstream the leading edge of the rotor and 45 degrees apart in the circumferential direction. In the radial direction, each set

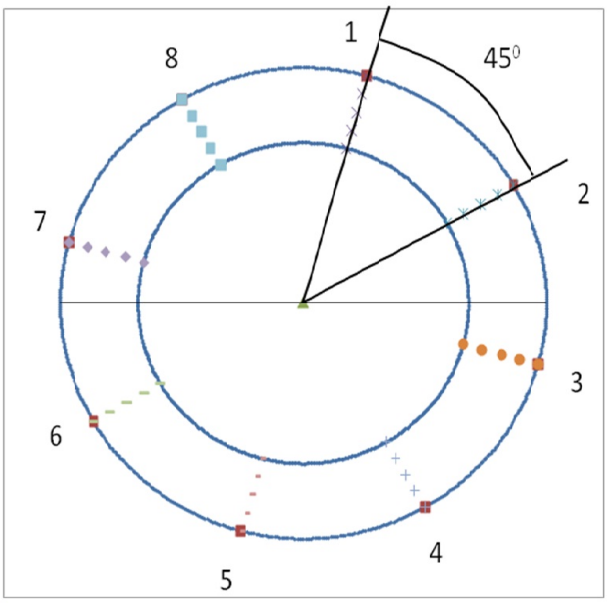

Figure 4.4: Circumferential positions of numerical sensors

contains five sensors equally spaced with one on the casing and one on the hub.

Figure 4.5 shows the unsteady static pressure history from eight numerical sensors on the casing which are labelled as n1, n2, ..., n8, the pressure fluctuation caused by the blade-passing is the main fluctuation observed which shows the periodicity over few rotor revolutions. The lower plot shows the time history for one rotor revolution. There are 36 spikes which indicate 36 rotor blades passing the same sensor in one rotor revolution. This information can be also seen in the Fourier Transform components for the pressure signal shown in Figure 4.6. The dominant frequency is blade passing frequency (BPF) which is the same as the expected value.

The time averaged solutions from this case were also compared with the steady state results. The maximum difference of main flow parameters is less than 0.2%, including mass flow, pressure ratio and isentropic efficiency. Pressure profiles at different spans are also compared with the steady state solution which are shown in Figure 4.7. As seen from the figure, pressure profiles of unsteady solution are very similar to the ones from steady state solution which further validates the unsteady features of the code.

To examine the flow behaviour in the rotor, Figure 4.8 shows the instantaneous

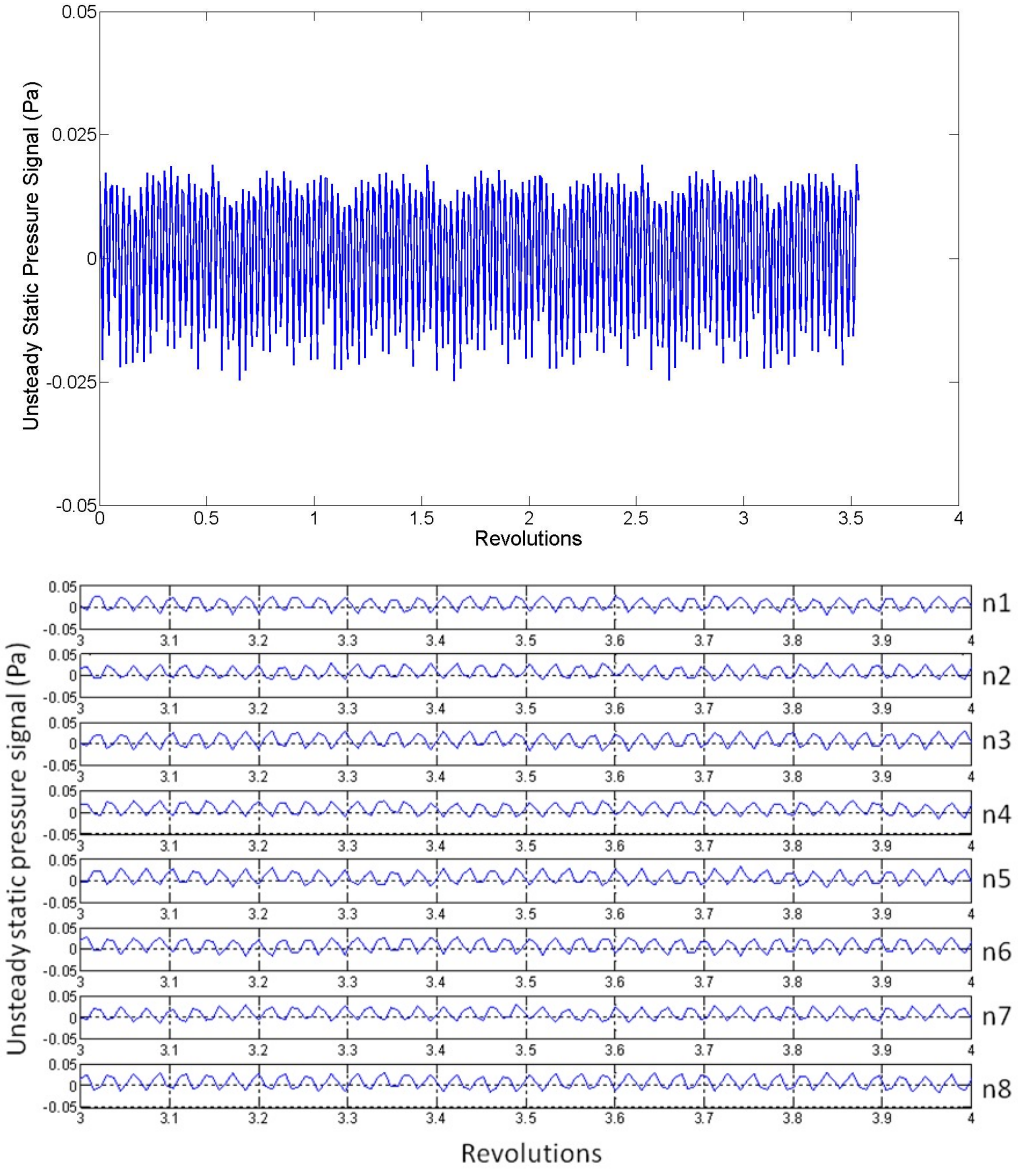

Figure 4.5: Unsteady static pressure history at the inlet of rotor without rotating stall

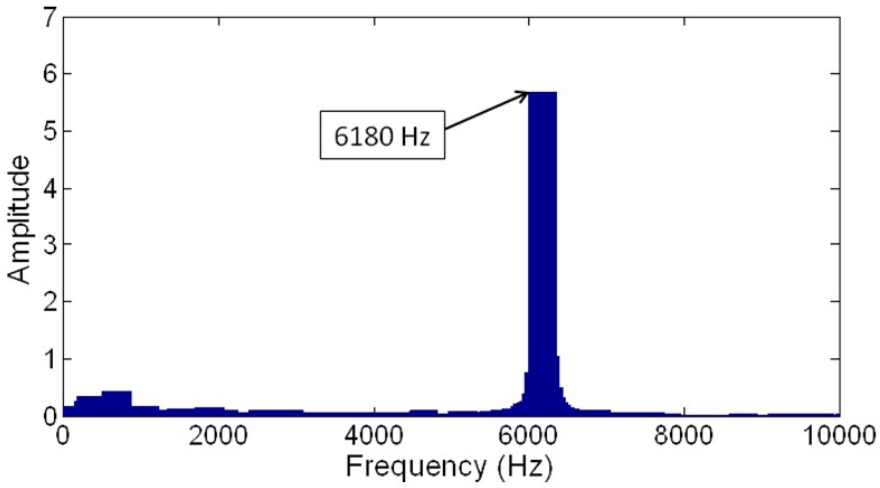

Figure 4.6: Fourier Transform components from one of the numerical sensors

static pressure of the inlet boundary of the rotor domain and Figure 4.9 shows the instantaneous axial velocity near the tip of the rotor. As seen, the flow is axisymmetric and there is no disturbance predicted in the rotor. Animations also show that flow in the rotor is axisymmetric and periodic after the initial transient. Figure 4.10 shows the streamline structure inside the rotor passage which is contoured by the axial velocity. As seen, flow is passing the passage smoothly without blockage or separation. To sum up, the unsteady solution away from stall boundary matched well with the steady state solution. It also predicted the expected BPF and flow behaviour in the rotor. The time accurate unsteady simulation with nominal blade settings near surge boundary will be presented in the next section.

4.4 Unsteady simulation near stall boundary

In this section, the case operating at near stall boundary is discussed. The overall compressor performance during rotating stall is shown with the steady state solution in Figure 4.11. The unsteady mass flow shown in the figure is obtained in the last 10 revolutions of the simulation. The mass flow rate with rotating stall is approximately 0.6% lower than the steady state solution and the pressure ratio decreased by approximately 1% which are caused by the rotating stall. It seems that

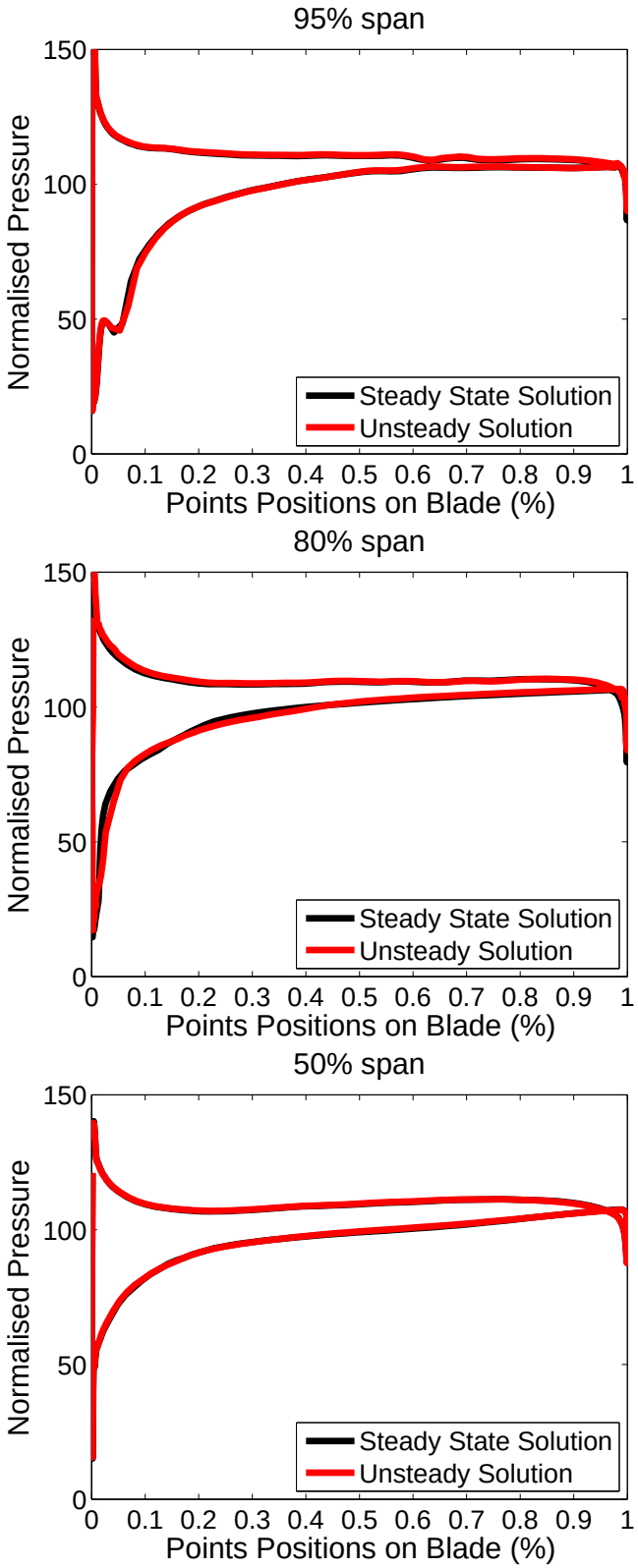

Figure 4.7: Pressure profiles comparison between steady and time averaged unsteady solution

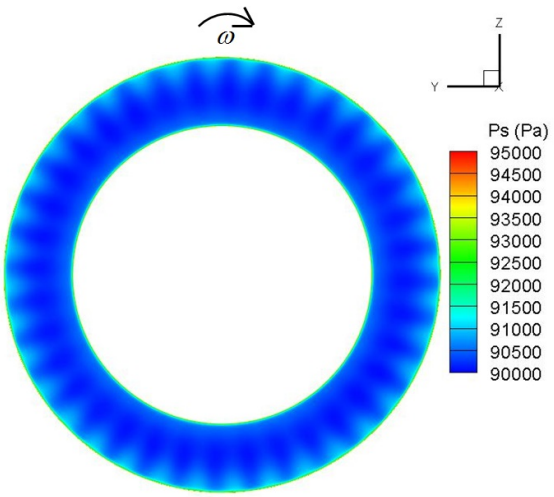

Figure 4.8: Instantaneous static pressure contour plot at the upstream of the rotor

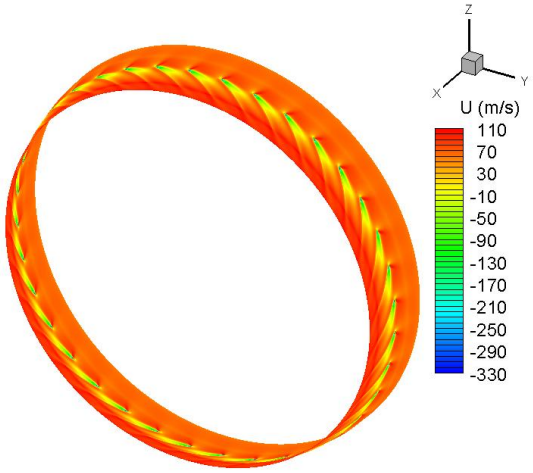

Figure 4.9: Instantaneous axial velocity contour plot near the tip surface of the rotor

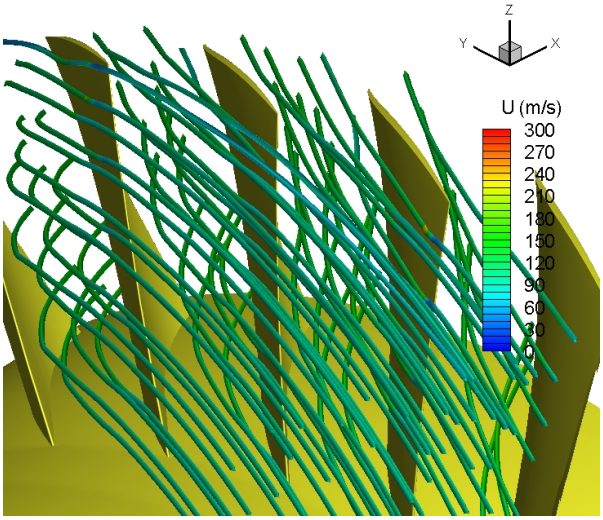

Figure 4.10: Instantaneous streamline structure inside the rotor

mass flow was less affected compared with the pressure rise. Furthermore, when a fully developed rotating stall pattern was achieved, mass flow was redistributed and settled leading to a condition that it had a very small fluctuation range with time.

The circumferentially averaged axial velocity profile comparison at the downstream of Rotor 37 is shown in Figure 4.12. It can be seen that from approximately 75% span to the casing, the averaged axial velocity during rotating stall was higher than that obtained from the steady state solution with no stalled cells, which is in the contrary to expectations. Further investigation of the detailed flow behaviour allows explaining this however. Figure 4.13 shows the Mach number contour comparison at 75% span of Rotor 37. The steady state solution was assembled from single passage for comparison reasons. It can be seen that in the area adjacent to the unstalled passages, the Mach number is higher than that in the steady simulations due to low or negative incidence. This indicates higher mass flow through unstalled passages in the upper part of the passage, which appears to compensate for the mass deficit in the stalled regions and the lower part of the passage. The averaged axial velocity from 75% to 18% span was lower than the steady state solution. The reason is that the flow in that region, especially the flow areas just below the rotating stall cells, was affected by the stalled flow resulting in lower averaged

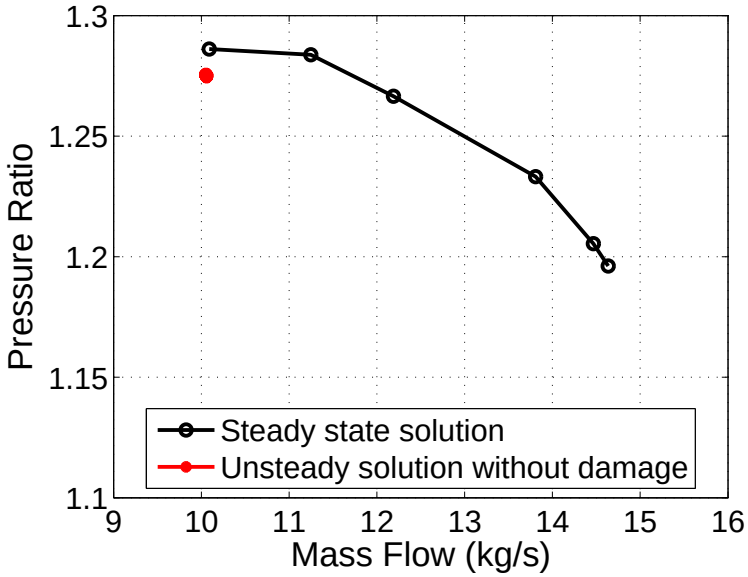

Figure 4.11: Compressor performance during rotating stall

axial velocity. Until 18% span, flow was not affected by the stalled flow leading to the flow recovery. From 18% span to hub region, the flow profile was similar and with slightly higher velocity for the unsteady undamaged case.

Figure 4.14 shows the unsteady static pressure signal time history from eight numerical sensors located at different circumferential positions on the casing. Spike type rotating stall was predicted for this case. Three different types of spikes were observed indicating three different patterns of rotating stall. As seen in the figure, after the initial numerical transient was settled, the first pattern of rotating stall started after six revolutions. It lasts 16 revolutions until a new rotating stall pattern was observed. After another 18 revolutions, a regular stall pattern was achieved which indicates that the rotating stall was fully developed. The regular pattern consists of six rotating stall cells. Figure 4.15 presents pressure signal in one rotor revolution. In the figure, five stall cells passed the same sensor during that period. The Fourier Transform components from one of the numerical sensors are shown in Figure 4.16 which was obtained after the regular rotating stall pattern is achieved. As seen in the figure, there are three main frequencies: 852 Hz, 1700 Hz and BPF. The first frequency is the frequency of the propagation for rotating stall cells and

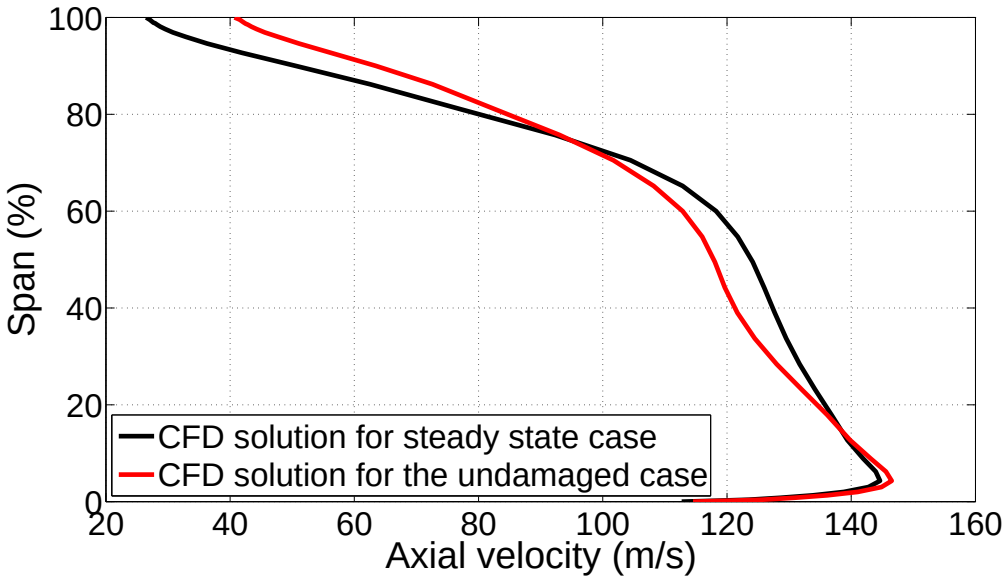

Figure 4.12: Circumferentially averaged axial velocity profile comparison at the downstream of Rotor 37

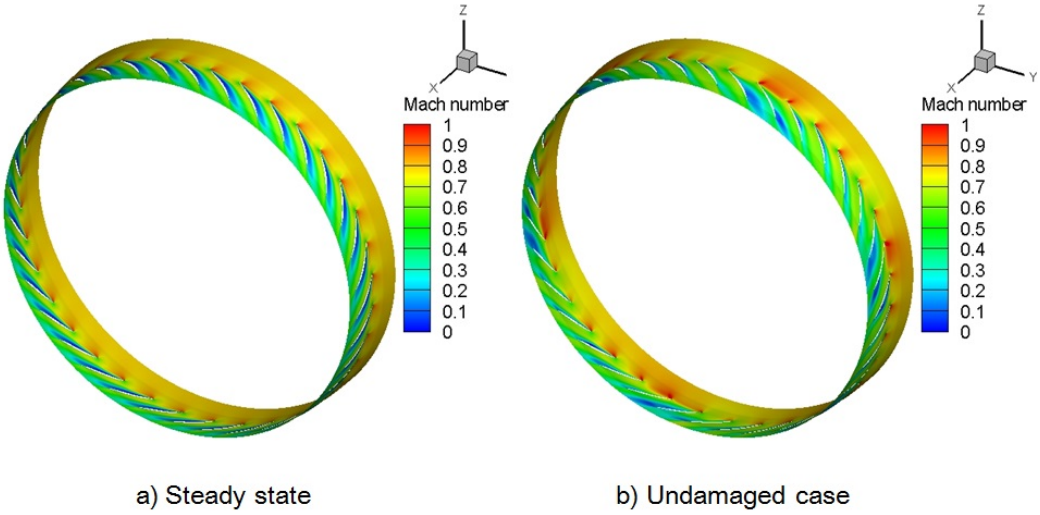

Figure 4.13: Mach number contour comparison at 75% span of Rotor 37

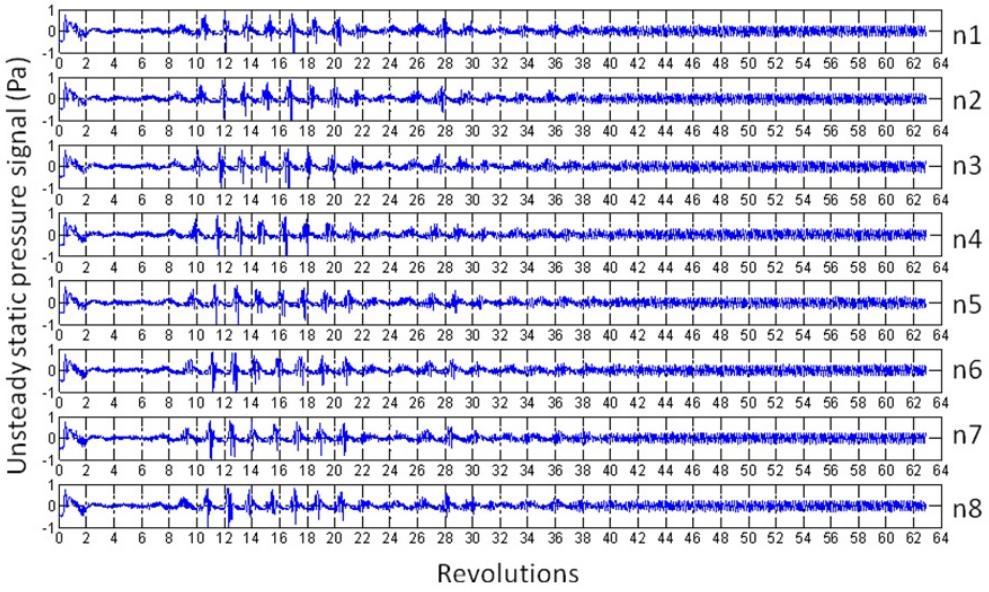

Figure 4.14: Unsteady static pressure signal full time history from numerical sensors on the casing

the second one is its second harmonic. Therefore, the propagation speed of rotating stall could be worked out to be 83% of rotor speed.

As mentioned in Chapter 2, there are three aspects to investigate for rotating stall: inception, development and fully developed pattern. Although there are no experimental data to compare with, it is still worthwhile to show its development in order to study rotating stall characteristics. 6 small stall cells were found at the 2nd revolution which are shown in Figure 4.17. At the 2nd revolution, those stall cells covered approximately one passage. After 4 revolutions, small stalled regions exist in many passages. At the 14th revolutions, they evolved into two large stall cells and some smaller cells. In the lower half of the annulus, there was one stall cell covering one passage; while in the upper half of the annulus, there was one large stall cell covering 4 passages which extended to the outlet of the rotor and an even larger stall cell covering 8 passages. There were also 4 smaller cells with each one covering one passage. At the 22nd revolution, those large stall cells split into 8 small cells, 5 of them covered 2 passages each and the rest covered one passage. There were also 8 stall cells found at the 32nd revolution and they were more spaced away from each other than those found at the 22nd revolution. At the 42nd revolutions, a regular

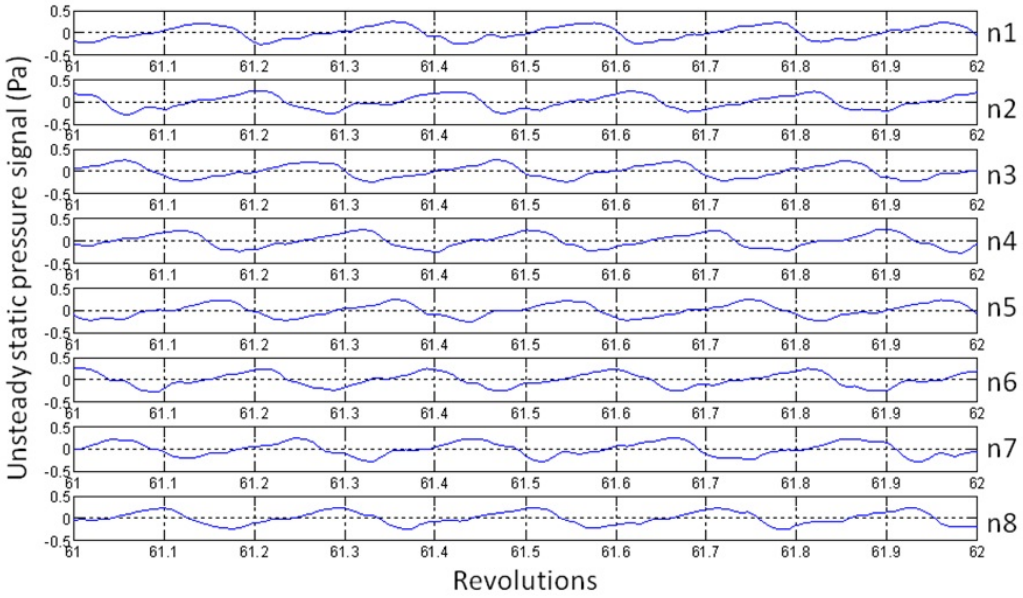

Figure 4.15: Unsteady static pressure signal from numerical sensor 1 on the casing in one rotor revolution

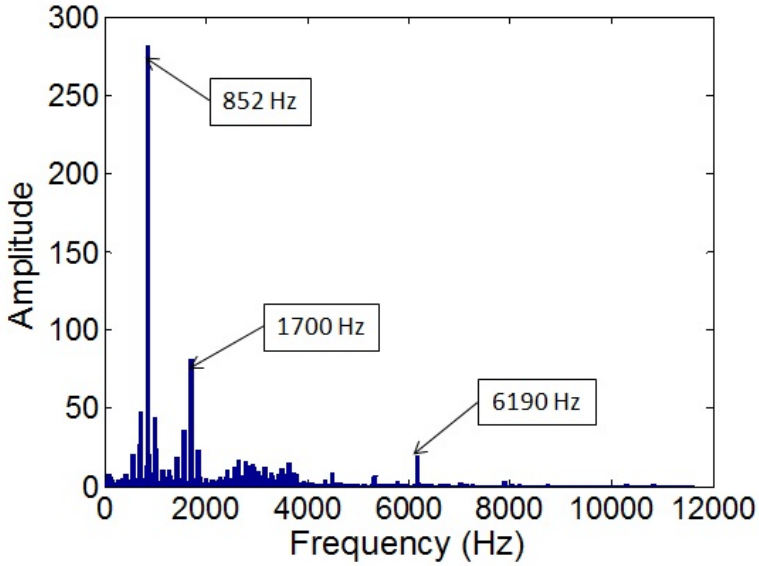

Figure 4.16: Fourier Transform components from numerical sensor 1

rotating stall pattern with 6 cells was already established and those stall cells were approximately equally spaced which covered two passages and were 4 passages away from each other. To sum up, the first stall pattern was found in the annulus after 6 revolutions; then it developed to large stall cells covering several passages and several small stall cells; then the large stall cells starts to split into small stall cells which covers less passages and were close to each other; finally the space between those cells varied until they were approximately equally spaced and the number was reduced to six.

To demonstrate span-wise coverage of stall cells, it can be referred to Figure 4.18 which shows the negative axial velocity on an axial cut plane in the rotor at the same time after a clear pattern achieved. The axial cut plane is at 40% of chord length downstream from the leading edge on the hub. Each cell covered approximately two blade passages in the circumferential direction. It also shows that stall cells were equally spaced in the circumferential direction and cover approximately 17% in radial span from the tip. It can be concluded that rotating stall cells were found only near the tip region of rotor blades. That is one characteristic of spike type rotating stall reported by Day [1993] which shows that stall cells tend to be confined to the tip region of the rotor suggesting that tip clearance flow may be responsible for its inception. Spike type disturbances have also been experimentally measured to have a circumferential extent of two to three blade passages (Day [1993], Silkowski [1995] and Day and Freeman [1994]).

Rotating stall for this rotor at design speed was investigated by Zhang et al. [2010] using multi-passage model. In that study, rotating stall predicted also has 6 stall cells with a propagation speed of 80% of the rotor speed based on the available data. Rotating stall cells covered approximately 40% span of rotor blades and approximately 4 passages in the circumferential direction. The span-wise extent of rotating stall is larger than the present study which could be caused by the interaction between shock waves, boundary layer and tip clearance flow at design speed while present predictions are performed at 60% of the design speed. In addition,

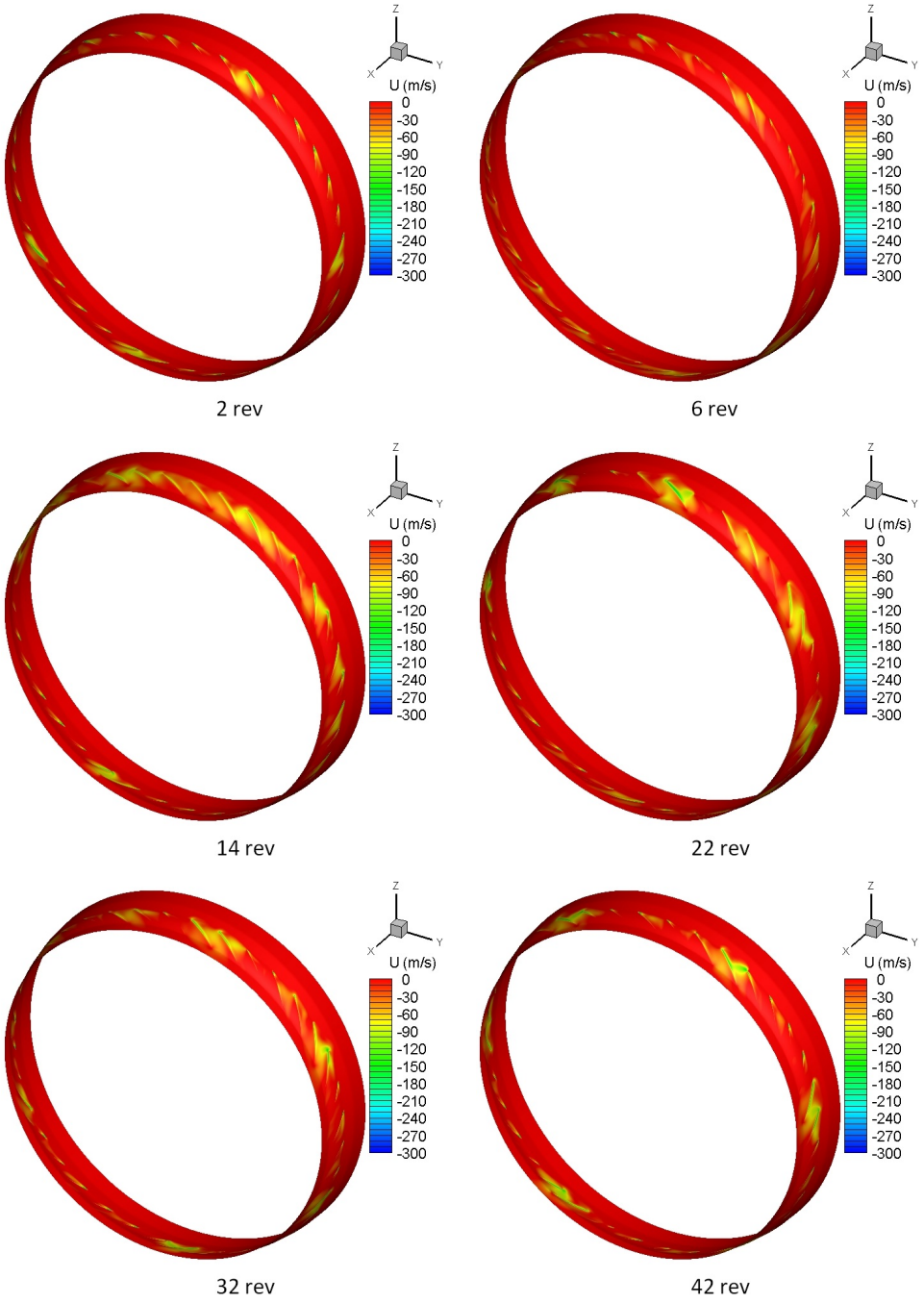

Figure 4.17: Development of rotating stall cells

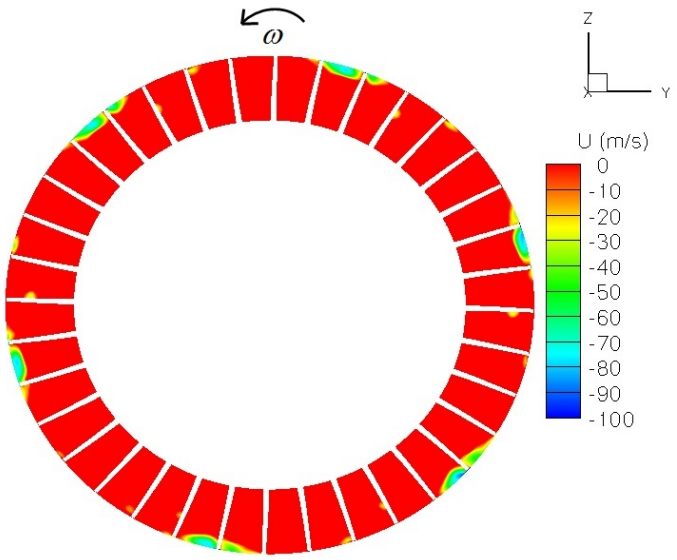

Figure 4.18: Instantaneous negative axial velocity on an axial cut plane

their simulations were performed over two engine revolutions only and the solution could have developed to a different pattern if the simulations were continued beyond that.

The 3D streamlines with contours of negative velocity were demonstrated in Figure 4.19. The inflow came from the leading edge of one blade, and the back flow was reversed at the leading edge of the neighbouring blade and into the passage. It met the tip clearance flow and the vortex of the stall cell. The interface of inflow with tip clearance flow was aligned with the leading edge plane. This confirms the flow feature for the spike initiated rotating stall proposed by Vo et al. [2008]. Inside the stall cell the blocked flow diverted the inflow in the neighbouring area. Outside the stall cell, flow was passing the passages smoothly without blockage. The stall cell was also in the form of a radial vertex attached to the blade and the casing which confirms that rotating stall is three-dimensional in nature. The concept of radial vortex was proposed by Inoue et al. [2000] and also recently confirmed by Weichert and Day [2012] and Pullan et al. [2012]. The similarity of the flow characteristics compared to those studies is that due to the design of this rotor, some blades encounters higher positive incidence beyond the critical value near the tip region which leads

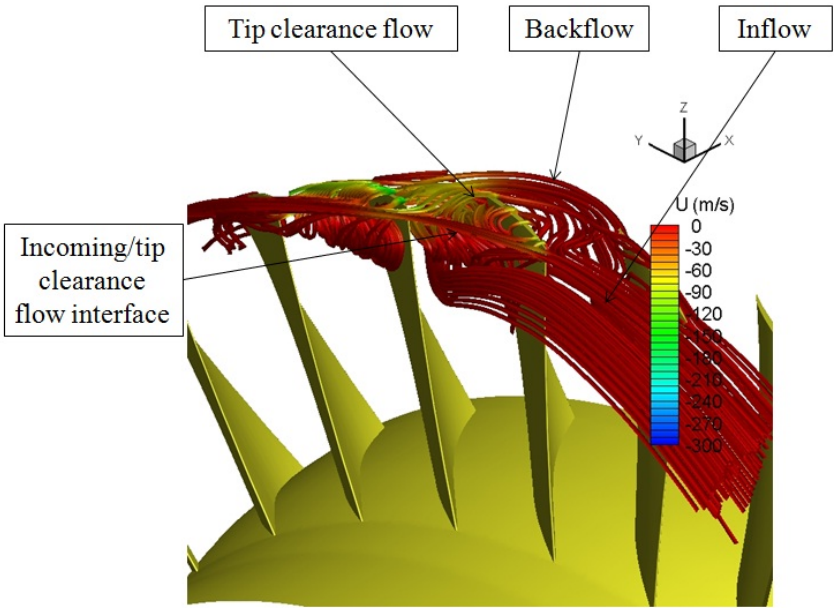

Figure 4.19: 3D streamline inside the stall cell

to separations from the suction side. The stalled region constitutes a radial vertex attached to the suction side of the blade and the casing. As shown in Figure 4.19 in the rotor reference frame, when the cell was propagating in the anticlockwise direction, the vortex would leave the suction side of one blade and move towards the pressure side of the next blade which would divert the flow in the surrounding. Also the stall cell indicates a pressure building up which forms the spike in the unsteady pressure signal time history. Furthermore, compared with stall cells found by Pullan et al. [2012], the location of stall cells was in the rotor passage rather than close to the leading edge. That could be the interaction between tip leakage flow over the blade and stall cell near the tip region due to the particular design of the rotor blade. The hub to tip ratio of Rotor 37 is much lower and since this is also a high speed compressor with more twisted angle near the tip which makes tip clearance flow is essential for inception of rotating stall.

4.5 Summary

In this chapter, time-accurate unsteady full annulus simulations were discussed. A transonic axial flow compressor, NASA Rotor 37, was used. Simulations were

performed at 60% of rotor speed. A case operating away from stall boundary was discussed first. Time averaged solutions were compared with steady state solution with the same inlet and outlet boundary conditions. Results show that they have very good agreement including overall performance and pressure profiles on the blades at different spans.

Then another case without any damaged blades operating at near stall boundary was discussed. From the overall performance, mass flow rate is 0.6% lower than the near stall point from steady state solution and has a small variation range with time after a fully developed rotating stall pattern is achieved while pressure ratio is reduced by 1%. Mass flow was less affected and the reason could be that it was compensated in other unstalled regions after the flow redistribution. Contrary to expectation, the circumferentially averaged axial velocity near the tip region with rotating stall was higher than the steady state solution. It was result from that more mass flow was achieved in the unstalled passages near the tip due to reduced incidence which compensated the deficit from the stalled passages.

Part span spike type rotating stall was predicted in this case. From the initiation to the fully developed pattern, three different rotating stall patterns were observed which could be seen from the pressure signals, mass flow variation history and flow animations. The regular pattern has 6 stall cells which rotate along the rotor annulus in the same direction of rotor rotation with a propagation speed of 83% of shaft speed. That is different from the investigation of this rotor at design speed as reported by Zhang et al. [2010] which showed that a part span rotating stall also with 6 cells but with more radial extent was found with a propagation speed of 80% of rotor speed. The mechanism of this type of rotating stall is consistent with proposals reported by Vo et al. [2008]. Stall cells are approximately equally spaced and covers two rotor passages in the circumferential direction and approximately 17% in the span. The similarity of flow feature regarding to radial vortex and its propagation mechanism conforms to those reported in the literature.

Chapter 5

Blade damage effects on compressor performance

5.1 About this chapter

In this chapter, compressor performance of NASA Rotor 37 was investigated with tip curl damaged blades. This chapter is the second part of the blade damaged study. To study the effect of blade damage, assemblies with both different degrees of one damaged blade and multiple damaged blades were analysed. All unsteady simulations discussed in this chapter were performed at 60% of the design speed. With one medium damaged blade, the investigation was performed at two operating conditions: one away from stall boundary and the other near stall. Assemblies with one heavy damaged blade and multiple damaged blades were only performed near stall boundary. Then results were compared with solutions from the assembly without any damaged blades presented in Chapter 4.

5.2 Computational geometry

In this chapter, rotor assemblies with damaged blades were achieved by repeating original Rotor 37 blades assembled with the chosen damaged blade(s) in the circumference. The model for steady state computations is shown in Chapter 3. The

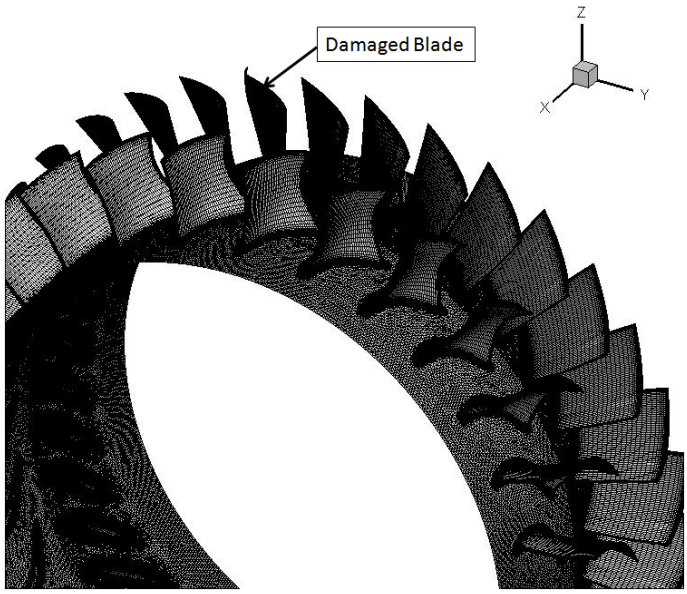

Figure 5.1: Partial view of mesh used for unsteady computation with one medium damaged blade

computational geometry for unsteady simulation is very similar to the one used in Chapter 4. It consists of the same components however with damaged rotor blade(s). To investigate the effects of different degrees of the damaged blade, only one damaged blade is introduced into the rotor assembly. All computational domain presented in this chapter contains approximately 10 million points which is partially demonstrated with one damaged blade in Figure 5.1.

Two different degrees of damaged blades were used in this research which are shown in Figure 5.2. One is with medium damage and the other is with heavy damage. Each damage was made from the leading edge to 20% of the chord length in the stream-wise direction on the tip and from 70% span increasing its span-wise extent linearly up to the tip which forms a typical curl damage. Figure 5.2 (c) shows the comparison of blade section near the tip section which has the maximum change in blade profile.

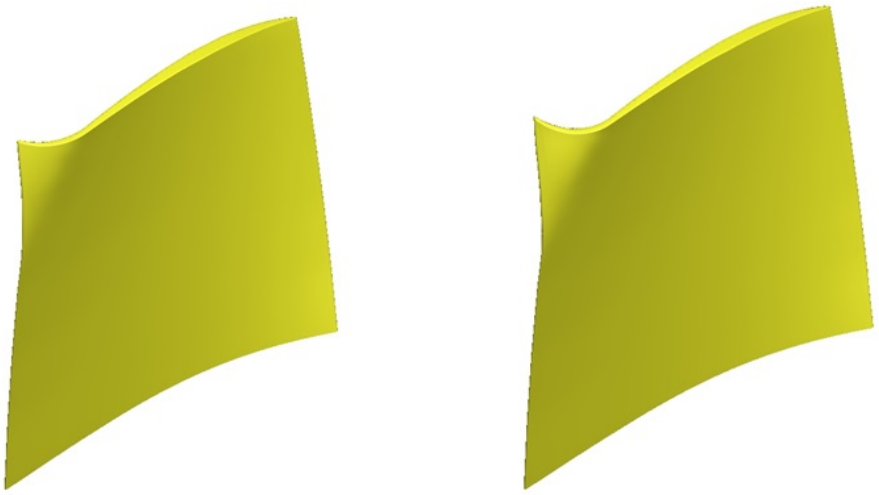

a) Medium damage b) Heavy damage

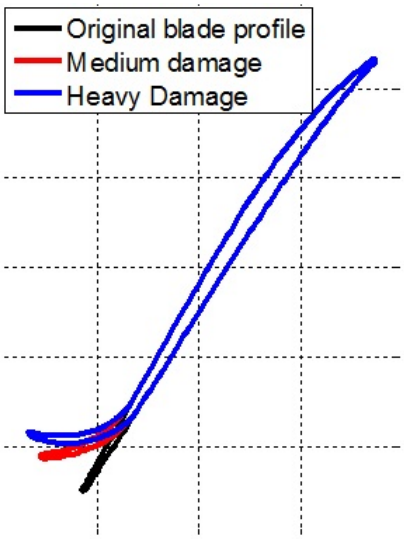

c) Blade profile comparison near the tip

Figure 5.2: Views of damaged blades

5.3 Unsteady simulation away from stall boundary with one damaged blade

Before the investigation of blade damage effects near stall boundary, another case with the medium damaged blade was investigated which was performed away from stall boundary at 60% speed. Compared with the solution obtained in the case operating at the same condition without any damaged blade, the overall performance for mass flow, temperature ratio and isentropic efficiency are the same. Pressure ratio differs the most however the difference is less than 1%. It could be concluded that the global performance was not significantly affected by the damaged blade. Flow blockage was only found in two passages including the damaged blade and flow seems to be compensated in other passages after its redistribution. Figure 5.3 indicates the circumferentially averaged axial velocity profile comparison away from stall boundary. It can be seen that the averaged axial velocity near the tip region from the casing to approximately 90% span was slightly lower for the case with one damaged blade which is as expected. The reduction of flow in that region was caused by the flow blockage due to the damaged blade. The mass flow for the case with one damaged blade seemed to be compensated in the region between the mid span to 90%. Since there was only one damaged blade in the rotor assembly, it result in no significant change in mass flow.

As seen in the unsteady static pressure history in static frame in Figure 5.4, except the blade passing signal, the larger spike indicates that the damaged blade was passing the numerical sensor. In the lower plot, it shows the pressure history in one rotor rotation. There are 34 smaller spikes and the larger spike. Rotating stall was not predicted in this case. Figure 5.5 shows an axial cut plane upstream the rotor contoured by the axial velocity. The discontinuity of contour shown in the figure indicates the flow blockage caused by the damaged blade. Furthermore, Figure 5.6 shows the instantaneous axial velocity at 95% span. As seen in the figure, two passages are stalled covering the damaged blade and more flow goes into

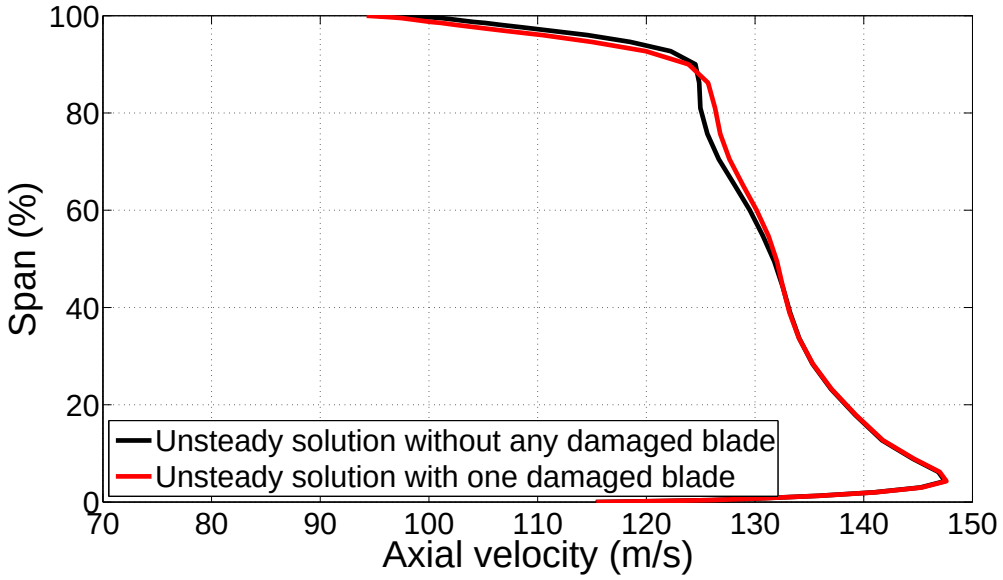

Figure 5.3: Circumferentially averaged axial velocity profile comparison away from stall boundary

neighbouring passages. As seen from the animation, flow was always stalled in that region. With two to three passages on both sides of the flow blockage in both figures discussed above, axial velocities were higher in those regions which represented the flow compensation. This could be the reason why mass flow is not affected by the damaged blade.

5.4 Effects of different degrees of damage of one blade

In this section, the investigation of the effect of different degrees of one damaged blade will be presented. The case with one medium damaged blade and heavy damaged blade are labelled as Damaged Case 1 and Damaged Case 2 respectively. The undamaged case representing the assembly without any damaged blade was discussed in Chapter 4. Both cases with damaged blade have the same inlet and outlet boundary conditions as the undamaged case. Part span spike type rotating stall was observed in both cases. The comparison of compressor performance during

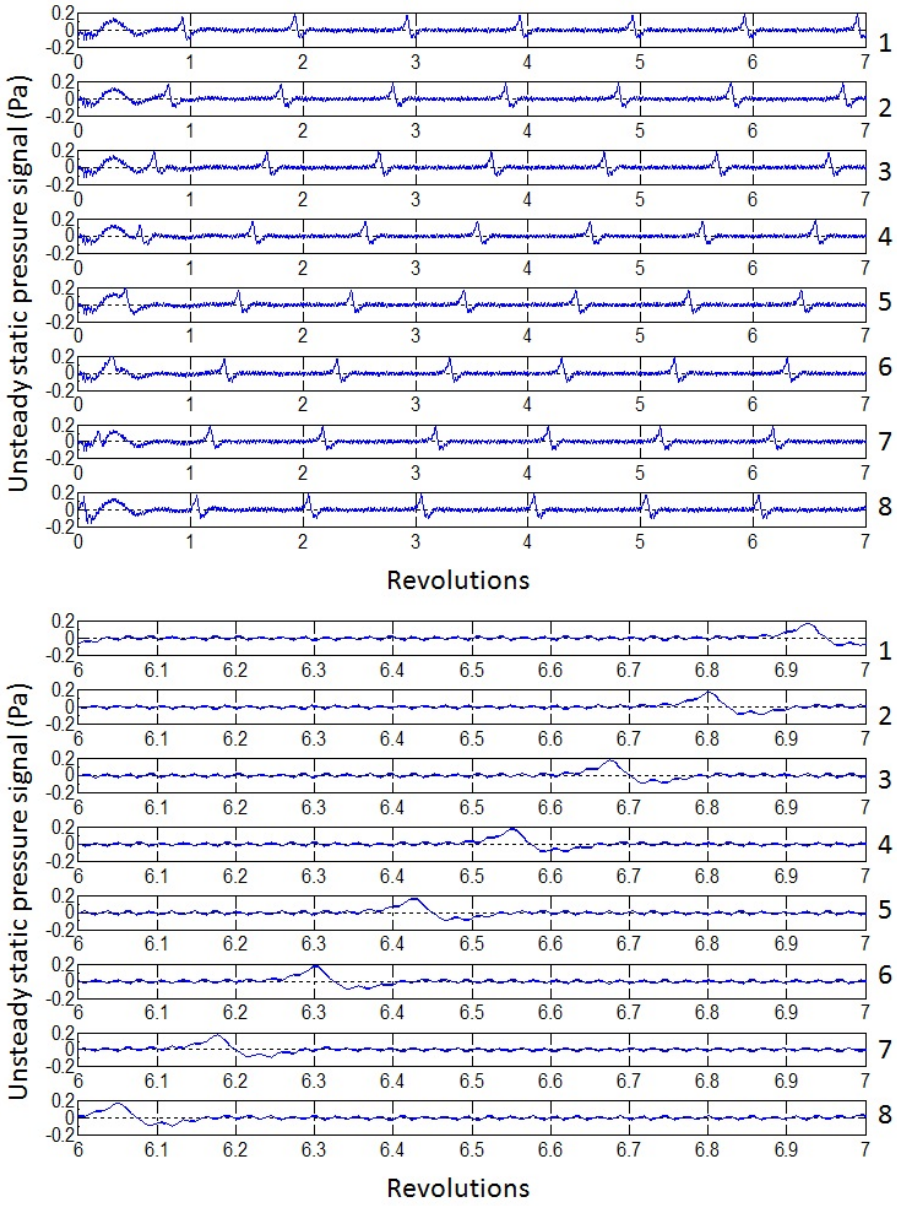

Figure 5.4: Unsteady static pressure history at the inlet of rotor without rotating stall

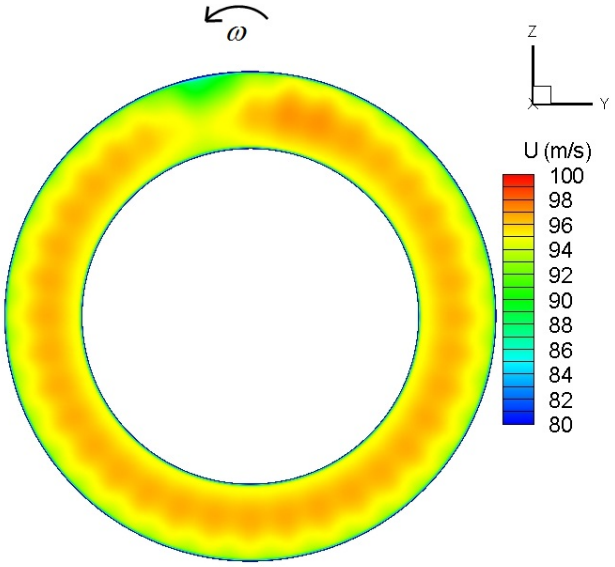

Figure 5.5: Instantaneous axial velocity on an axial cut plane upstream the rotor

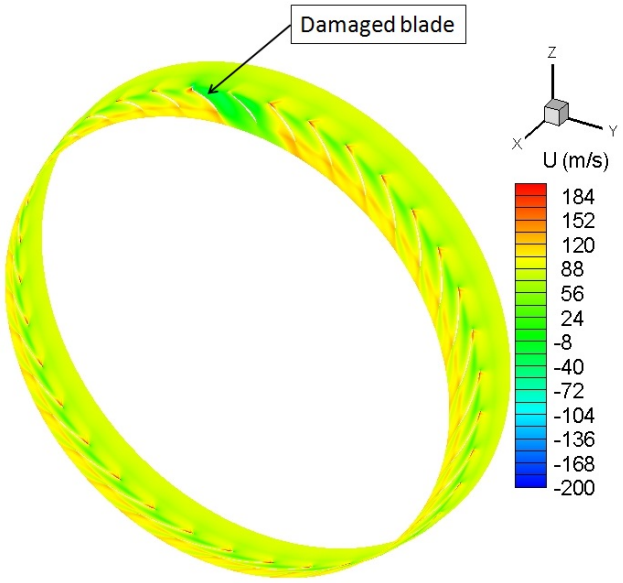

Figure 5.6: Instantaneous axial velocity at 95% of rotor span

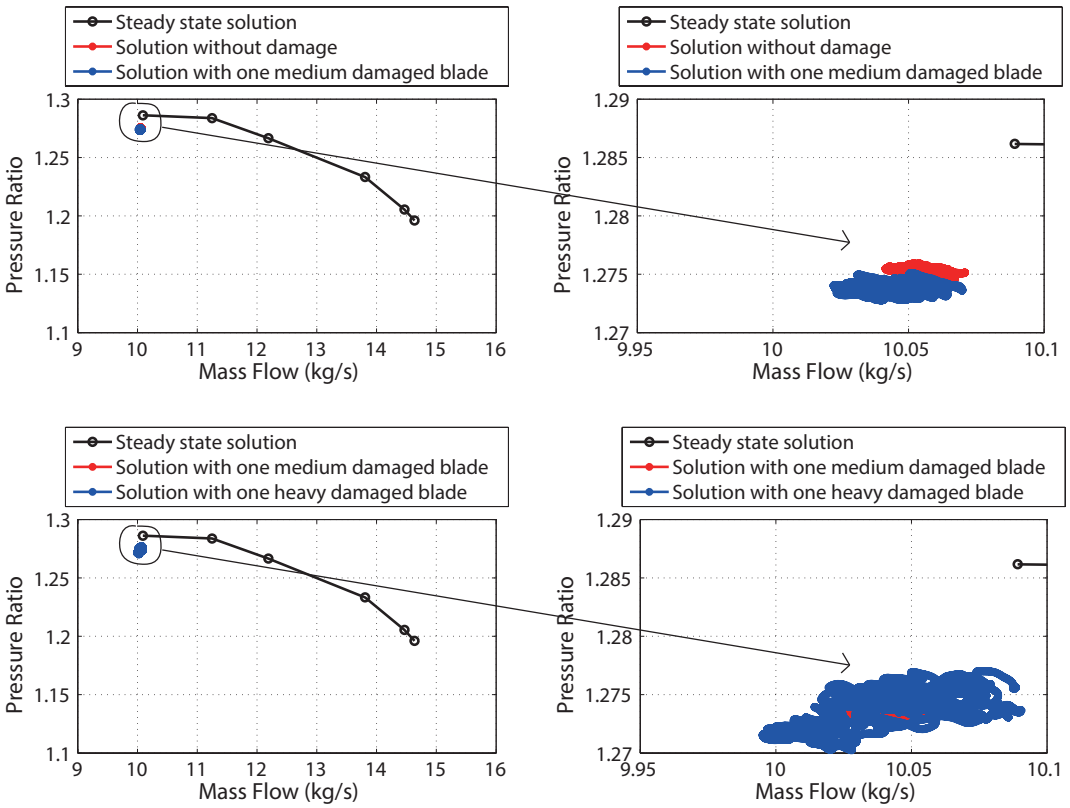

Figure 5.7: Compressor performance during rotating stall

rotating stall with regular patterns is shown in Figure 5.7. Here, the regular patterns refer to fully developed rotating stall pattern with repeating periodicity within few rotor rotations. For Damaged Case 1, the overall compressor performance is very similar for the mass flow while pressure ratio is slightly lower, compared with the undamaged case. For Damage Case 2, it has slightly larger variation for mass flow and pressure ratio than Damage Case 1. However, the time averaged value for both mass flow and pressure ratio was the same for both damaged cases. It seems that rotating stall predicted in both cases could not cause significant decay in the overall compressor performance. Mass flow varied in a small range of fluctuation with time for both cases after its redistribution in the compressor.

The circumferentially averaged axial velocity profile comparisons at the downstream of Rotor 37 for both cases are shown in Figure 5.8. Both profiles for Damaged Case 1 and Damaged Case 2 are very similar to the undamaged case. The averaged mass flow near the tip is slightly lower than the undamaged case for Damaged Case

2 due to increased blockage by the higher degree of damage of the blade in that region. Flow is compensated in other unstalled regions where the undamaged blades compensate for the loss resulting from the damaged blade, the same as discussed in Chapter 4. As also seen in that figure, the division between the region affected by the damaged blade and the flow compensation is at 60% span for both cases. Flow features are the same in that radial position which will not be shown here.

The same numerical sensors are used as the ones for undamaged case, described in Chapter 4. It was predicted that stall cells started from the damaged blade and rotated in the opposite direction to rotor rotation observed in the relative frame of reference. For Damaged Case 1 in Figure 5.9, after the initial numerical transition, spike type rotating stall started after 2 revolutions. A more stable stall pattern was formed after 10 revolutions with 6 stall cells. Then the transition process of 18 revolutions took place until a final pattern was established after 30 revolutions. Compared to the undamaged case, it took less numbers of rotor rotations to achieve a regular form of rotating stall. For Damaged Case 2 in the lower plot in Figure 5.9, when increasing the damage, it took more rotor rotations for the flow to settle. Figure 5.10 presents a comparison of unsteady static pressure time history in one rotor rotation. It can be seen that 5 and 6 cells passed the same sensors in that period for Damaged Case 1 and Damaged Case 2 respectively. There are small kinks at the beginning of some of the spikes for both cases, circled on the plot. It is believed to be the effect that the cell just passed the damaged blade. Compared to the undamaged case, the rotating stall characteristic is the same for Damaged Case 1. For Damage Case 2, one more rotating stall cell was predicted.

Figure 5.11 shows the Fourier transform of static pressure full time history from one sensor on the casing for Damaged Case 1. Other than the blade passing frequency, two other frequencies are also predicted: one is 850 Hz and the other is 1,700 Hz. It is clear that the former is the frequency of rotating stall while the latter is its second harmonic. It can be worked out that rotating stall has a propagation speed of approximately 83% of rotor speed which is the same as the undamaged

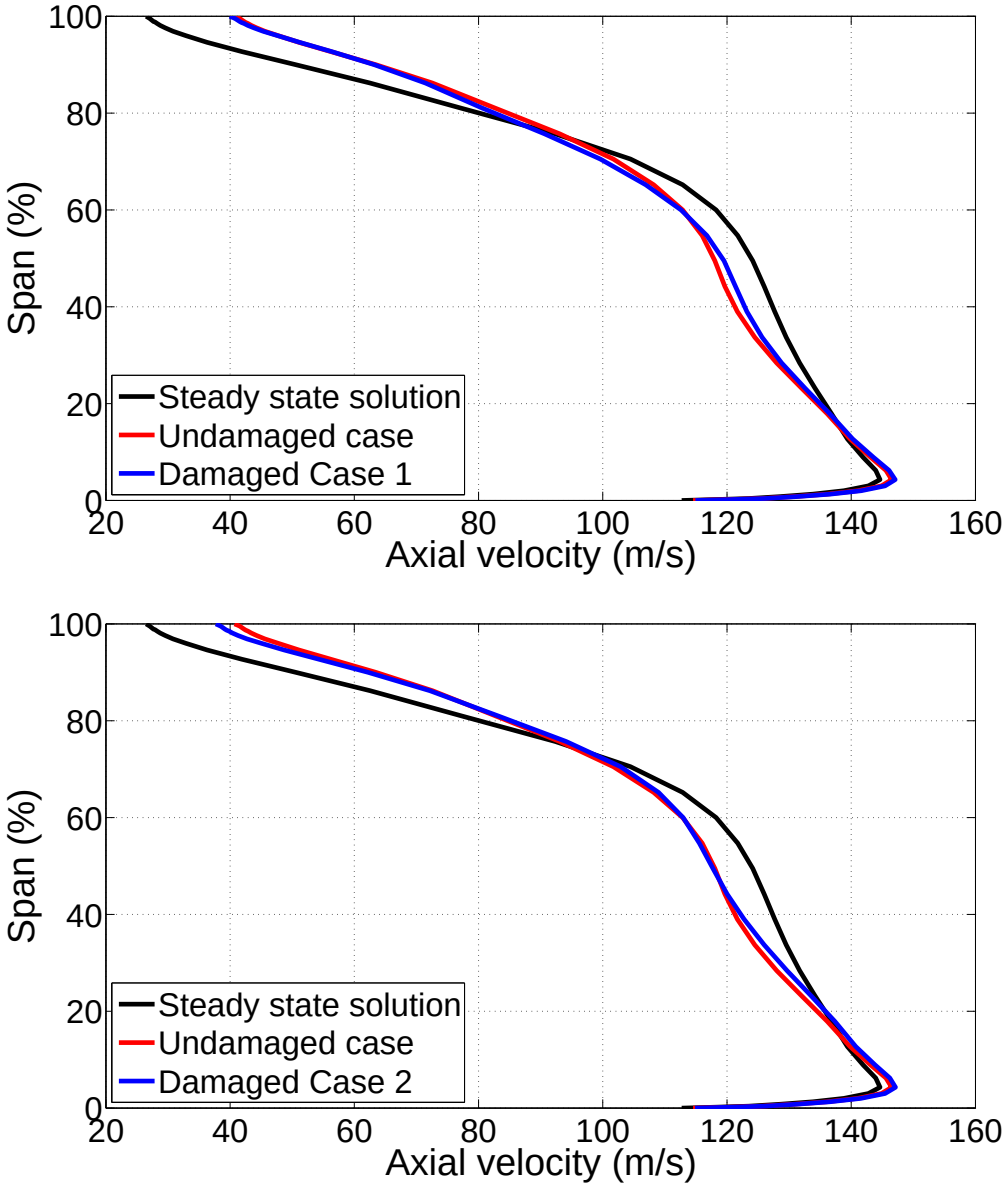

Figure 5.8: Circumferentially averaged axial velocity profile comparison at the downstream of Rotor 37

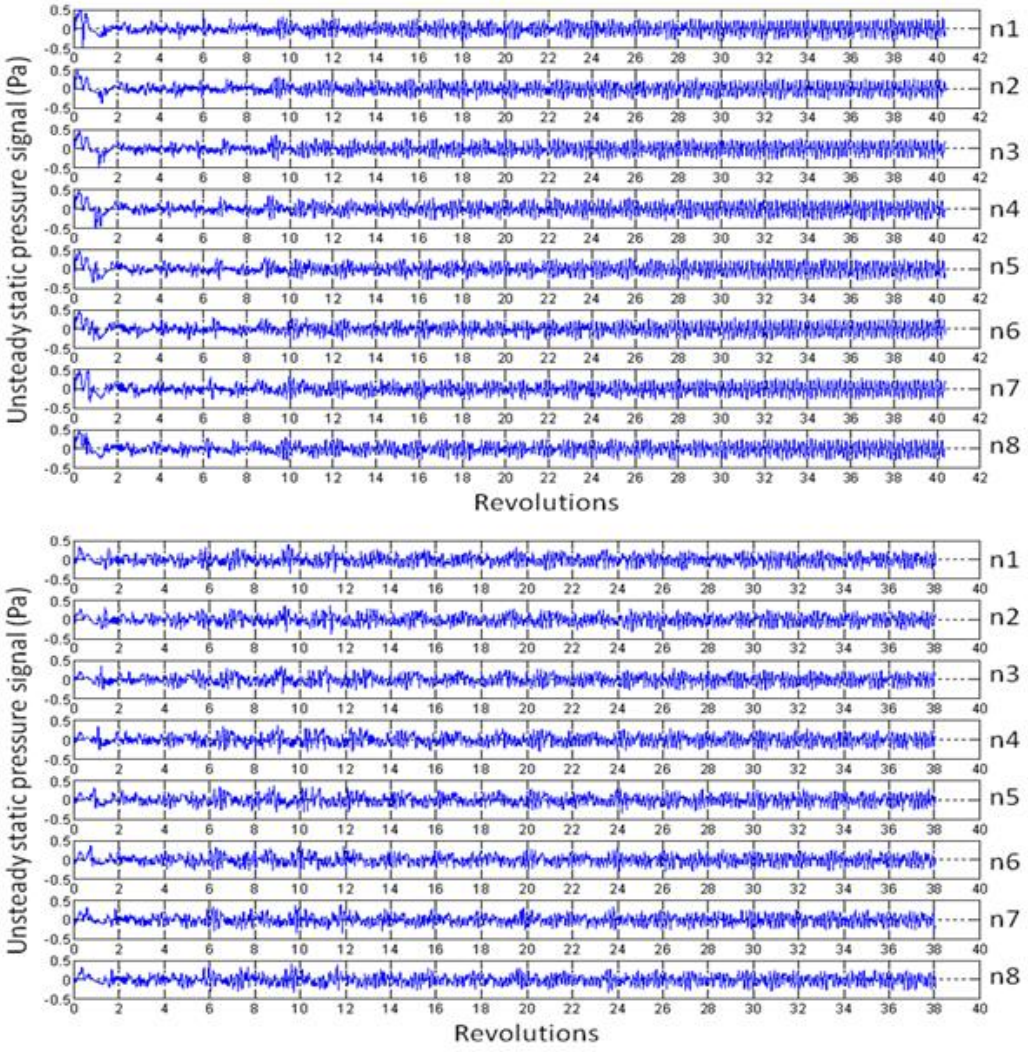

Figure 5.9: Unsteady static pressure full time history comparison (Up: Damage Case 1, Down: Damage Case 2)

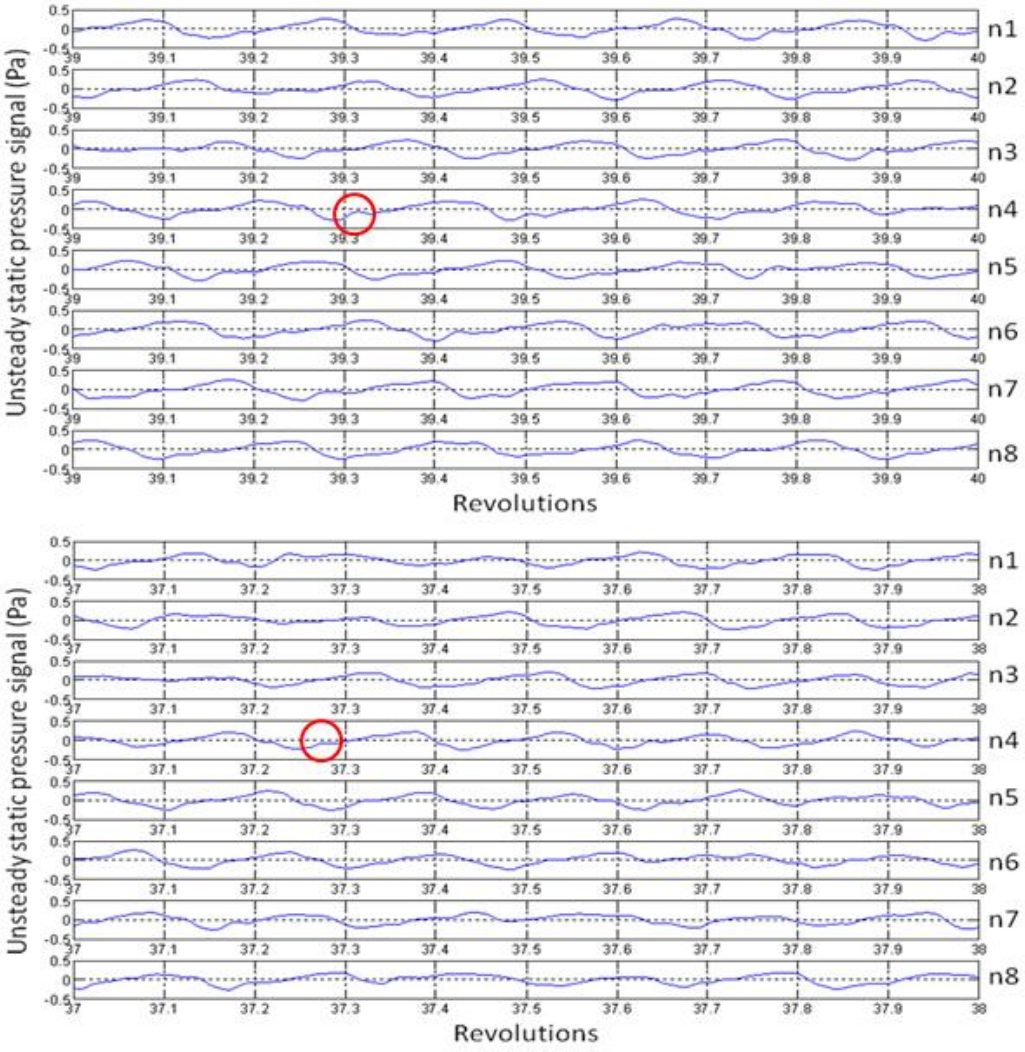

Figure 5.10: Unsteady static pressure time history comparison in one rotor revolution (Up: Damage Case 1, Down: Damage Case 2)

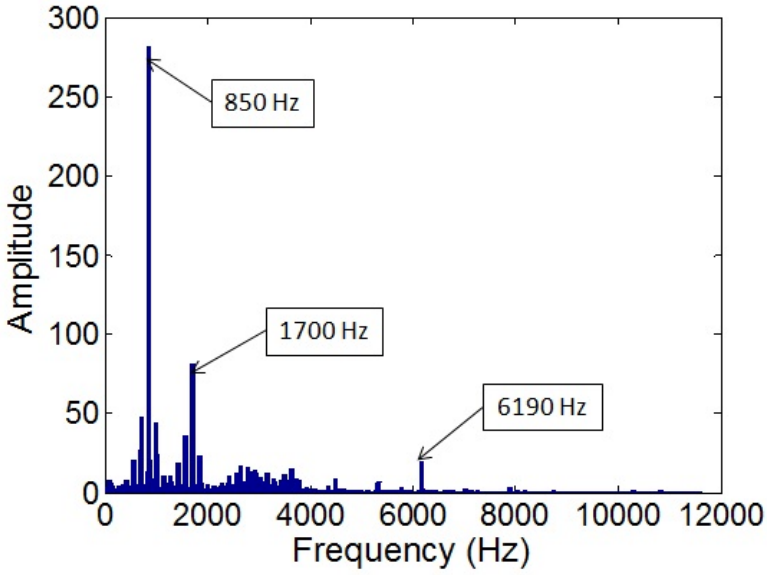

Figure 5.11: Fourier transform components of numerical sensor 8 on the casing for Damage Case 1

case. Figure 5.12 shows the Fourier transform from a numerical sensor on the casing for Damaged Case 2. It can be worked out that the propagation speed of rotating stall is the same as Damaged Case 1.

Figure 5.13 shows the instantaneous negative velocity near the tip of the rotor. For both cases with damage, rotating stall cells are observed respectively at the same time with similar size, shape and approximately equally spaced in between. Compared with the undamaged case, the difference is that a non-rotating stall cell which covered the neighbouring region around the damaged blade all the time after rotating stall starts. The non-rotating stall region was caused by the feature of the damaged blade which diverts the inflow all the time causing permanent separations in the neighbouring area. When the rotating cell was passing through the damaged blade, it merged with the non-rotating cell. After it passed by, the non-rotating cell would recover to its original shape and size. That could be seen from the animation and also the 3D flow streamlines which will be discussed later. The extent of stall cells in the radial direction can be seen in Figure 5.14. The figure shows the negative velocity on an axial cut planes of the rotor each of which is 40% chord length downstream from the leading edge on the rotor hub. For Damaged Case

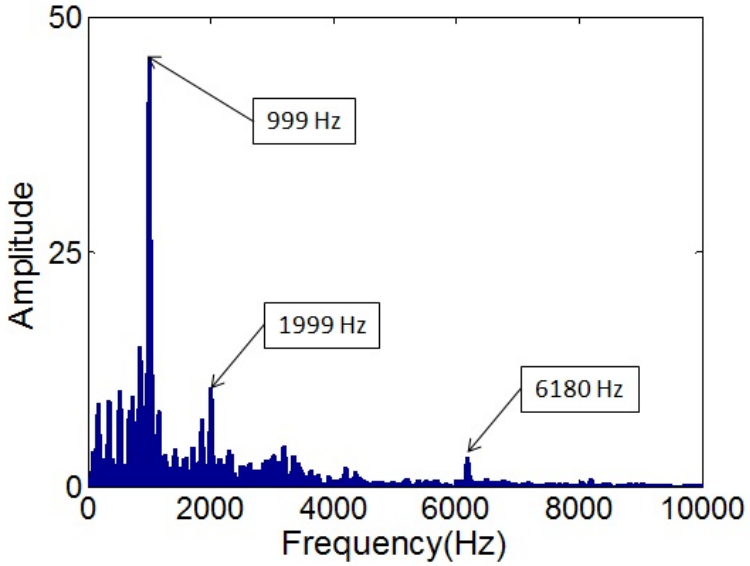

Figure 5.12: Fourier transform components of numerical sensor 8 on the casing for Damage Case 2

1, each stall cell covers approximately 17% of span in the radial direction which is the same as the undamaged case. The non-rotating stall cell is smaller in the radial extent which covered approximately 11% span. For Damaged Case 2, the rotating stall cells covered from approximately 10% to 18% in radial span and non-rotating cell covered approximately 12% of the span. In both cases, stall cells were observed near the tip region which is the results of interaction of high flow incidence in the tip region and tip leakage flow. Again, that is one characteristic for spike type rotating stall as discussed in Chapter 4.

For Damaged Case 1, the 3D structure of stall cells after a clear rotating stall pattern obtained was demonstrated in Figure 5.15. Figure 5.15 (a) shows the non-rotating stalled region including the damaged blade. In Figure 5.15 (b) which was obtained at a consequence time to Figure 5.15 (a), it shows one stall cell was merging with the non-rotating stall cell. The size of the stalled region was enlarged in both radial and blade-to-blade directions. The structures of other cells at other locations are very similar as in the undamaged case. For Damaged Case 2, the non-rotating stall cell is slightly larger with no significant difference. Thus, results of stall cell structures for this case are not presented. The formation of spike with damaged

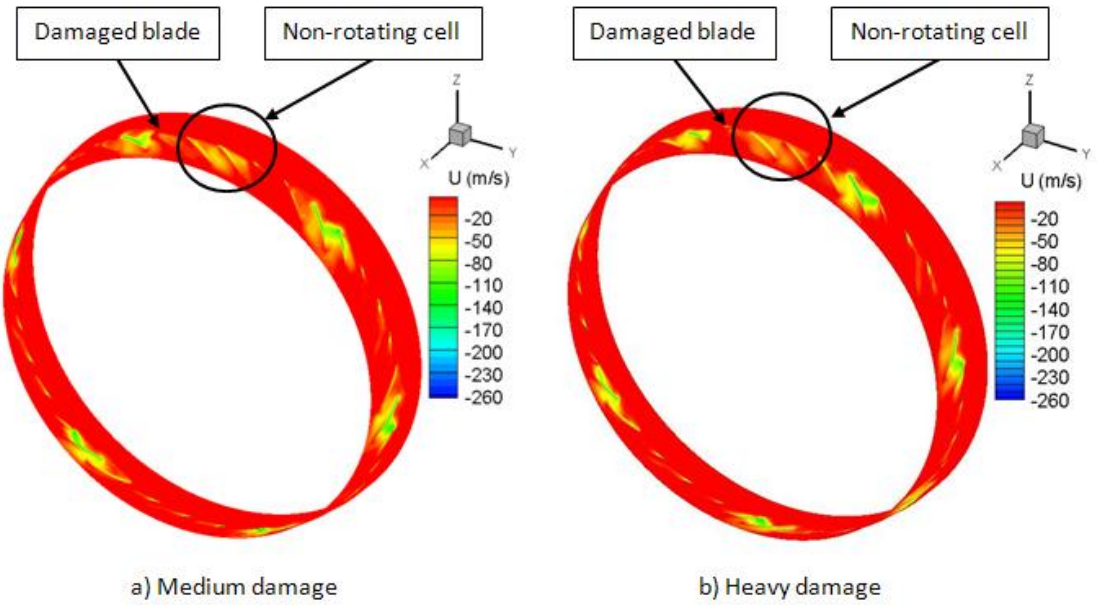

Figure 5.13: Instantaneous negative velocity near the tip of the rotor

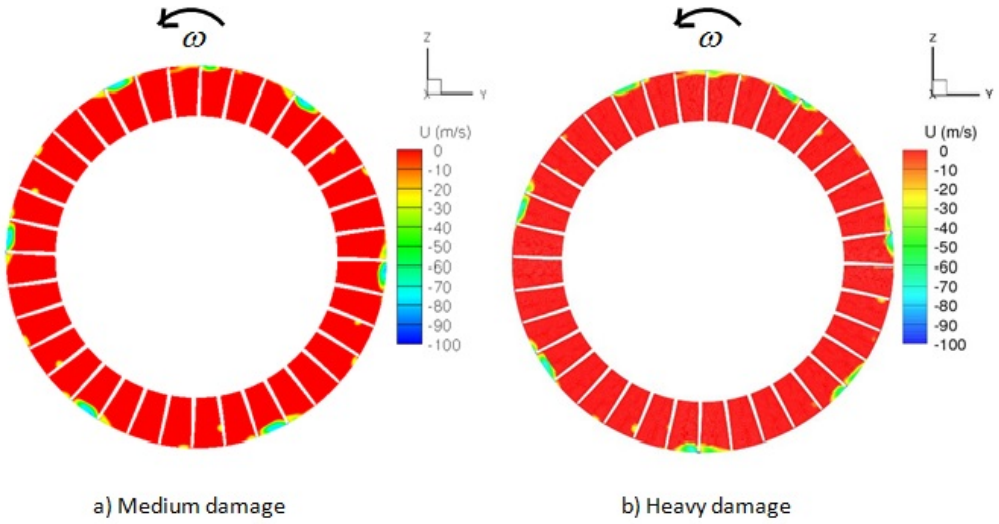

Figure 5.14: Instantaneous negative velocity comparison on an axial cut plane

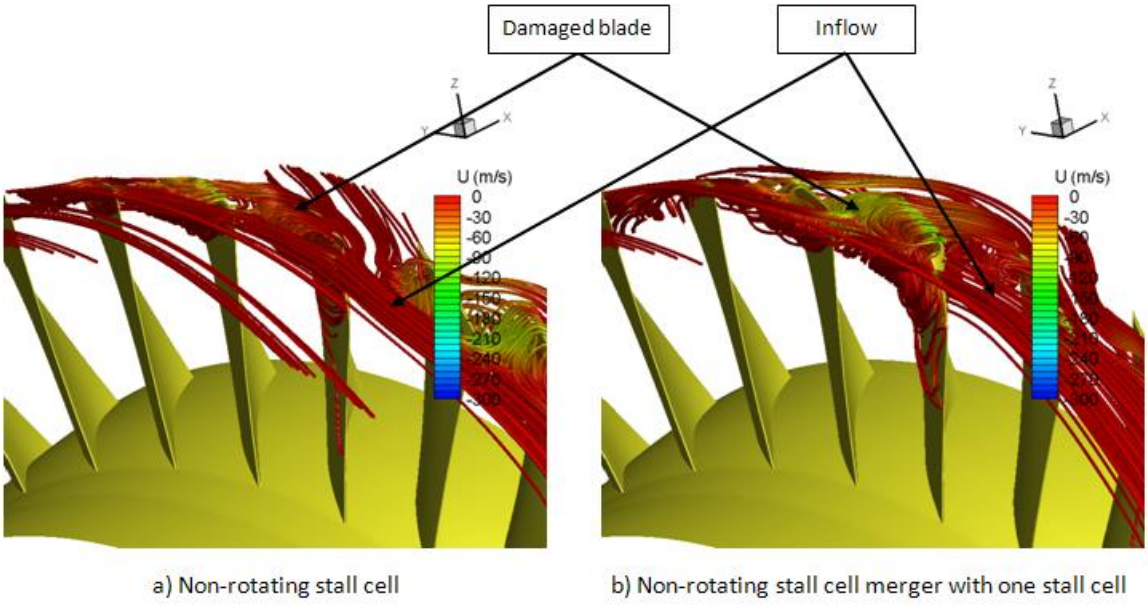

Figure 5.15: Stall cell structure for Damage Case 1

blade is caused by the combined effects of beyond critical incidence value near the tip, damage feature and the tip clearance flow. The formation of the radial vertex and its propagation mechanism is the same as to other literatures as discussed in Chapter 4.

It can be concluded that both Damaged Case 1 and Damaged Case 2 do not have significant effect on the overall compressor performance. The characteristic of rotating stall differs in the number of stall cells and the non-rotating stall cell. With one medium damaged blade, rotating stall predicted had the same number of stall cells with a non-rotating stall cell. By increasing the degree of the damaged blade, both the number of rotating stall cells and the size of the non-rotating stall cell were increased.

5.5 Effects of multiple damaged blades

To study the effects of multiple damaged blades in this compressor, a case with six damaged blades with medium degree of damage was investigated. This case will be labelled as Damaged Case 3 for clarity. The computational domain of the rotor annulus used is partly shown in Figure 5.16. Six damaged blades were placed next to

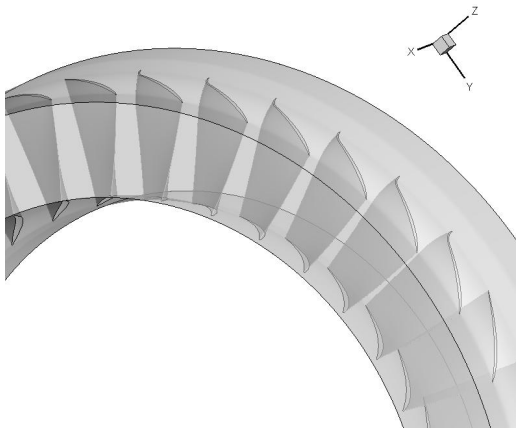

Figure 5.16: Part of the rotor assembly for Damage Case 3

each other in the rotor assembly for the reason that it would be expected to provide the most negative effect on compressor performance with this blade arrangement.

Figure 5.17 shows a comparison of the overall compressor performance with steady state simulation during the last 10 revolutions of the simulation. As seen in the figure, the unsteady mass flow is slightly lower and with larger variation. On the other hand the pressure ratio had a larger reduction which was approximately 1.2% due to the malfunctioned blades. Compared to Damaged Case 1 and 2, mass flow was reduced with larger variation and pressure ratio was decreased either. The time averaged mass flow and pressure ratio were slightly lower than both the other damaged cases. This case does not have a clear pattern of rotating stall based on the available data and it is believed that it will not have one since the case was simulated more than 90 revolutions with the mass flow still changing. It indicates that with six damaged blades, it is highly likely that the flow will not settle at all. Due to the limited time scale for this study, it is not possible to prove this at this stage.

The circumferentially averaged axial velocity profile comparison at the downstream of Rotor 37 is shown in Figure 5.18. Compared with the undamaged case, Damaged Case 3 had lower averaged axial velocity from 75% span to the casing as expected due to the existence of multiple damaged blades. As mentioned before, the damage on each damaged blade starts from 70% and had maximum damage

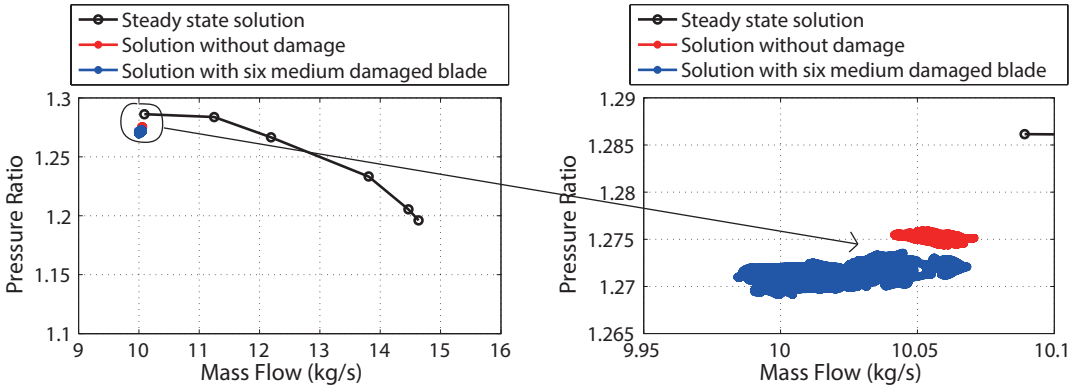

Figure 5.17: Compressor performance for Damage Case 3

near the rotor tip which result in that lower averaged axial velocity was achieved in that region. Mass flow seems to be compensated in the region between 75% span to the hub. The division for the region affected by damaged blades and mass flow compensation was moved to 75% span. Figure 5.19 shows the Mach number contour plot comparison at 75% span of Rotor 37. In Damaged Case 3, the passages with damaged blades were stalled and three other small stall cells were also found. However, the stationary stalled region has smaller radial extent which could be discussed later. That could be the reason why the circumferentially averaged axial velocity for both cases at this span are similar.

Figure 5.20 shows the unsteady static pressure signal time history from numerical sensors. In Figure 5.20 (b), the rotating stall pattern is very different from other cases. There is rotating stall cell passing the large non-rotating stall region which is circled in the plot. The circled part indicates six damaged blades with stalled flow were passing the numerical sensor. And it is not possible to work out the propagation speed or rotating stall based on the available data.

Figure 5.21 shows the instantaneous negative axial velocity near the tip and the contour plot is captured at a time after 91 revolutions. There is a very large non-rotating stalled region covering those damaged blades and some of the neighbouring area. In the meantime, there are three other cells of much smaller size rotating around the annulus. Another negative axial velocity contour plot is obtained on an

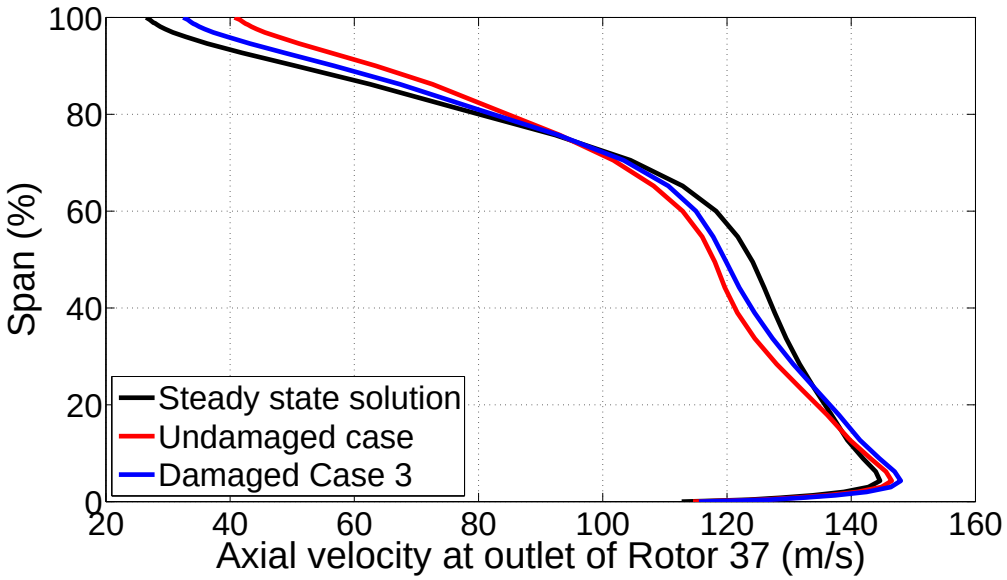

Figure 5.18: Circumferentially averaged axial velocity profile comparison at the downstream of Rotor 37

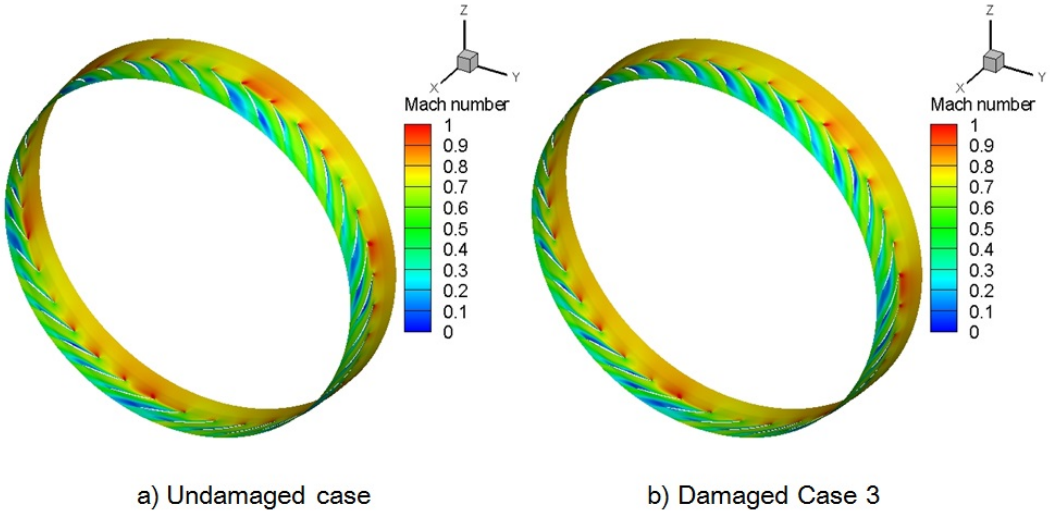

Figure 5.19: Mach number contour plot comparison at 75% span of Rotor 37

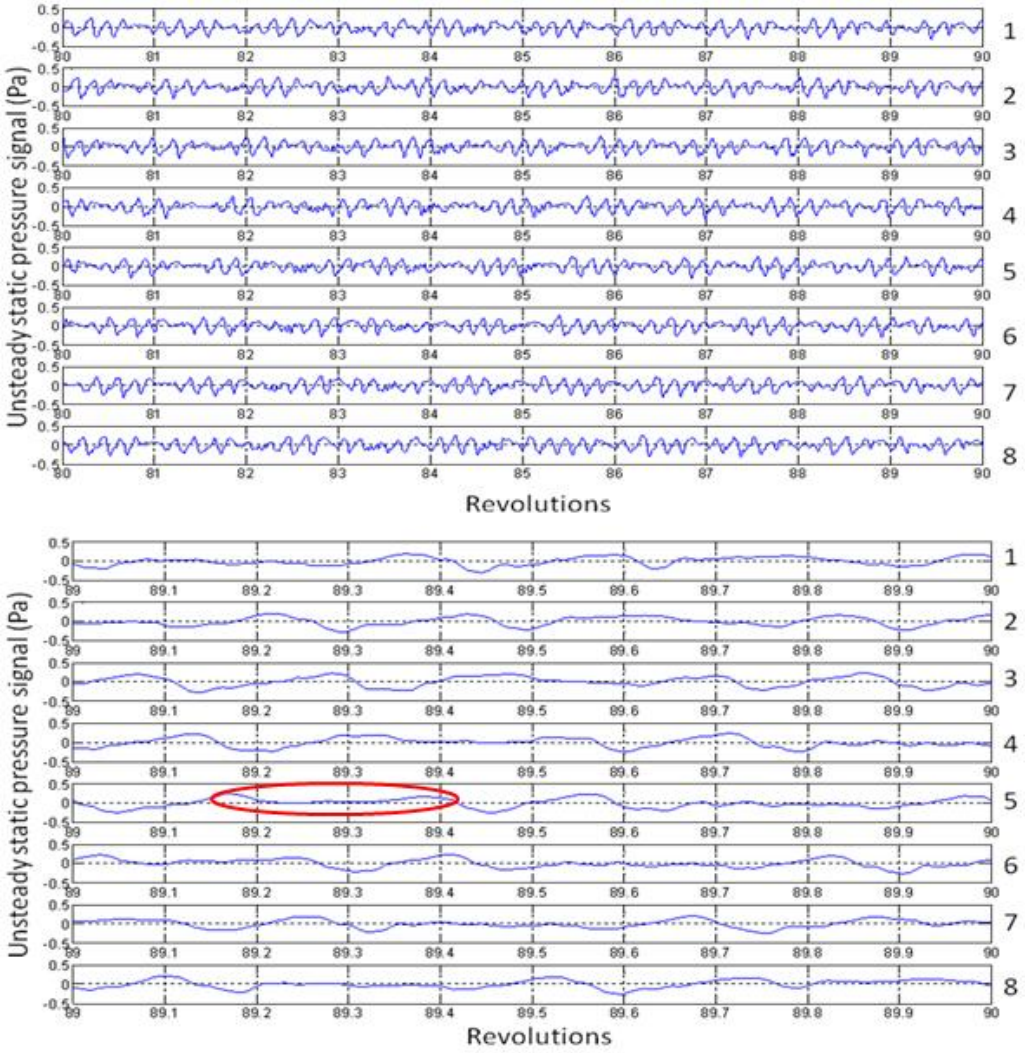

Figure 5.20: Unsteady static pressure signal time history from numerical sensors on the casing(Up: Time history in last 10 revolutions; down: Time history in 1 revolution)

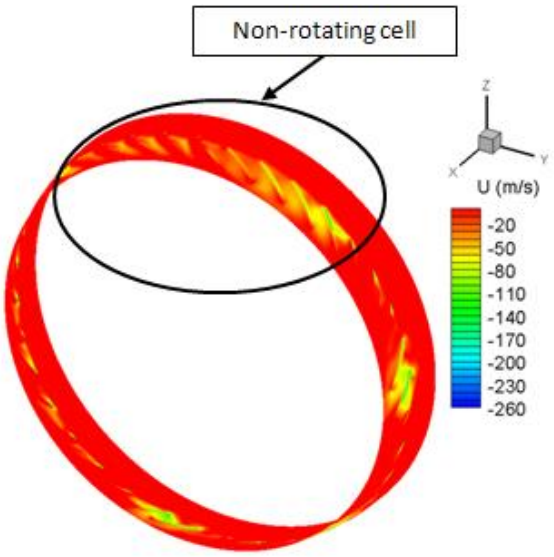

Figure 5.21: Instantaneous negative axial velocity near the tip of the rotor

axial cut at 40% of chord length downstream the leading edge of the rotor on the hub in Figure 5.22. As clearly shown form the plot, the large non-rotating stall region covers approximately 9 blade passages; three smaller cells cover approximately two passages each and up to 17% of the radial span.

To conclude, Damaged Case 3 does not have significant effect on the overall compressor performance based on the available data. On the other hand, mass flow was less affected since it was compensated in the unstalled passages. However, flow was very difficult to settle with six damaged blades. Pressure ratio were decreased due to rotating stall and the increased number of damaged blades compared with Damaged Case 1. Rotating stall characteristics are very different regarding to the number and size of rotating stall cells and the size of the non-rotating stall cell.

5.6 Summary

A compressor rotor assembly with three different blade damage settings were presented in this chapter and they were also compared with the undamaged case presented in Chapter 4. Spike type initiated rotating stall was predicted in all cases and the corresponding flow features were found to be similar to those reported in the

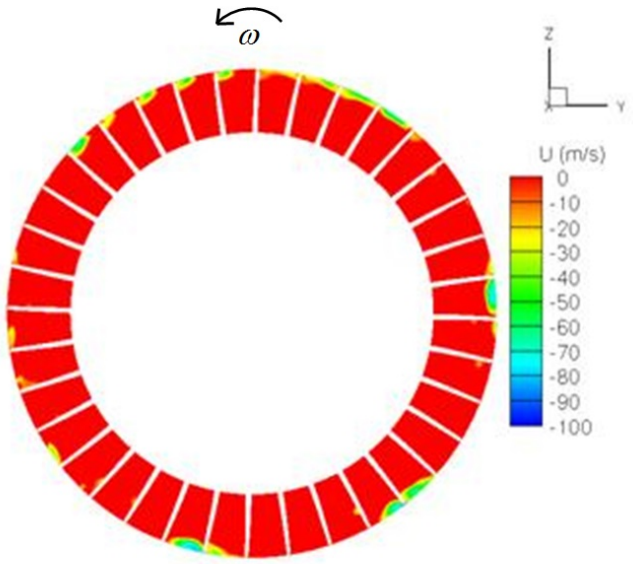

Figure 5.22: Instantaneous negative axial velocity on an axial cut plane through rotor blade

literature. For the assembly with one medium damaged blade and the nominal blade settings, two operating points on the compressor characteristics were investigated: one away from surge line and the other near surge line. When the compressor operating near work line, the flow separation was restricted to the surrounding passages of the damaged blade and flow was compensated in other passages.

At near stall condition, the assembly with one medium damaged blade has a similar stable and clear rotating stall pattern except one non-rotating stall region caused by the damaged blade. When increasing the degree of damage on the blade, spike type rotating stall was found as well however with a different pattern. Both the number of stall cells and the non-rotating stall region were increased. In the case with more damaged blades with identical medium damage, a large stationary stalled region was found which covered approximately quarter of the annulus and three other cells rotated around the annulus at irregular patterns. It was found that it was more difficult for the flow to settle to achieve a regular pattern when the degree of damage or number of damaged blades was increased, based on the available data. For all cases with rotating stall, mass flow was not significantly affected compared to the steady-state simulations because the flow deficit was compensated by increased

flow in the unstalled passages.

For one damaged blade with two different degrees of damage the stall cells rotated in the same direction of rotor rotation with a propagation speed approximately 83% of the shaft speed. Stall cells were approximately equally spaced and covered two rotor passages in the circumferential direction and approximately 17% of the passage in the span-wise direction. The flow features regarding the radial vortex and its propagation mechanism conforms to those reported in the literature for undamaged assemblies.

Contrary to expectation, tip curl damaged blades investigated did not have significant effects on compressor overall performance. Since the unsteady full annulus simulations require extensive computational resources, it was not possible to perform a detailed parametric study to find the degree of damage which would have detrimental aerodynamic effects on the compressor.

Chapter 6

VSVs mal-schedule effects on a 3.5 stage axial flow compressor

6.1 About this chapter

In this chapter, a 3.5 stage IDAC compressor is used to investigate the effects of VSVs mal-schedule on multi-stage compressor performance. All unsteady time-accurate simulations were performed near stall boundary at 68% of design speed. For comparison purposes, a case with nominal blade settings was also investigated. The corresponding compressor performance and flow behaviour were analysed and discussed in detail. Before the unsteady time-accurate simulations, steady state simulations were also performed and discussed to investigate rotating stall indicators.

6.2 Description of the compressor

A multi-stage compressor used in this study, Inversely Designed Aachen Compressor (IDAC), is a high-speed three stage axial compressor with Inlet Guide Vanes (IGV) and Controlled Diffusion Airfoils (CDA) for blade design. It was built at the Institute of Jet Propulsion and Turbomachinery of RWTH Aachen University (Bohne and Niehuis [2004]). The view of the compressor is shown in Figure 6.1. The outer diameter is 3,870 mm. The compressor has a design mass flow of 13.4 kg/s with a

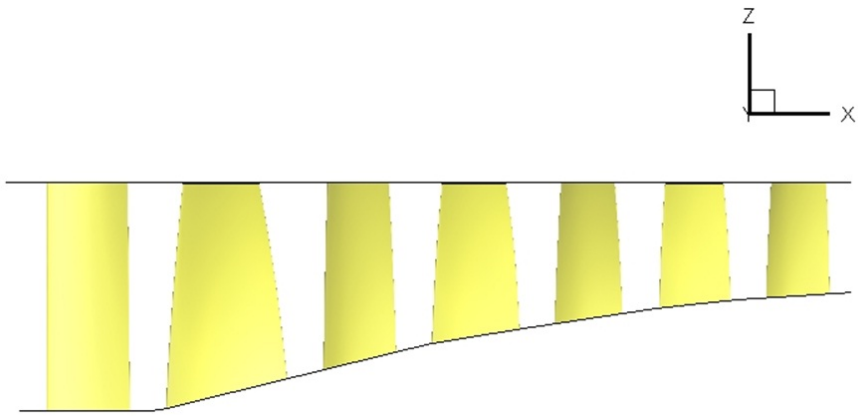

Figure 6.1: View of IDAC compressor

total pressure ratio of 2.03, operating at 17,000 rpm. At design condition, the total temperature rise is 68 K; the maximum relative inlet Mach number is 0.89 and the circumferential tip speed on the first rotor is 345 m/s. The design specifications are listed in Table 6.1. The IGV and the stator vanes are mounted in inner shroud rings with no radial tip clearances and the tip clearance for rotor blades is less than 0.3 mm during operation which is approximately 0.35%, 0.49% and 0.64% span for all three rotor bladerows respectively.

Flow in a multi-stage compressor is normally complex due to the three dimensional nature and the existence of stationary and rotating blades which may encounter the following unsteady phenomena: rotor-stator interaction, tip clearance flow, viscous flow effects, upstream and downstream influence (Niehuis et al. [2003]). The main reason for the choice of this compressor is that it only has three stages which is adequate for this investigation. It allows the researcher to consider the first two stator vanes as VSVs and it also makes the full annulus time-accurate unsteady simulation possible, though it could take considerable computing time for one simulation. Furthermore, the availability of its geometry and flow measurements for code validation also makes it desirable.

Table 6.1: Specifications of IDAC Compressor

Blade design	CDA
Corrected rotor speed	17,000 rpm
Corrected mass flow	13.4 kg/s
Power input	920 kW
Total pressure ratio	2.03
1st stage	1.30
2nd stage	1.30
3rd stage	1.22
Total temperature rise	68 K
Maximum relative inlet Mach number	0.89
Outer diameter	3,870 mm
Tip speed for rotor 1	345 m/s
Height of first blade	86.0 mm
Height of last vane	43.7 mm
Chord length of first blade	50.0 mm
Chord length of last vane	26.0 mm
Reynolds number first blade	960,000
Reynolds number last vane	380,000

6.3 Computational domain and boundary conditions

The computational domain and boundary conditions used will be presented in this section. The method used to initiate stall involved gradually throttling the operating point up to the stability limit using a downstream nozzle in a similar fashion to an experimental throttle, which is based on the same technique used in the blade damage study as explained in Chapter 4. Different performance points could be achieved by adjusting the downstream nozzle size and it is more practical to find the stability limit using steady state analyses within a limited time scale. Another objective of this research is to investigate whether there are indicators for potential stall by analysing the flow features from steady state simulations. The main part of the computational domain used for the steady state simulation is shown in Figure 6.1. The outlet boundary is extended 12 chord length of the first rotor downstream from the last stator where it is believed that flow with uniform static pressure can be

assumed without affecting the solution. Mixing planes were used at the interfaces between bladerows. Total temperature and pressure with zero flow angles were applied at the inlet boundary and uniform static pressure was applied to the outlet boundary.

For unsteady simulations, the computational domain used is shown in Figure 6.2 in a full annulus fashion. All unsteady simulations were performed at 68% speed. The main reason is that the compressor is highly likely to encounter rotating stall at off-design speed as reported in literatures. Another reason for that is the availability of detailed flow analyses at that shaft speed as reported in the literature. Sliding planes were used instead at the interfaces between bladerows. The unsteady flow computational domain contains approximately 25 million mesh points. The mesh for the first rotor is partially shown in Figure 6.3. Meshes in similar scale were used for the remain bladerows. For reference, 1,900 time steps were used for per engine revolution which required 85 hours in real time using 32, 2.5 GHz Intel Xeon cores. The starting solution for unsteady simulation was the near stall point from steady state solution which will be presented in the next section.

6.4 Study of rotating stall indicators

In this section, solutions from steady state simulations will be analysed. The compressor performance characteristics were obtained at three different rotational speeds: design speed, 84% speed and 68% speed which are shown in Figure 6.4. The two plots present the overall comparisons of pressure ratio and efficiency maps with experimental data and the solution at design speed was also compared with results from CFX simulations. The experimental data shown in the figure were obtained from the experimental work reported by Bohne and Niehuis [2004].

All CFD results were obtained from a mesh which provides a grid independent solution. As shown in the figure, the CFD solution from SURF is not well matched with the experimental data. The pressure rise for all three speeds has fairly good agreement with the experimental data. The general profile of the characteristics

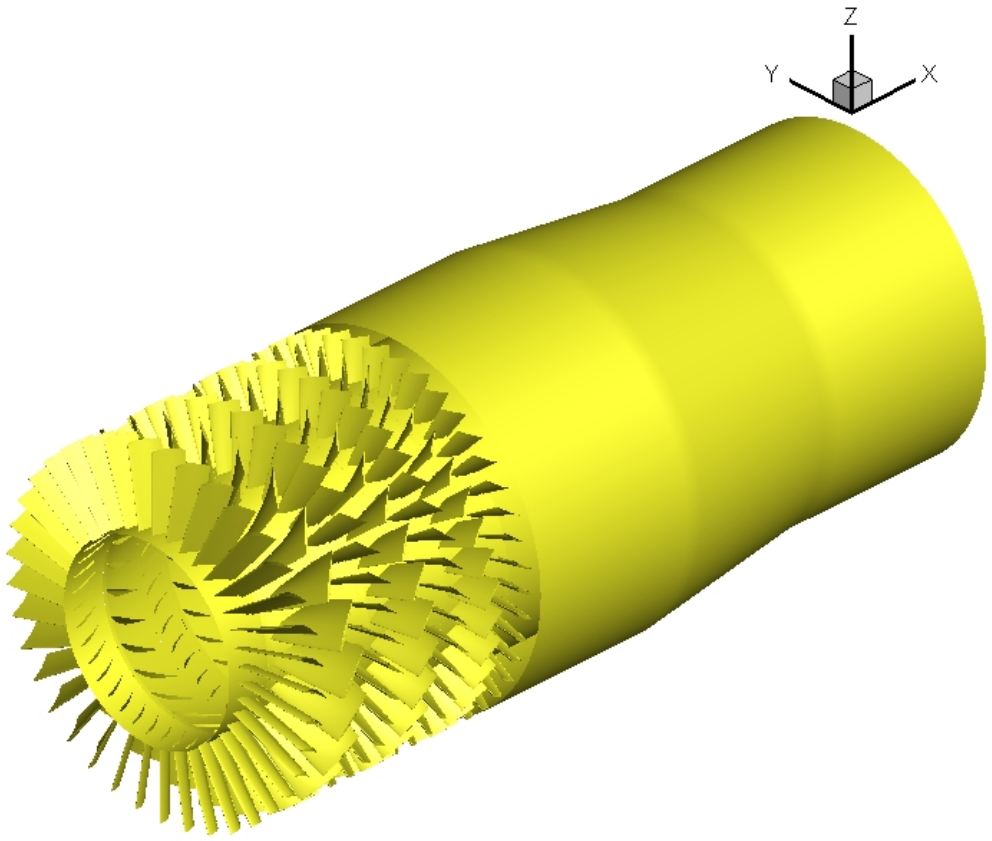

Figure 6.2: View of computational domain of IDAC compressor for unsteady simulations

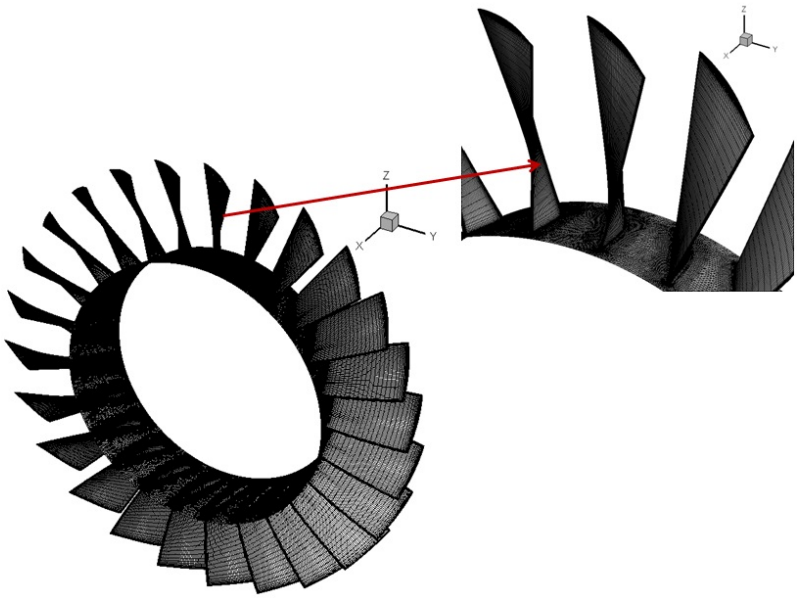

Figure 6.3: Mesh view for rotor 1

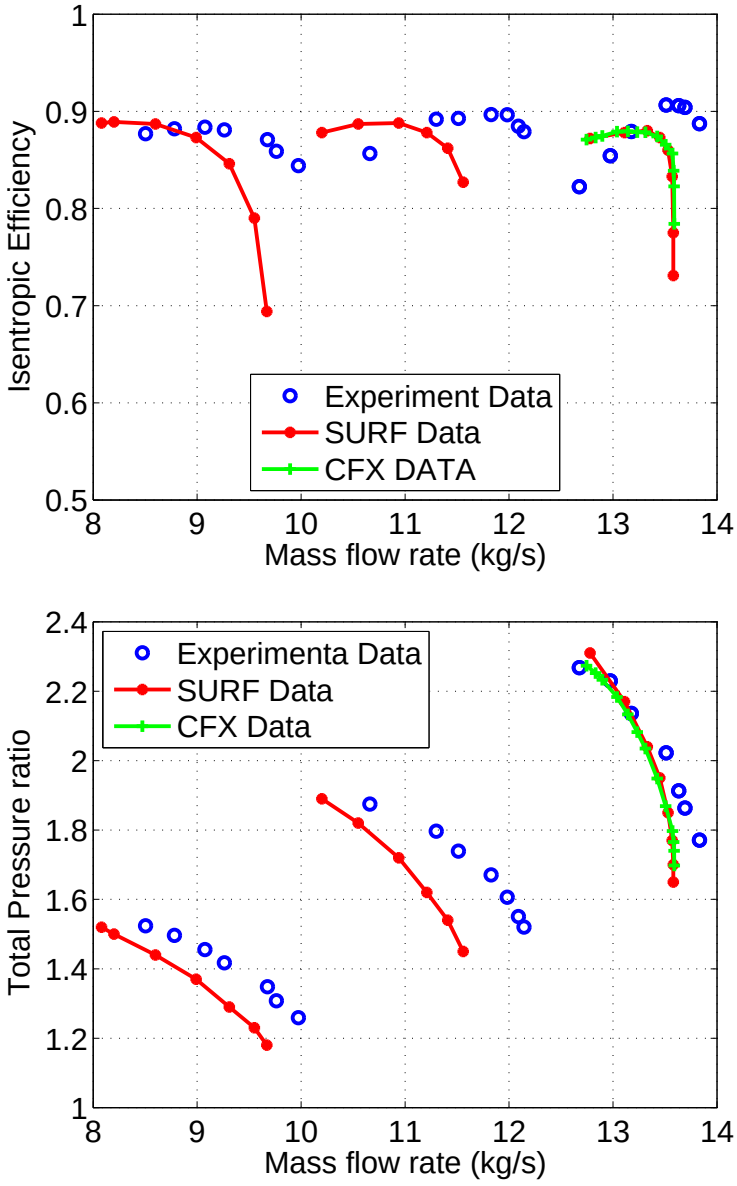

Figure 6.4: IDAC characteristics at three different speeds (Higher mass flow to lower mass flow: 100% speed, 84% speed and 68% speed)

and the operating flow range were well predicted. However, characteristics at three different speeds are all shifted slightly to lower mass flow compared with the experiment. The predicted choking mass flow was approximately 2% lower and mass flow near stall was approximately 1% higher than the experimental data. The reason could be that the boundary conditions used for the steady state simulation differ from the one in the experiment. In the experiment, through personal contact as reported by Nucara and Sayma [2012], inflow was transported from a bifurcated inlet duct with 90° bend to the axial inlet of IGV and with a honey comb at upstream to straighten the inflow. However, there were no measurements taken to reveal the effect of inlet flow distortion. Furthermore, measurements were only taken in one sector of the annulus due to its objective which was to investigate the unsteady flow behaviour. While uniform flow was assumed at the inlet and mixing planes were applied for the inter bladerow boundaries for the numerical simulations.

The in-house code was validated using NASA Rotor 37 by Li and Sayma [2012] and also had good agreement with experimental data reported by Sayma [2009]. This part of the research aims at using the performance from steady state simulation as a baseline and introduce VSVs mal-schedule for further investigations. Another steady state simulation at design speed was obtained by using a well known commercial code CFX which is indicated as the green line in Figure 6.4. The CFX simulation used the same geometry and boundary conditions as those for SURF. It can be seen that both pressure ratio and efficiency characteristics from SURF and CFX are well matched which represent the reassurance for the current predictions.

It is also worthwhile to understand the stage performance. Figure 6.5 shows the overall performance for all three stages at three different rotor speeds. Higher pressure ratios and efficiencies were obtained in stage 1 at all three speeds and pressure ratio decreased gradually across the downstream stages. For each stage, similar efficiency profile were achieved at different shaft speeds except stage 3 at design speed. The reason is that stage 3 was designed to be highly loaded and flow separation was observed in the third stator even at design conditions. At 68% speed,

Table 6.2: Vane settings for IDAC compressor

Vane settings	IGVs angle change	S1 angle change	S2 angle change
Nominal	0 °	0 °	0 °
Mal-scheduled	0 °	15 °	-15 °

the first stage was highly loaded with the rear stage unloaded as reported by Niehuis et al. [2003]. It also showed that stage 1 was operating at higher throttling line than the downstream stages which suggested that higher incidence would be encountered in that stage.

Compressor performance at near stall point

As mentioned before, one objective of this study is in attempt to find rotating stall indicators from steady state simulations. The first two stators were assumed to be VSVs. Different bladerows are labelled as: IGV, R1, S1, R2, S2, R3 and S3 respectively. Vane settings used are shown in Table 6.2. S1 was closed by 15° and S2 was opened by the same amount to create a stage mismatch. The blade profile comparison at mid span is shown in Figure 6.6. The change of stagger angle was the same along the blade span for each stator vane. The case with nominal blade settings is labelled as "Nominal case" and the case with VSVs mal-schedule is labelled as "MS case". Steady solutions at 68% speed with flow details at near stall points for both cases will be analysed and discussed next.

Figure 6.7 shows the overall compressor performance comparison at 68% speed between the Nominal case and the MS case. The MS case has lower pressure ratio and efficiency with narrower operating range. Compared with the Nominal case, mass flow at near stall point was reduced by 1% and pressure ratio was decreased by 6%. The chocking mass flow was reduced by approximately 3% with approximately 3% reduction in pressure ratio. It can be concluded that VSVs mal-schedule has significantly changed the overall performance of the compressor. Details regarding the mis-match between stages will be discussed next.

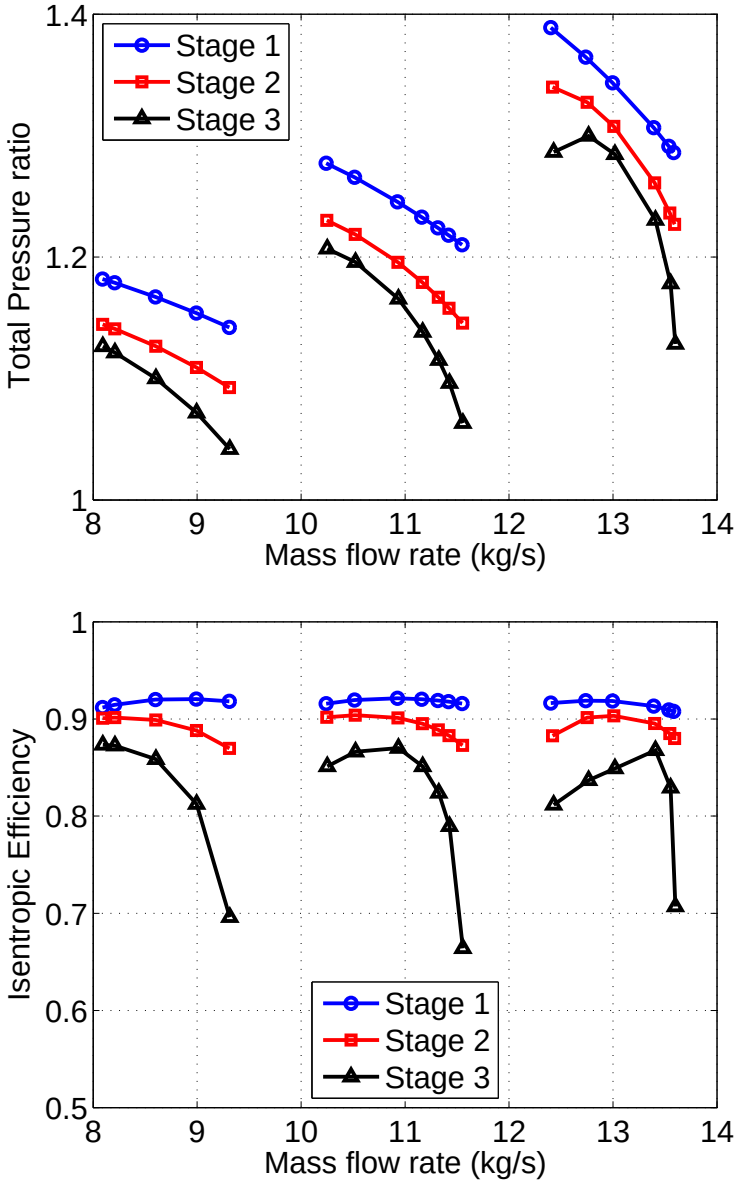

Figure 6.5: Stage performance characteristics at three different speeds (Low mass flow to high mass flow: 68% speed, 84% speed and 100% speed)

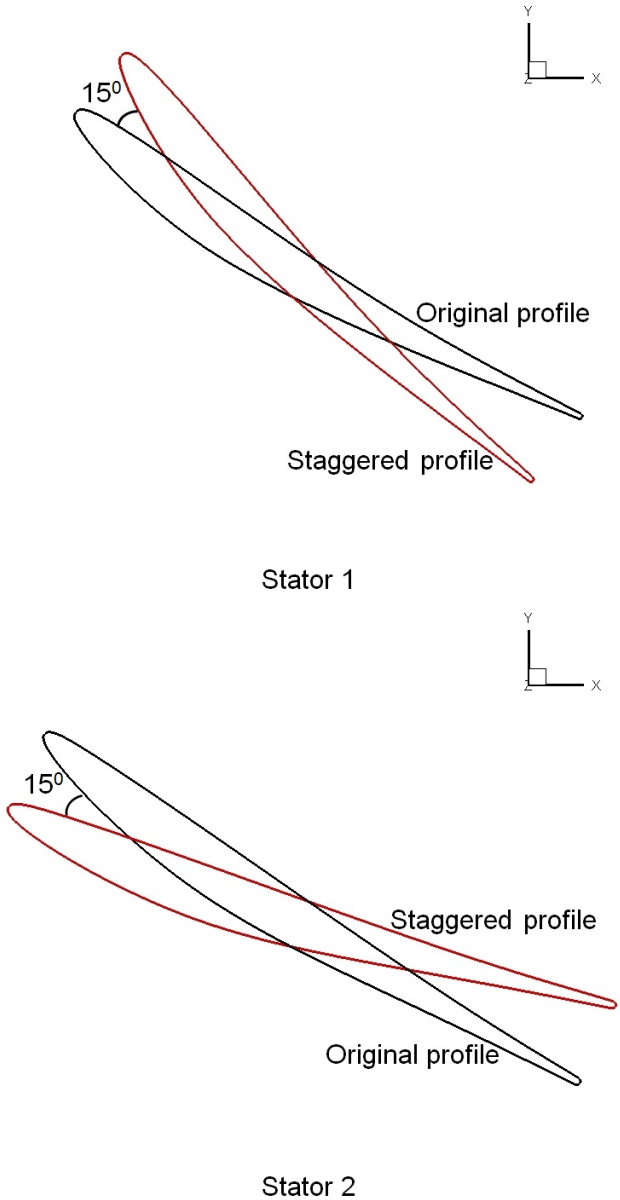

Figure 6.6: Blade profile comparison at mid span

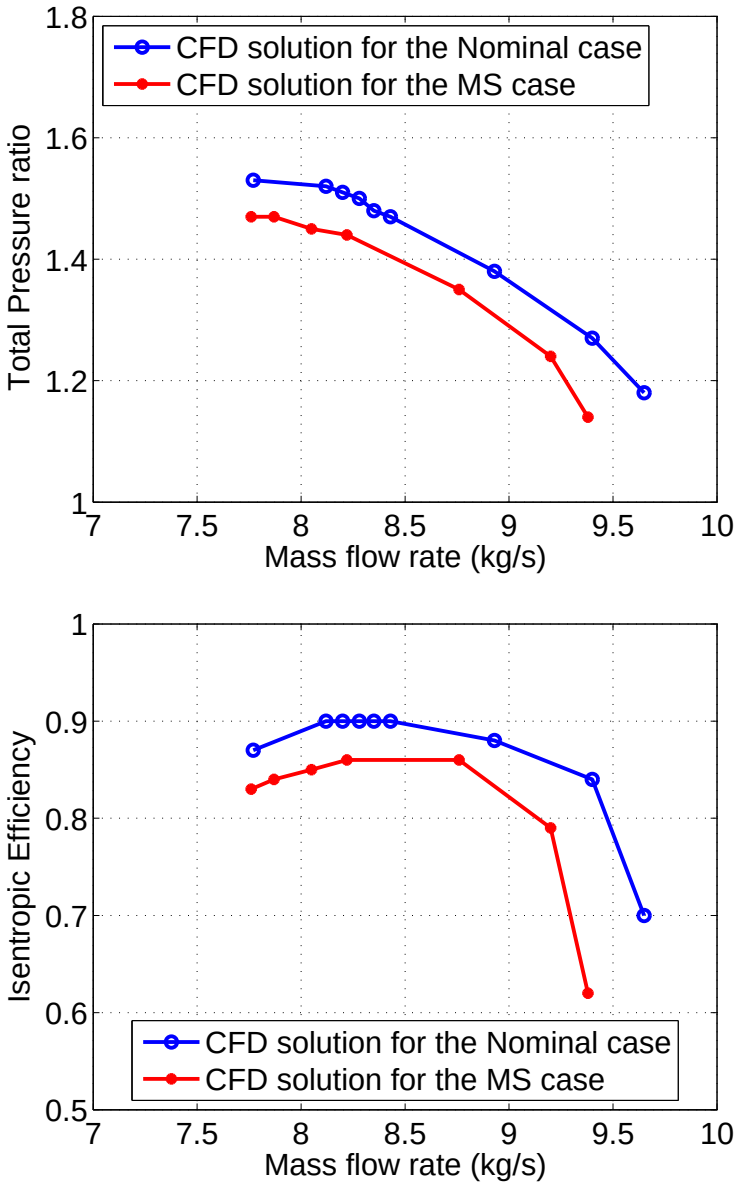

Figure 6.7: Overall compressor performance comparison at 68% speed

Figure 6.8 shows the Mach number contour comparison near the hub from all blades for both cases. For the Nominal case, flow separation can be seen in S1. For the MS case, it seemed that flow separation in S1 was eliminated resulting from the improved incidence while the flow separation in S2 was enlarged resulting from the degraded incidence. Figure 6.9 shows Mach number contour comparison at mid-span. Mach number in R2 and S2 seemed to be increased due to the combined effect of closure of S1 and opening of S2. Furthermore, flow separation was also predicted in S2 at mid span which also indicated the degradation in compressor performance by VSVs mal-schedule.

Figure 6.10 shows the Mach number contour comparison near the tip between the Nominal case and the MS case. It can be seen that there are low velocity flow regions indicated by green colour in all three rotors which are caused by tip leakage flow. In all three rotors, 'slip lines' were formed due to the existence of tip leakage flow which pushed the passage flow towards the pressure side of the the adjacent rotor blade. As discussed before, stage 1 was operating in a higher throttling line with higher pressure ratio and incidence. That also provided a high possibility that by throttling the compressor further for both cases, if possible, the incidence of R1 could be beyond the critical value first resulting in flow separations which may trigger stall.

Pressure profiles on the IGV and R1 seemed not to be affected by the MS which will not be shown here. Figures 6.11, 6.12, 6.13, 6.14 and 6.15 shows the pressure profile comparisons at mid span between the Nominal case and the MS case for S1, R2, S2, R3 and S3 respectively. Pressure profile comparisons at other spans showed the similar trend. As shown in the overall performance comparison in Figure 6.10 which was discussed before, both mass flow and pressure ratio was reduced due to the VSVs mal-schedule. With the same blade configuration in the same compressor, the incidence would normally be increased with the decreased mass flow resulting in higher pressure ratio. However, the stage mis-match in the MS case has altered the flow completely which was believed to be the cause for the difference in the pressure

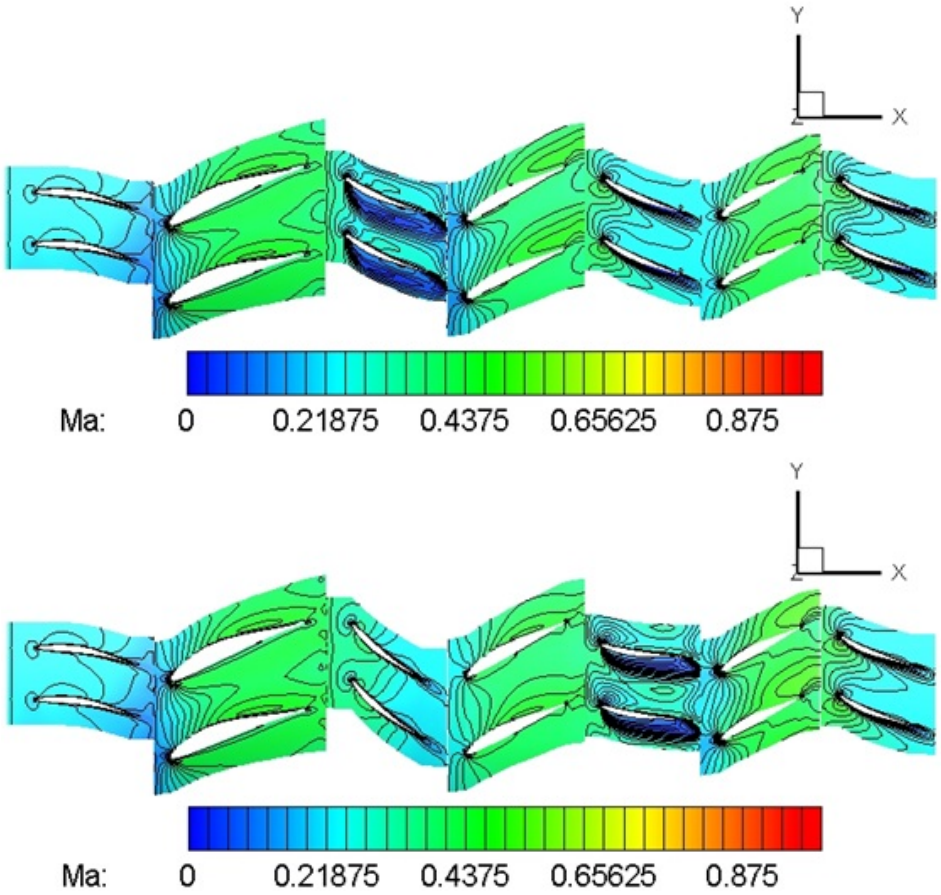

Figure 6.8: Mach number contour plot near the hub of the blades at near stall point at 68% speed (Upper: Nominal case; Lower: MS case)

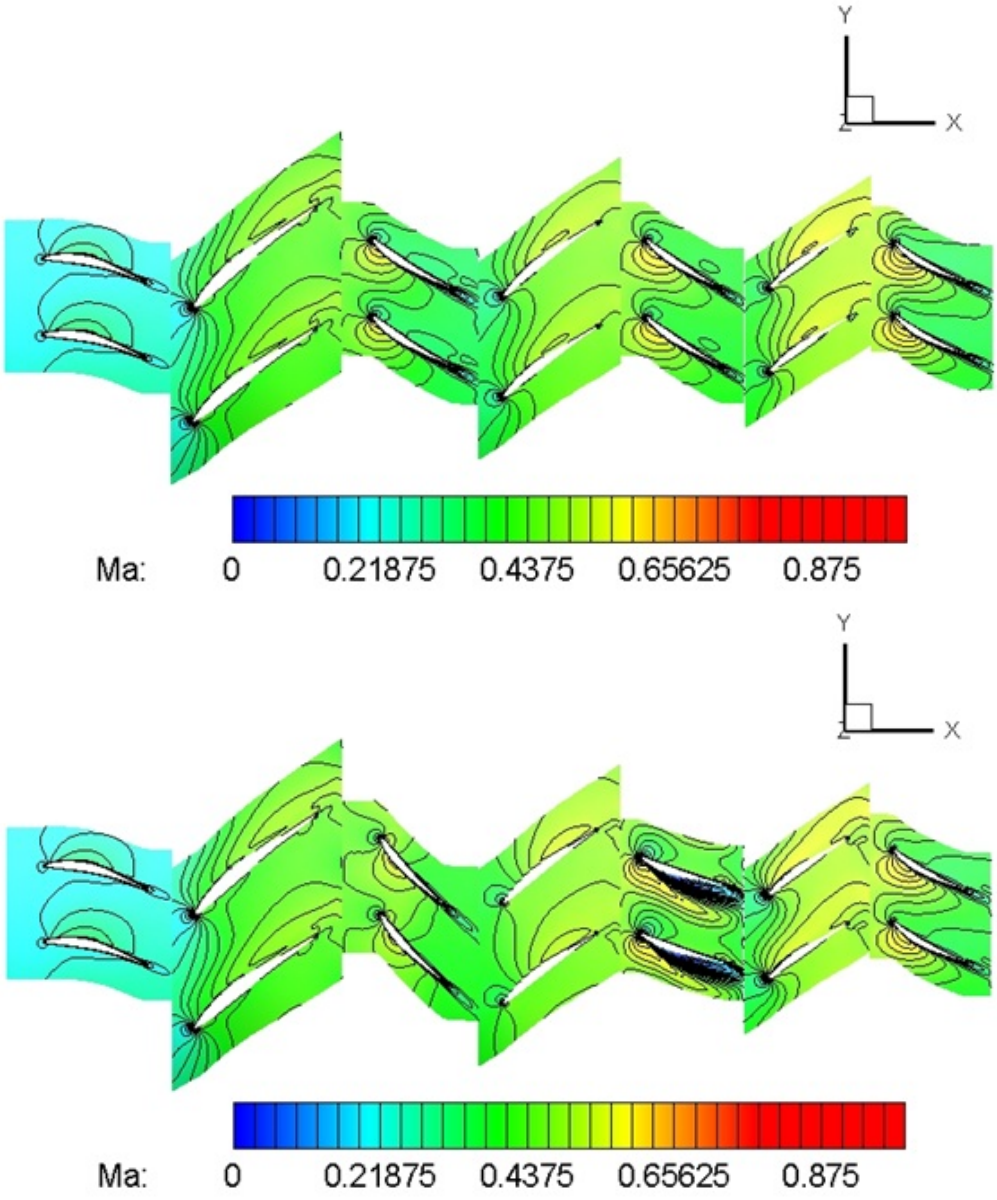

Figure 6.9: Mach number contour plot at the mid-span of the blades at near stall point at 68% speed (Upper: Nominal case; Lower: MS case)

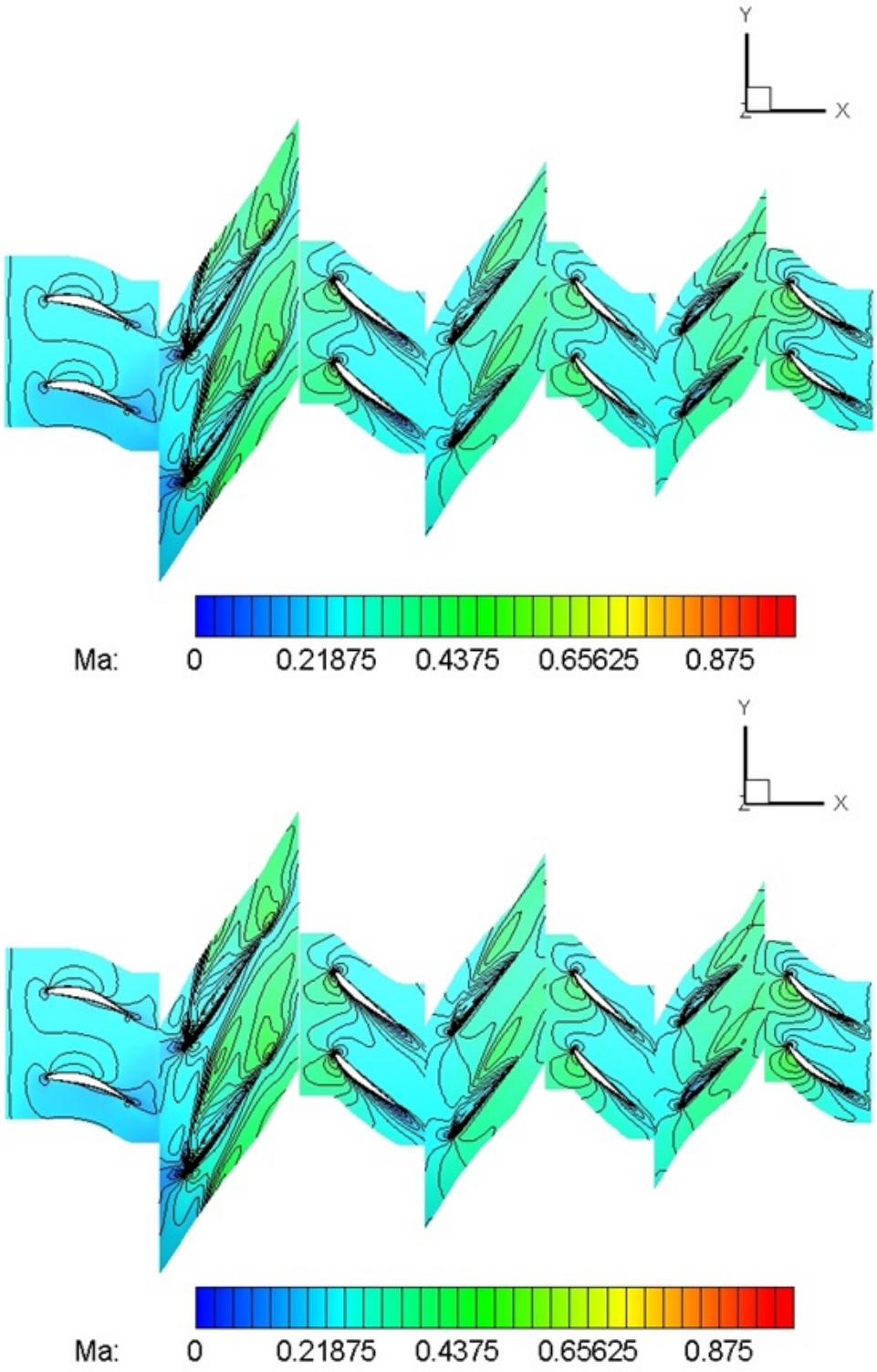

Figure 6.10: Mach number contour plot near the tip of the blades at near stall point at 68% speed (Upper: Nominal case;Lower:MS case)

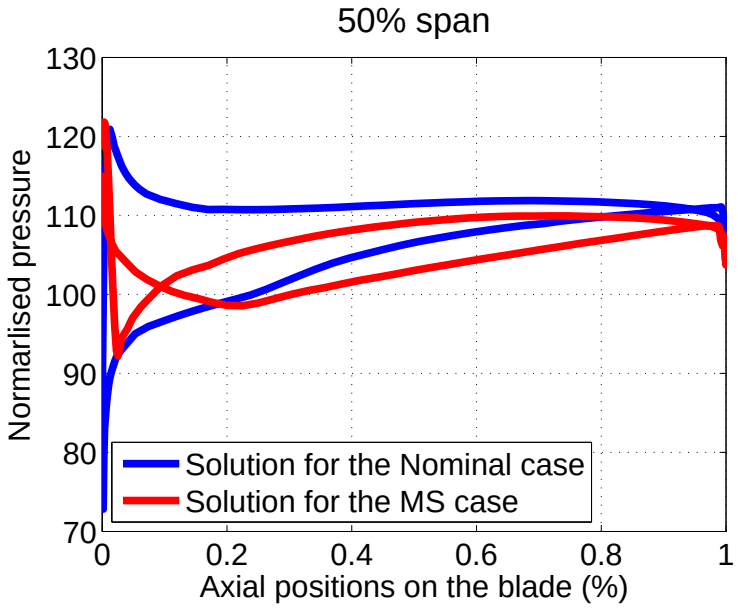

Figure 6.11: Pressure profile comparison on S1 at mid span

profiles.

Figure 6.16 shows the circumferentially averaged axial velocity radial profile comparison at the upstream of S1. From mid span to the tip region, the axial velocity was lower than the Nominal case, while the separation near the hub region seems to be cleared out for the MS case indicated by the increased axial velocity. Since flow was merely diffused in stators with decreased absolute velocity and reduced axial velocity by closing S1, the incidence was reduced. This was what happened between the casing and approximately 42% span. Due to the deign of this compressor, S1 had separation near the hub region. The improved incidence near the hub region removed the flow separation.

Figure 6.17 shows the axial velocity radial profile comparison upstream of S2. For the MS case, the axial velocity has increased across almost the whole passage which indicated the local increase in mass flow in S2 due to its opening. With the increased axial velocity combined with the opening of S2, the incidence was increased. Due to the original design, small flow separation region was found near the hub in the Nominal case from the Mach number contour. The degraded incidence near the hub enlarged the flow separation.

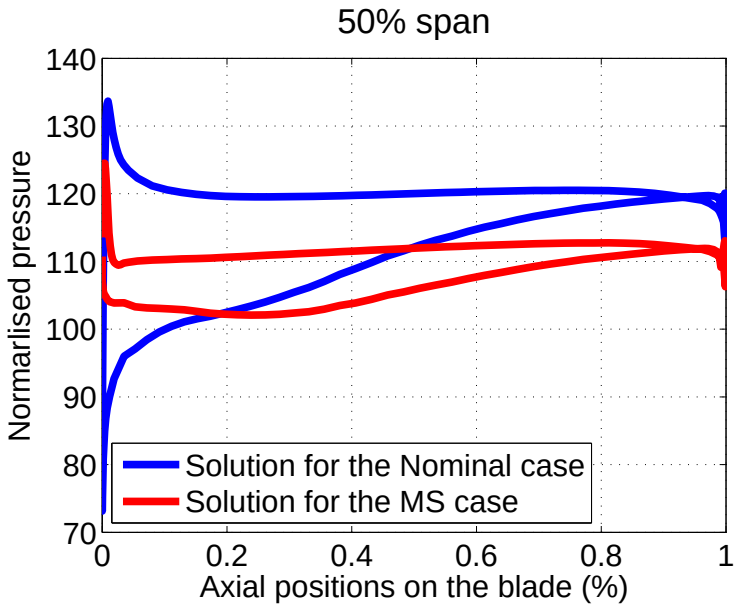

Figure 6.12: Pressure profile comparison on R2 at mid span

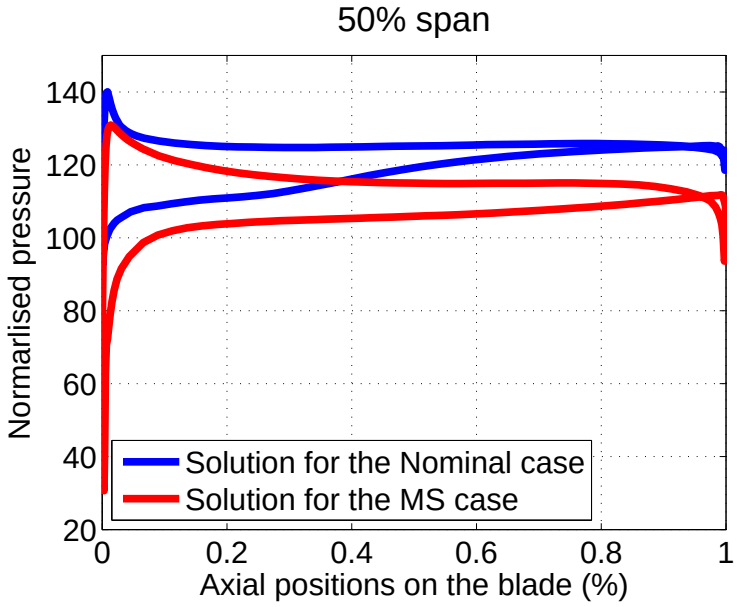

Figure 6.13: Pressure profile comparison on S2 at mid span

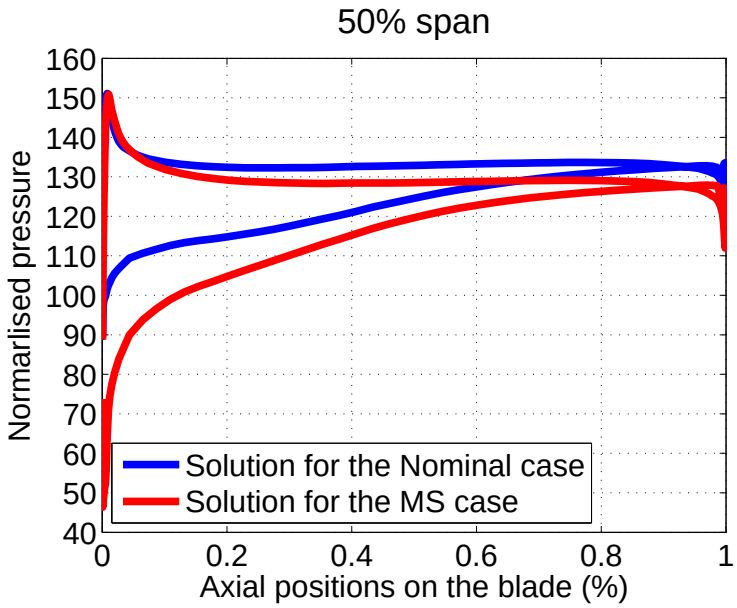

Figure 6.14: Pressure profile comparison on R3 at mid span

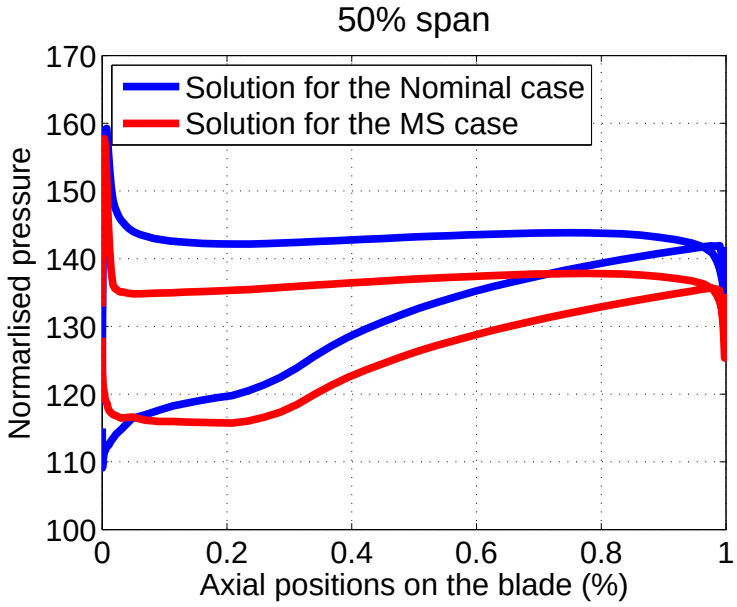

Figure 6.15: Pressure profile comparison on S3 at mid span

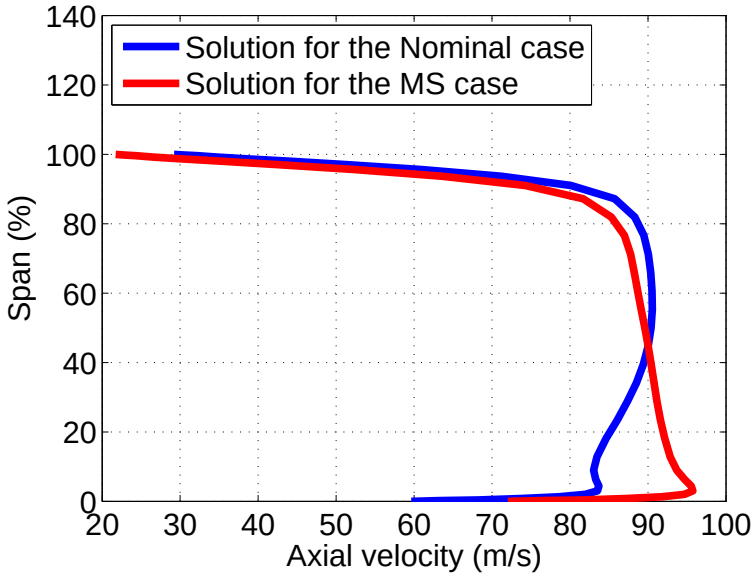

Figure 6.16: Axial velocity radial profile comparison upstream of S1

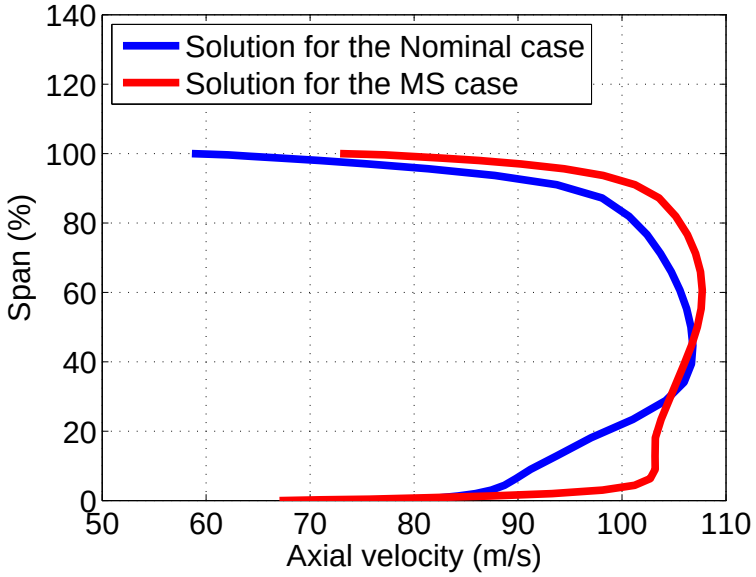

Figure 6.17: Axial velocity radial profile comparison upstream of S2

To sum up, the MS case has narrower flow range, lower pressure ratio and efficiency which indicates that VSVs mal-schedule has altered the overall performance completely. Pressure profile comparisons also showed that the performance was negatively affected. By analysing flow detail through Mach number contours across the compressor and the axial velocity radial profile comparisons, it was found that flow separation was improved by decreased incidence on S1 while the flow separation was enlarged by increased incidence on S2. The flow separation in S2 was also predicted at mid span. Nevertheless, mis-match was created between stages. It was assumed that R1 was possible to be stalled first than the other two rotors due to higher incidence at near stall point and the tip clearance flow effects. Niehuis et al. [2003] also reported that R1 was likely to stall first at 68% speed through experimental observation.

6.5 Unsteady investigation for the Nominal case near stall boundary

As discussed in Chapter 5, introducing small asymmetry of the same order of manufacturing tolerances into the computational geometry could lead to a much quicker onset of rotating stall in the numerical simulations and significant computer time savings. Therefore, all blades in the computational domain for this compressor were also randomly staggered between $-0.2°$ and $0.2°$ which is within the manufacture tolerances, to create the required asymmetry. In this section, the unsteady simulation performed at near stall boundary with "Nominal" VSVs settings will be discussed.

The unsteady simulation starts from a converged steady state solution near stall but with an arbitrarily chosen slightly more closed nozzle downstream. The overall performance from unsteady simulation together with steady state solutions are shown in Figure 6.18. As explained in Chapter 1, surge is a global phenomenon typically associated with cyclic large pressure and mass flow fluctuations. In ex-

treme conditions, reverse flow could be encountered in the engine. For this case, the compressor has lost approximately 75% of its mass flow at the worst performance condition with few cyclic loops including large range variation for mass flow. Therefore, it could be concluded that surge cycles were achieved.

In actual engines, surge cycle occurs due to the volume downstream the compressor including the combustion chamber. Within a very short time, flow is significantly built up in that volume resulting in increase of pressure ratio due to the increased back pressure. That also leads to large drop in mass flow. After the flow is released to the combustion chamber which result in reduction in back pressure, the mass flow is then increased throughout the compressor. At extreme conditions, the flow is released from the combustion chamber with flames and goes out from the inlet of the compressor. That is why flames can be seen from the inlet of an engine during deep surge. This forms the fluctuation of mass flow and pressure ratio which constitutes a surge cycle. It also indicates that surge is the phenomenon that the compressor lost the ability to keep the required pressure rise/ratio.

The mass flow time history is shown in Figure 6.19. Three identical cycles are shown in the figure after 5 rotor revolutions. The mass flow varied from 2 to 8 kg/s. It shows that one surge cycle requires approximately 2 revolutions which indicates that the frequency of the surge cycle is approximately half of the one for shaft rotation. Surge could generate successively axial forces on fan blades which could cause high cycle fatigue (HCF) and damage the blade eventually. The consequence of surge is commonly referred to blade axial deflections may cause rotors hitting stators. Surge cycle could also cause extra loading or unloading on rotor blades which can be periodic with time. In conditions especially for rotor with high solidity, if two adjacent blades during vibration bend towards each other, they may hit each other which could result in blade damage. That is why the aeroelasticity investigations are essential for those cases, however they are beyond the scope of this research.

To capture the unsteady flow characteristics, six sets of numerical sensors were located in the stationary frames which are in-between all bladerows. In the axial

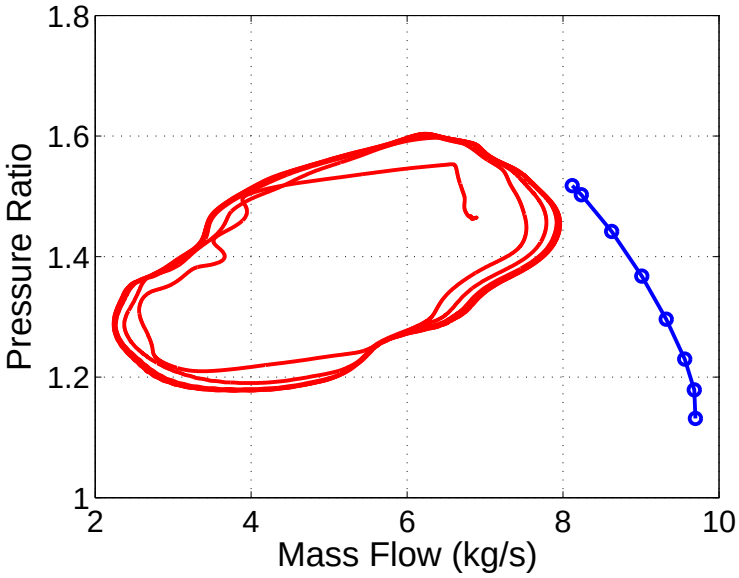

Figure 6.18: Overall compressor performance during surge with steady state solution

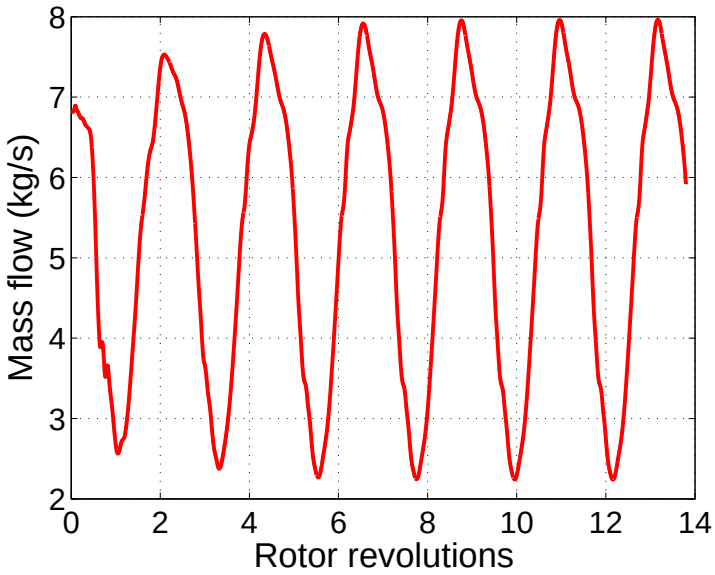

Figure 6.19: Mass flow time history for the Nominal case

direction, each set has equal distance from both bladerows. For each set of the numerical sensors with the same axial coordinates, they are similar to those used in the blade damage study which were descried in Chapter 5. They were placed 45° apart along 8 different circumferential positions. At the same circumferential position, there was one on the casing, one on the hub and four equally spaced in between.

As shown in the unsteady static pressure signal full time history from numerical sensors in Figure 6.20, pressure variations happened at the same time with no phase difference at different circumferential positions. It suggests that stall regions observed in the rotor bladerow were not rotating along the annulus. All pressure waves shown have six crests which indicate six surge cycles. Figure 6.21 shows the Fourier transform from one of the sensors at the upstream of R1. Three frequencies were found from the pressure signal: 108 Hz, 4820 Hz and 9530 Hz. The first one is the frequency for the surge cycle. The second one is the blade passing frequency (BPF) of R1 and the third one is its second harmonic.

Figure 6.22 shows the unsteady static pressure signal time history from six numerical sensors at different axial locations. They are located at: downstream of IGV, upstream and downstream of S1, S2 and upstream of S3 as labelled in the figure. As indicated by the dashed line, pressure variation started firstly from the S3 which suggested that S3 was responsible for the initiation of the surge cycle at this shaft speed. It agrees with the general principle for surge as explained earlier that surge commonly starts at the end of the compressor. It was also reported in Niehuis et al. [2003] and Bohne and Niehuis [2004] that S3 defined the surge limit of this compressor at the design speed.

The further detailed flow in S3 will be analysed which may confirm the cause for surge cycles. Figure 6.23 shows the instantaneous circumferentially averaged axial velocity radial profile at three different times in one surge cycle upstream S3. After 9.6 revolutions, the mass flow was in the range of 5-6 kg/s from the full time history. Low velocity regions were found near the tip and hub indicating flow blockage.

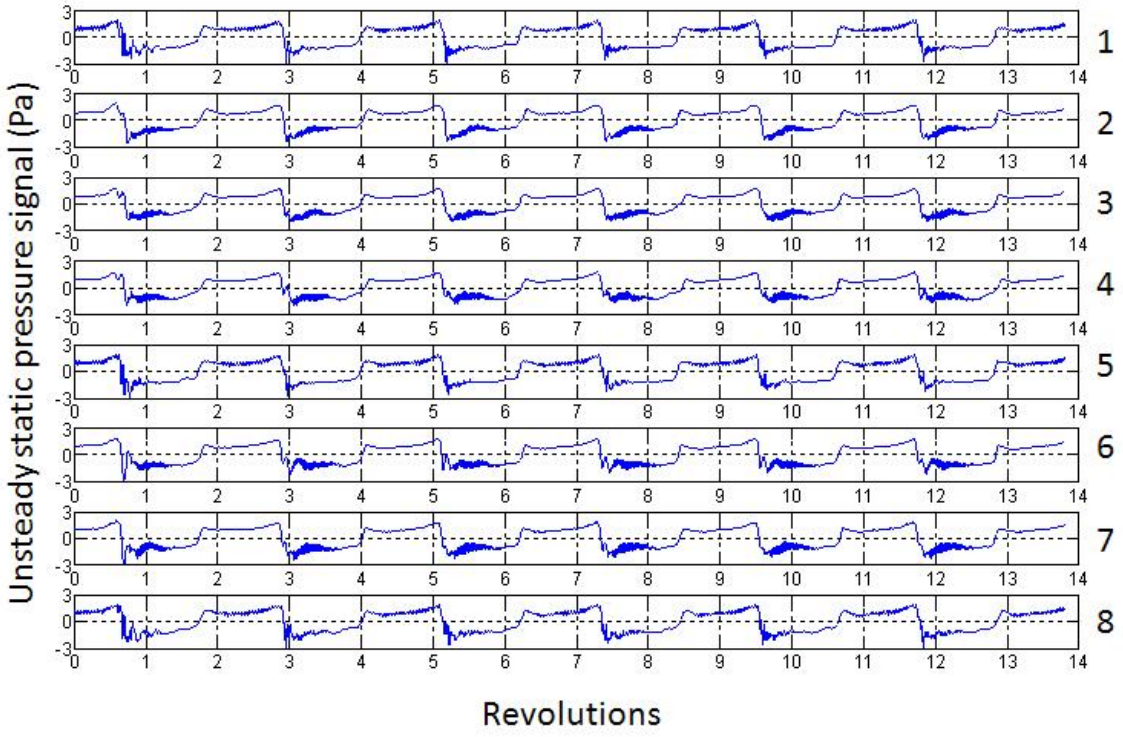

Figure 6.20: Unsteady static pressure signal time history from eight numerical sensors on the casing upstream R1 for Nominal case

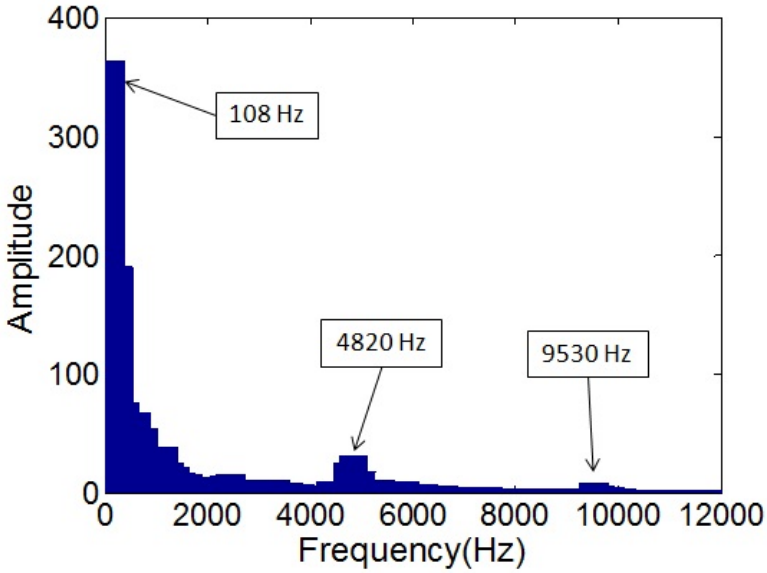

Figure 6.21: Fourier transform components from one sensor upstream R1

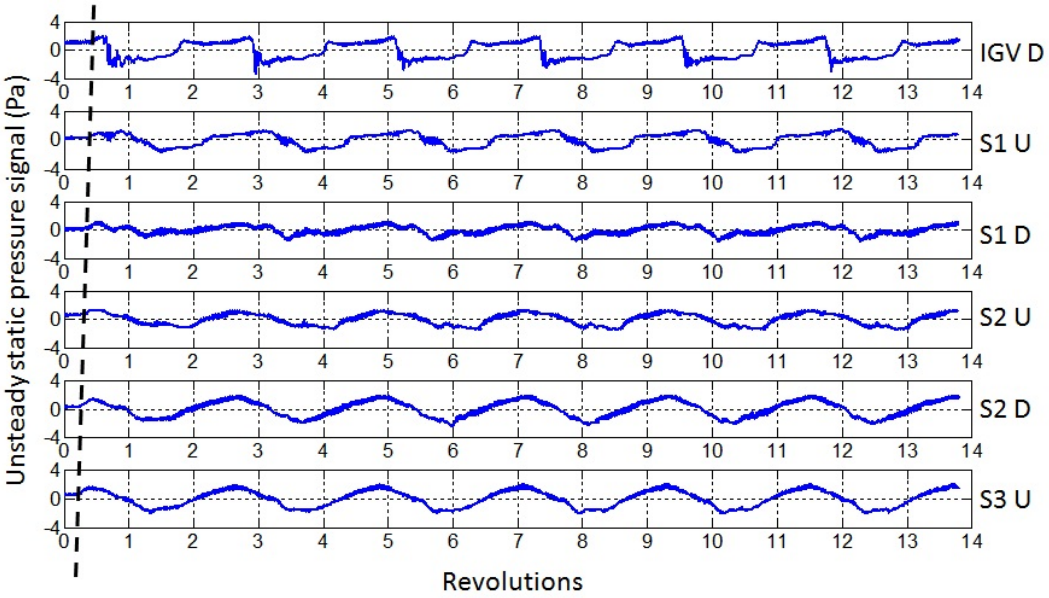

Figure 6.22: Unsteady static pressure signal time history from six numerical sensors on the casing in different axial locations for Nominal case(D: downstream; U: upstream)

When mass flow reduced to be close to the lowest value after 10.1 revolutions, no negative flow was found in S3, however the axial velocity profile varies significantly from tip to hub. Flow was stalled in the lower radial part of the passage which was indicated by the low velocity. This phenomenon was the result of the design of this stator. As reported by Bohne and Niehuis [2004], a hub-corner-stall was observed in S3 even at design condition because the stator was originally designed to be highly loaded. Even though no stall was found in S3 at near stall condition at 68% as well as the experiment, due to lower flow velocity resulting in improved incidence in the present study which was shown in the Mach number contours discussed earlier. It was claimed by the authors that it was caused by the interaction between the profile flow and the sidewall boundary layer which was not taken into account in the design process. When the mass flow reached to its peak value in the cycle after 11 revolutions, stalled region was cleared out with improved axial velocity and incidence on the blade.

To conclude, surge cycles were predicted for the Nominal case with a frequency of 108 Hz and it was also found that S3 was the cause for its initiation at 68% speed.

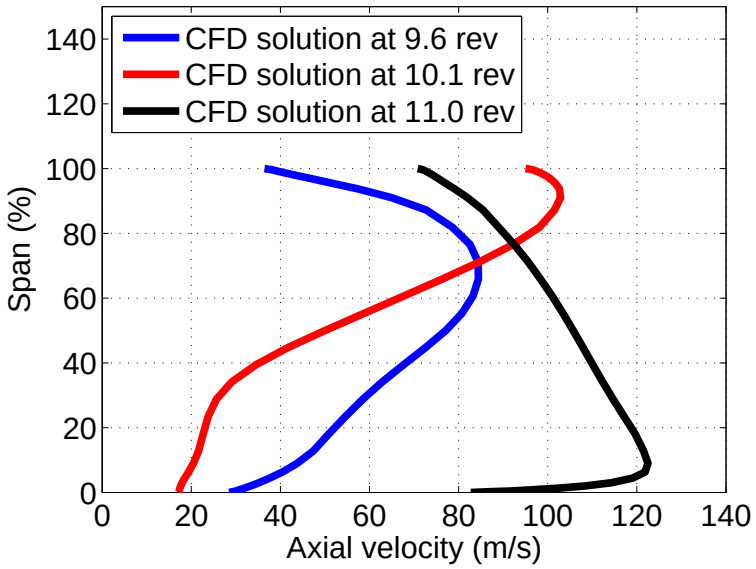

Figure 6.23: Instantaneous circumferentially averaged axial velocity radial profile upstream of S3

Stalled flow started from the hub region of S3 due to its original design the same as reported in the literature.

6.6 Investigation with VSVs mal-schedule

As explained in Chapter 1, VSVs are commonly used to control the performance in multi-stage compressors at off-design speeds. VSVs are normally controlled by actuator systems which could encounter malfunction occasionally. In this case, the original design of IDAC compressor does not have VSVs. To study the mal-schedule effects of VSVs, S1 and S2 were assumed to be VSVs as discussed at the beginning of this chapter. They were mal-scheduled and flow mis-match between stages were created especially at near stall boundary. In this section, the time-accurate unsteady simulations for the MS case will be discussed.

The unsteady simulation for this case was also performed at 68% speed with the same downstream nozzle size as in the Nominal case. The overall performance is shown in Figure 6.24 together with steady state solution. Part span rotating stall was predicted in this case. The mass flow with pressure rise characteristic had a

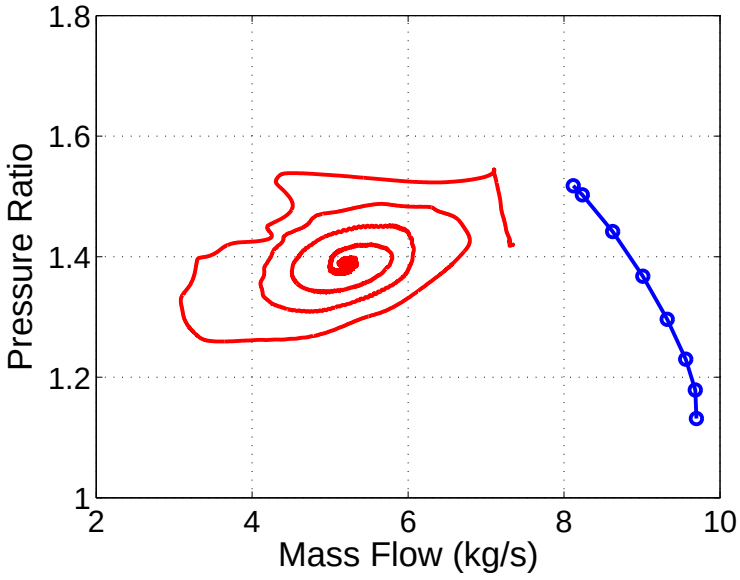

Figure 6.24: Overall compressor perfomance during rotating stall with steady state solution

shape of an inside spin. It tended to settle to one point with very small mass flow and pressure ratio variations. The mass flow time history is shown in Figure 6.25 from which it could also be seen that the mass flow settled down to a certain range after approximately 10 revolutions.

Rotating stall predicted in this compressor was also spike-type initiated. An instantaneous negative axial velocity contour plot at 95% span of the whole compressor after 30 revolutions is shown in Figure 6.26. By that time, a fully developed rotating stall pattern was observed. All the stall cells located at the same circumferential positions in all three rotors. As seen from the figure, stall cells covered seven, four and seven rotor passages in R1, R2 and R3 respectively. All stall cells located at leading edge regions and before the trailing edge regions and extended to the upstream stators. This is similar to the findings reported by Pullan et al. [2012]. Compared with their work, for this compressor, R1 has a even higher hub-to-tip ratio. The spike in this compressor could be caused by the flow separation at the leading edge of the blade resulting from "beyond critical" flow incidence which has the structure of a radial vortex outside the blade. The formation and propagation of the mechanism of spike was similar to that discussed in Chapter 4.

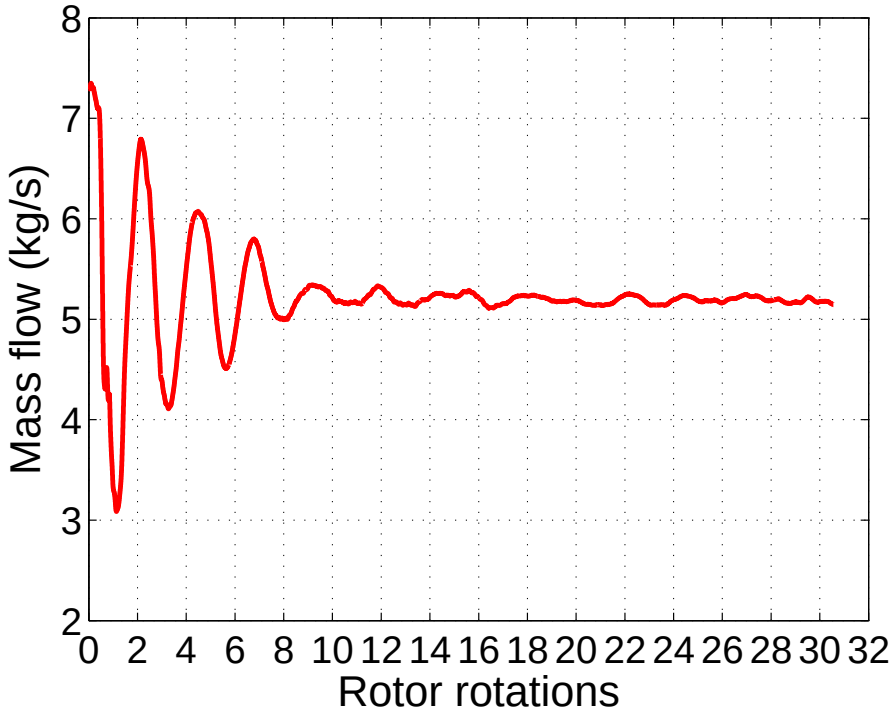

Figure 6.25: Mass flow time history for VSVs mal-schedule case

6.6.1 Flow in IGV and stage 1

As shown in the unsteady static pressure signal full time history in Figure 6.27, after the initial transition, rotating stall started at approximately 2 revolutions in R1. Then a pattern with 6 rotating stall cells were formed and they tended to merge to one large stall cell afterwards, seen from animations. From the 10th revolution, a pattern with one large stalled cell near the tip was firstly formed. It was believed to be caused by the interaction of the inflow and tip clearance flow. As shown in the unsteady static pressure time history, there is one pressure wavelength in two rotor rotations which provides the propagation speed of the rotating stall observed, approximately 50% of shaft speed. The propagation speed of rotating stall could also be worked out from the Fourier Transform from one of the numerical sensor which is shown in Figure 6.28. There are two main frequencies in the domain: 94.6 Hz and 7,230 Hz. The first frequency is the frequency of the rotating stall and the second frequency is the S1 blade passing.

Figure 6.29 shows the instantaneous axial velocity on an axial cut plane in the

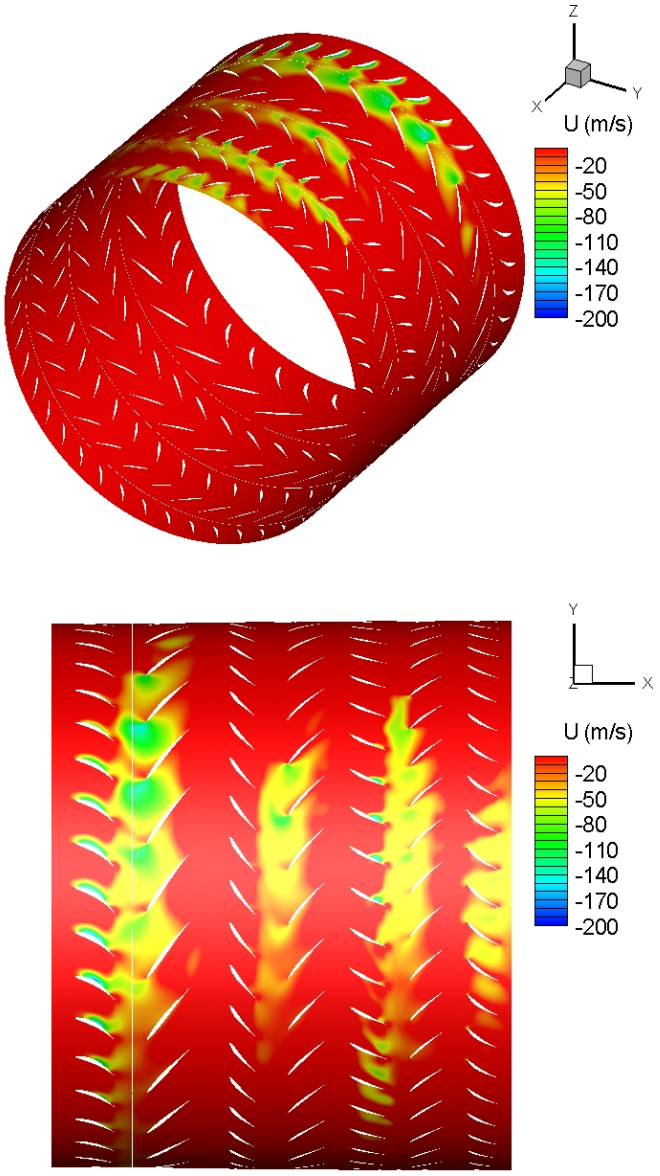

Figure 6.26: Instantaneous negative axial velocity contour plot at 95% of blade span after 30 revolutions

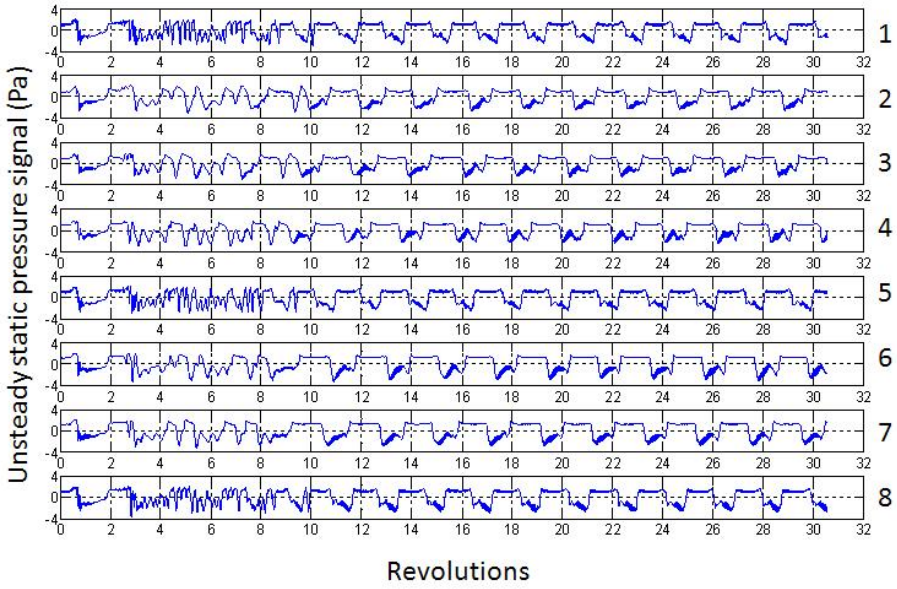

Figure 6.27: Unsteady static pressure signal time history from numerical sensors at the inlet of R1 for the MS case

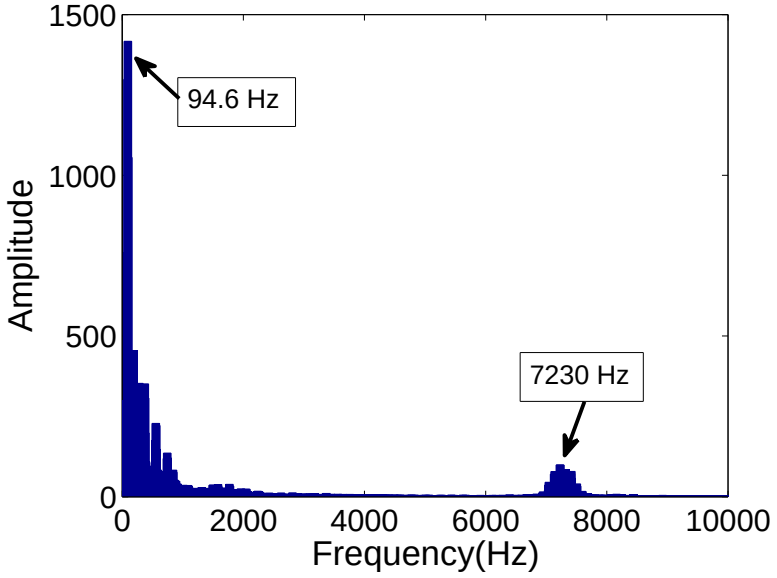

Figure 6.28: Fourier Transform Components from one of the numerical sensor at the inlet of R1 for case with VSVs mal-schedule

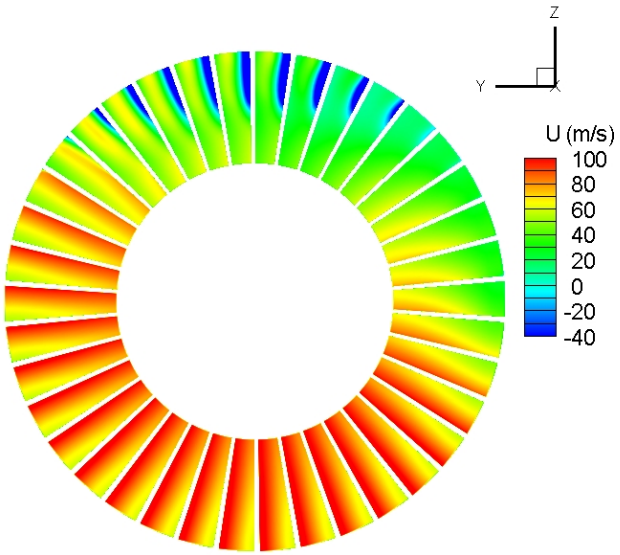

Figure 6.29: Instantaneous axial velocity in the middle of IGVs after 30 rev for MS case

middle of the IGV after 30 revolutions. Flow in approximately two fifths of the annulus was altered by the rotating stall cell in R1 due to its extension which indicates the downstream effects of flow in R1. Nine passages were stalled near the tip on the suction sides which was found in the middle of the IGV passages. They occupied up to 50% span in the radial direction.

Figure 6.30 shows the instantaneous negative axial velocity on an axial cut plane near the leading edge of R1 at different time frames. At 4th revolution, five stall cells were predicted and they tended to merge together. After another 6 revolutions, one large stall cell with one smaller cell were found. The regular pattern with one stall cell covering seven rotor passages was predicted after 20 revolutions. Stall cells were attached to casing and the pressure side of the rotor blades which had similar structure of radial vortex as reported by Pullan et al. [2012] and the one in NASA Rotor 37. The rotating stall cell occupied approximately 40% span in radial direction. On the axial plane located 50% chord length in the rotor as shown in Figure 6.31, stall cell in passages started to detach from the casing and moved towards the mid span, towards the rotor rotation direction. Stall cell in the regular pattern near the trailing edge of the rotor was detached completely from the casing,

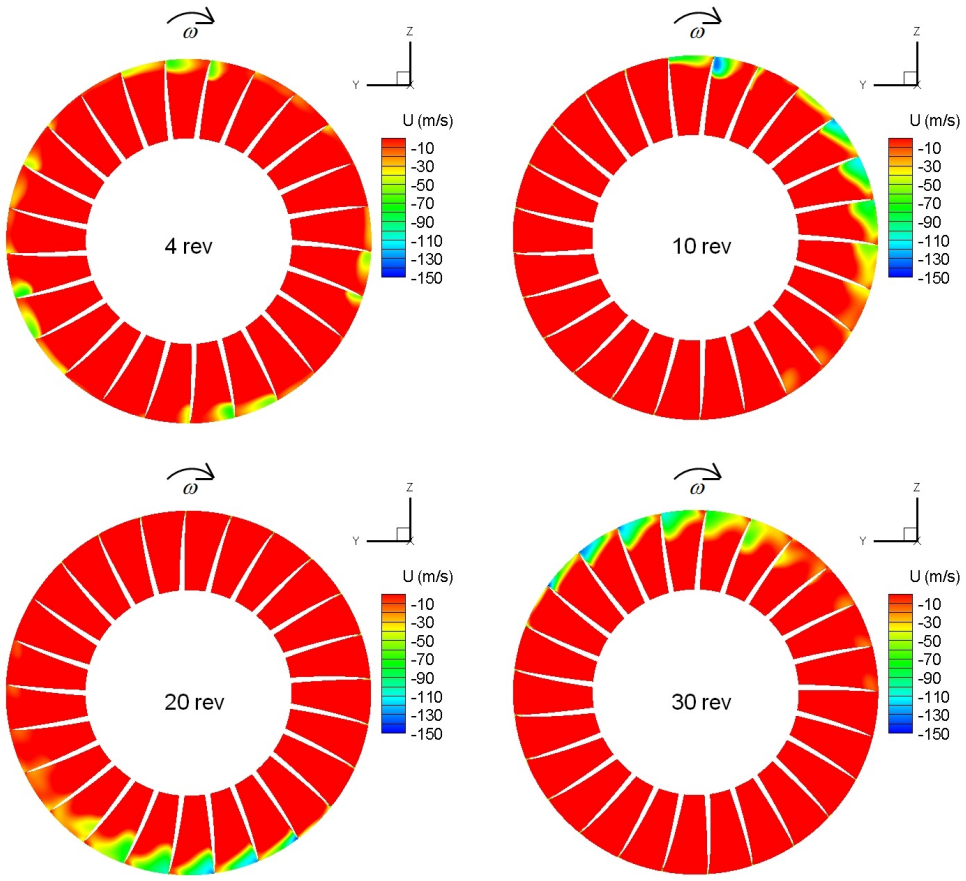

Figure 6.30: Instantaneous negative axial velocity on axial cut planes near the leading edge of R1 at different time frames for MS case

shown in Figure 6.32. It suggests that the radial vortex was formed which was attached to the casing near the leading edge with legs spilled into the passages.

Figure 6.33 shows the instantaneous axial velocity contour plot which locates at 50% chord length of S1 after 30 revolutions. A large stall cell was also predicted due to flow condition in both R1 and R2. The large stall region occupied from 45% to 81% span. This was caused by the flow features in R1 in which the radial vertex of the stall cell detached from the casing. There were also stalled regions on the hub which were found few passages away in the anti-clockwise direction or opposite direction to shaft rotation. This stall cell is also rotating from time to time due to the flow characteristic in upstream and downstream rotors.

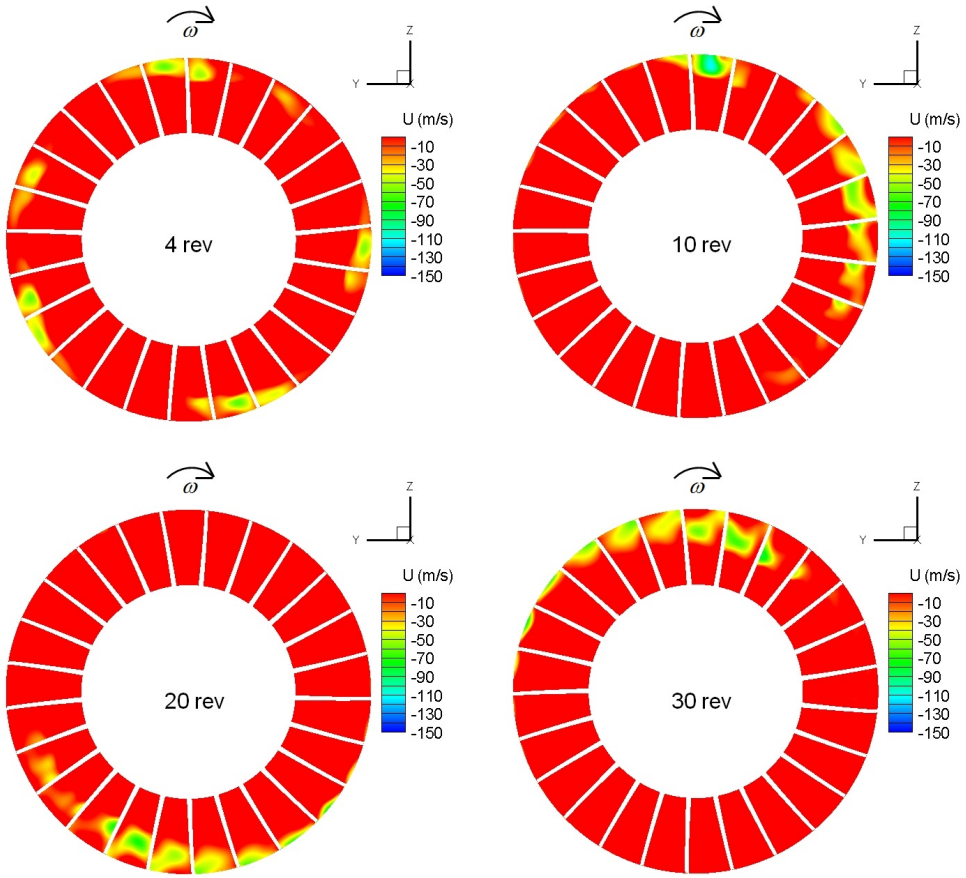

Figure 6.31: Instantaneous negative axial velocity on an axial cut plane in the middle of R1 at different time frames for MS case

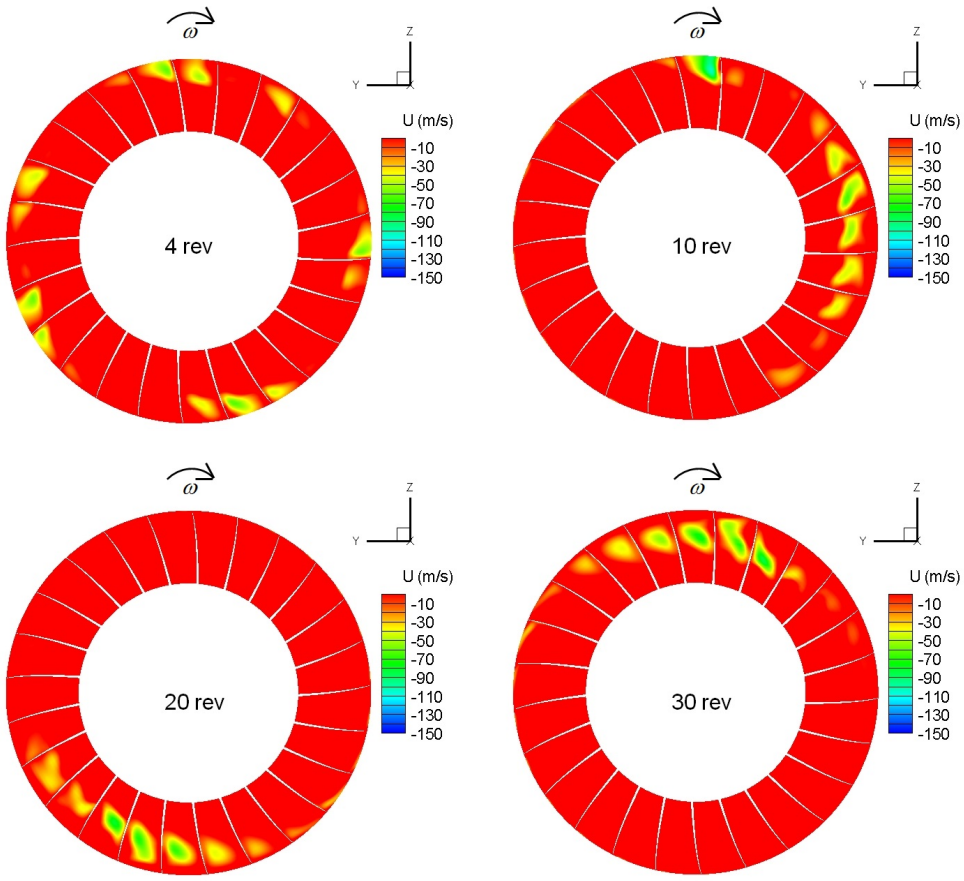

Figure 6.32: Instantaneous negative axial velocity on an axial cut plane near the trailing edge of R1 at different time frames for MS case

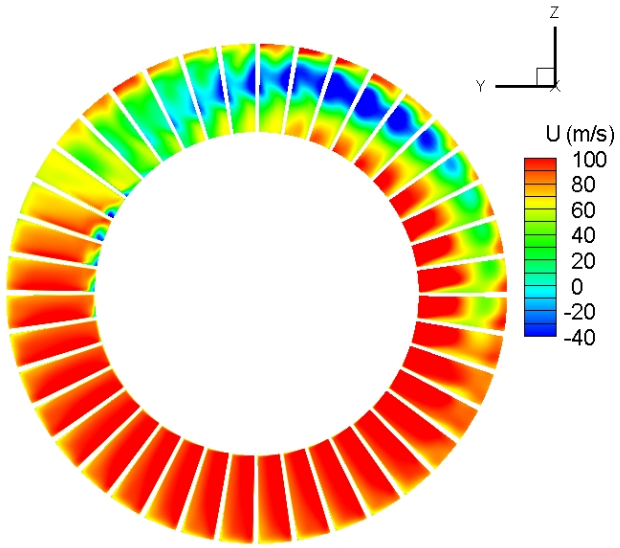

Figure 6.33: Axial velocity on an axial cut plane in the middle of S1 after 30 rev for MS case

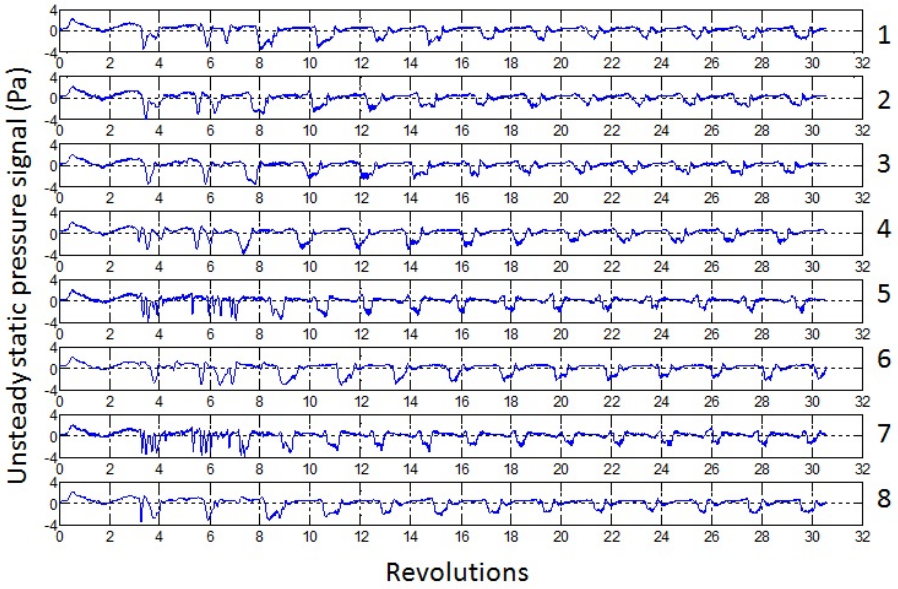

Figure 6.34: Unsteady static pressure signal time history from numerical sensor at the inlet of R2 for case with VSVs mal-schedule

6.6.2 Flow in stage 2

Figure 6.34 shows the unsteady static pressure signal upstream of R2. Rotating stall starts after 3 revolutions with 6 stall cells firstly formed in R2. As reported by Longley et al. [1996], in multi-stage compressors, downstream stages would operate with inlet flow nonuniformity or rotating inlet distortion when upstream stages encountered rotating stall, due to stage interaction. Therefore, it is believed that rotating stall in stage 2 was caused by the one in R1. After 8 revolutions shown in the plot, those cells merged to one large stall cell. The period of the stall cell passing along one circumference of R2 required two rotor rotations which provides the propagation speed of the stall cell is also approximately 50% of shaft speed. The propagation speed of rotating stall in R2 could also be obtained from Figure 6.35. It shows the Fourier Transform from numerical sensors at the inlet of R2. As shown in the figure, there are also two main frequencies: 94.6 Hz and 7,710 Hz. The first frequency is for the rotating stall and the second is the frequency of R2 passing S1.

Figure 6.36 shows the instantaneous negative axial velocity on an axial cut plane near the leading edge of R2 at different time frames. At the 4th revolution, five

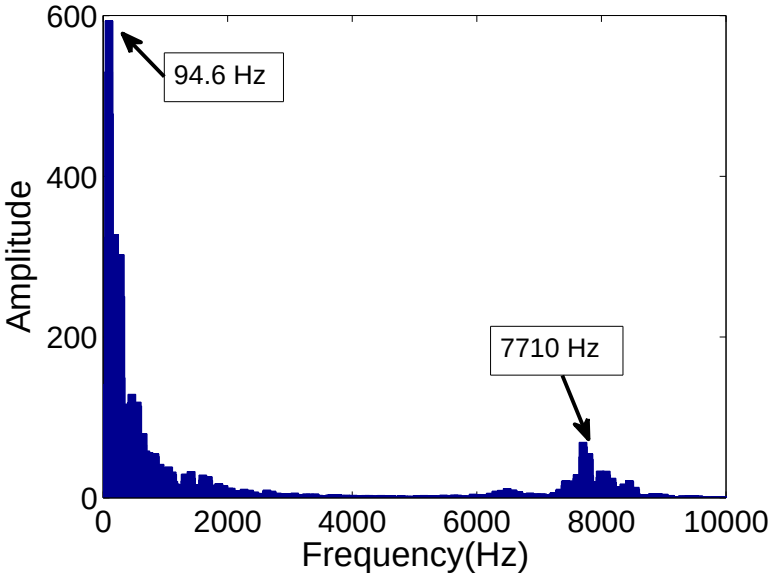

Figure 6.35: Fourier Transform Components from one of the numerical sensor at the inlet of R2 for MS case

rotating stall cells were found, the same as in R1 but at different locations with phase difference in the circumferential direction. It could be due to the difference in the number of blades compared with R1 and rotating stall was also still developing. At the 10th revolution, only one large stall cell was found at the same circumferential location. The regular pattern has already been achieved at the 20th revolution with flow blockage in seven passages. As shown in Figure 6.37 which is the instantaneous negative axial velocity contour plot on an axial cut plane in the middle of R2 at different time frames, the radial vortices tended to detach from the casing after a regular pattern was obtained. Similar as in R1, the radial vortices detached from the casing and moved towards the middle of the passage as shown in Figure 6.38 which shows the instantaneous negative axial velocity contour plot on an axial cut plane near the trailing edge of R2 at different times. The similarity between the rotating stall cell in both R1 and R2 also suggests that rotating stall in R2 could be caused by rotating stall in R1.

Figure 6.39 shows the instantaneous axial velocity contour plot on an axial cut plane located approximately 50% chord length in S2 obtained after 30 revolutions. The flow blockage in the upper part of the annulus was caused by the downstream

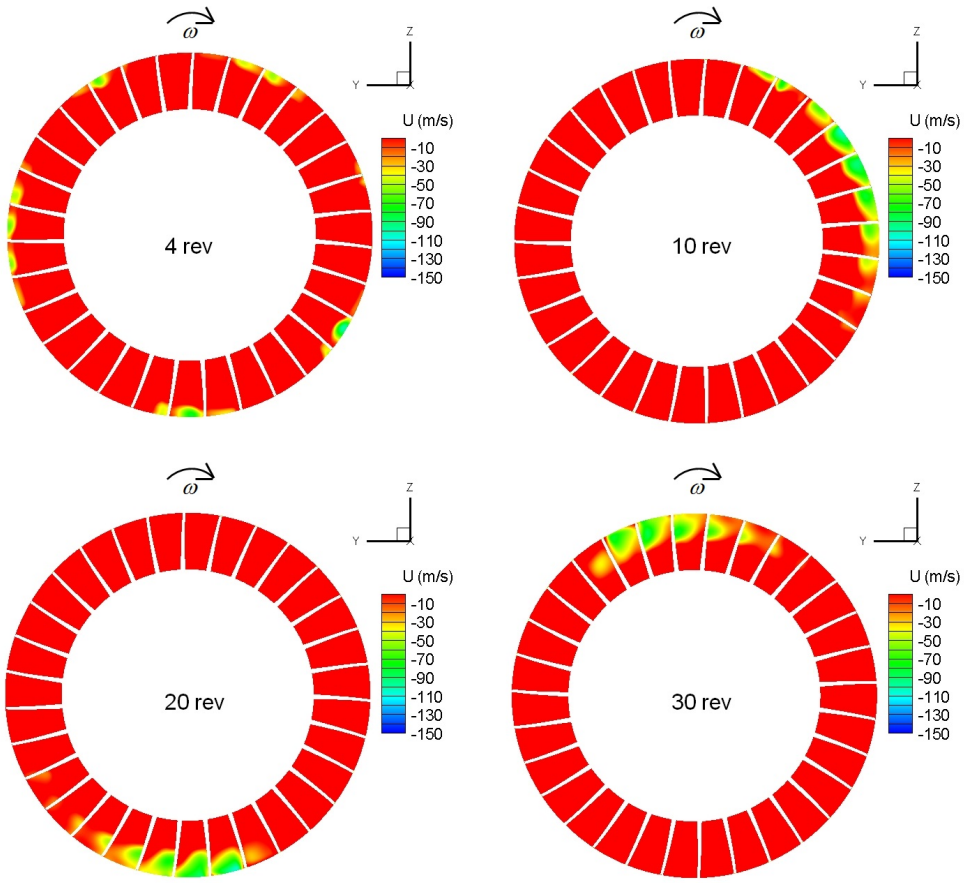

Figure 6.36: Instantaneous negative axial velocity contour plot on an axial cut plane near the leading edge of R2 at different time frames for the MS case

effect of R2 which also rotated around the annulus at half shaft speed. As also can be seen in the figure, stalled regions were found near the hub in most of blade passages. The reason could be that there was flow separation observed near the hub at the near stall point as discussed from the steady state solution. That flow separation was caused by the degradation in incidence by staggering S2. It also exists in the near stall point from steady state solutions as discussed earlier. Therefore, it is reasonable that flow separation would still exist when throttled this compressor further.

6.6.3 Flow in stage 3

Figure 6.40 shows the unsteady static pressure signal at the upstream of R3. Rotating stall also starts after approximately 3 revolutions. One large stall cell was

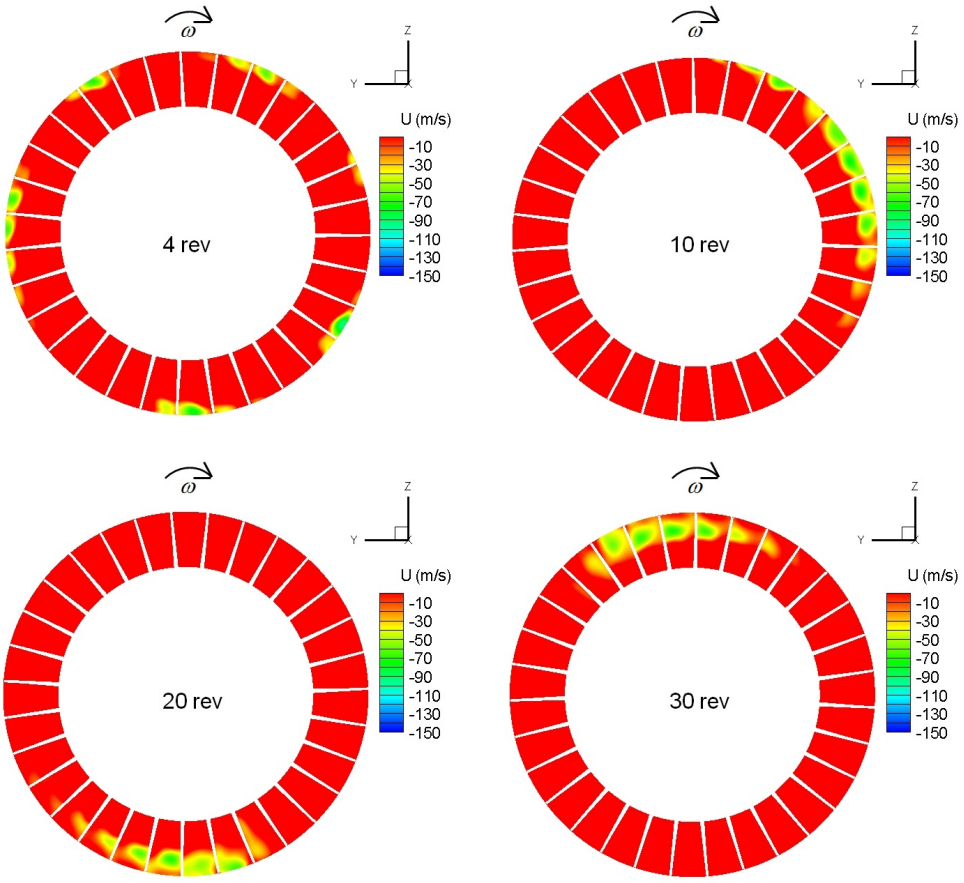

Figure 6.37: Instantaneous negative axial velocity contour plot on an axial cut plane in the middle of R2 at different time frames for the MS case

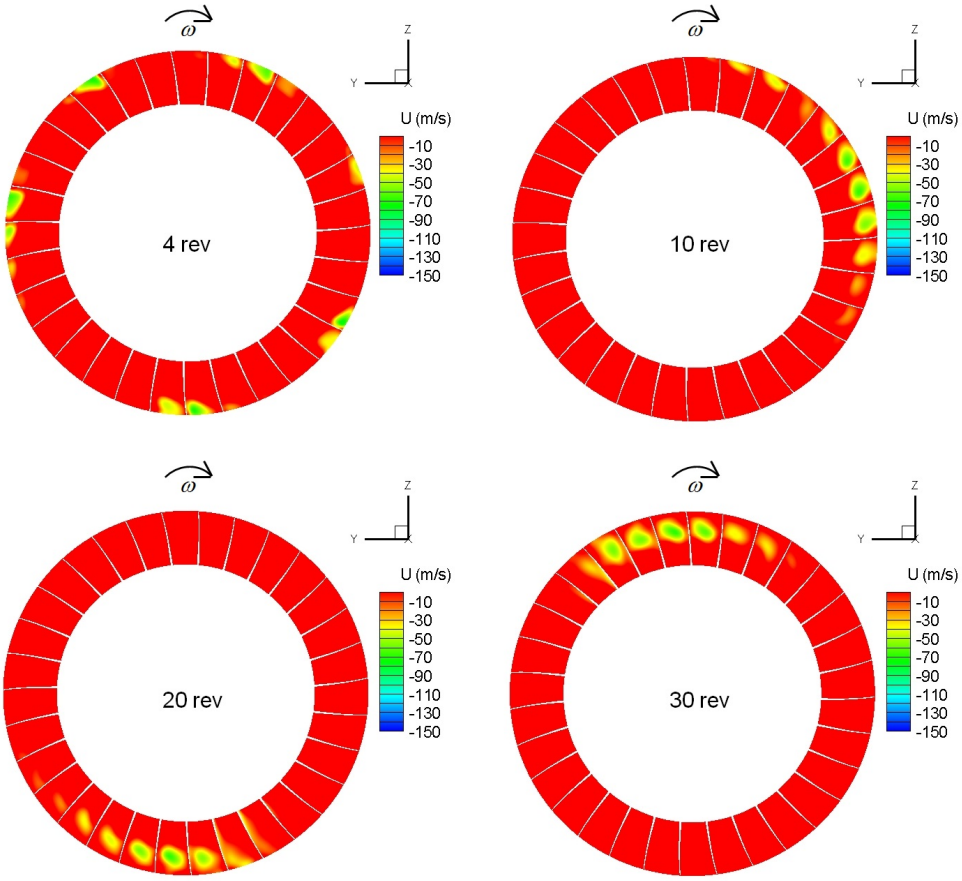

Figure 6.38: Instantaneous negative axial velocity contour plot on an axial cut plane near the trailing edge of R2 at different time frames for the MS case

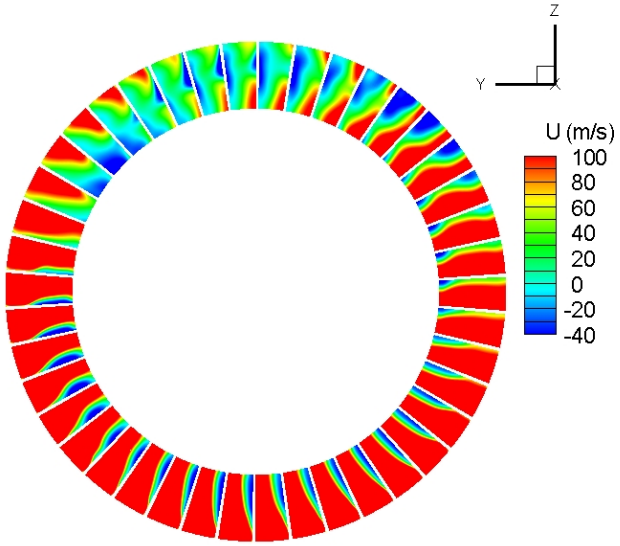

Figure 6.39: Instantaneous axial velocity contour plot in the middle of S2 after 30 rev for the MS case

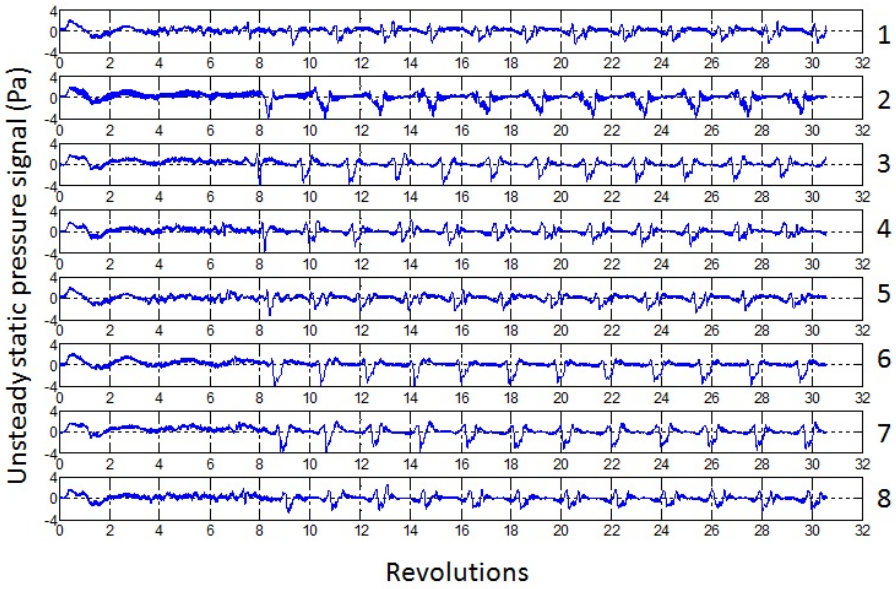

Figure 6.40: Unsteady static pressure signal time history from numerical sensor at the inlet of R3 for case with VSVs mal-schedule

formed after 8 revolutions. Rotating stall had the same propagation speed as in the other two rotors. Again, the rotating stall in R3 is believed to be caused by the rotating stall in the upstream stages. Figure 6.41 shows the Fourier Transform from numerical sensors at the inlet of R3. There are three main frequencies in the plot: 94.6 Hz and 7,520 Hz. The first frequency is the frequency for rotating stall and the second one is the blade passing frequency for R3.

Figure 6.42 shows the instantaneous negative axial velocity on an axial cut near the leading edge of R3 at different time frames. At the 4th revolution, only a very small negative cell attached to the casing was predicted. At the 10th revolution, one large stall cell was found covering nine passages in the circumferential direction. In one rotor passage, the stalled flow was predicted locating at the lower part of the blade passages close to the hub which was caused by the flow blockage near the hub in S2. Stalled region tended to be moved to the tip region of R3 due to the centrifugal effects. Figure 6.43 shows the instantaneous negative axial velocity on a axial cut in the middle of R3 at different time frames. At the 4th revolution, three stall cells were found. They merged into one at the 10th revolution. Stall cell slightly detached from the casing. Figure 6.44 shows the instantaneous negative

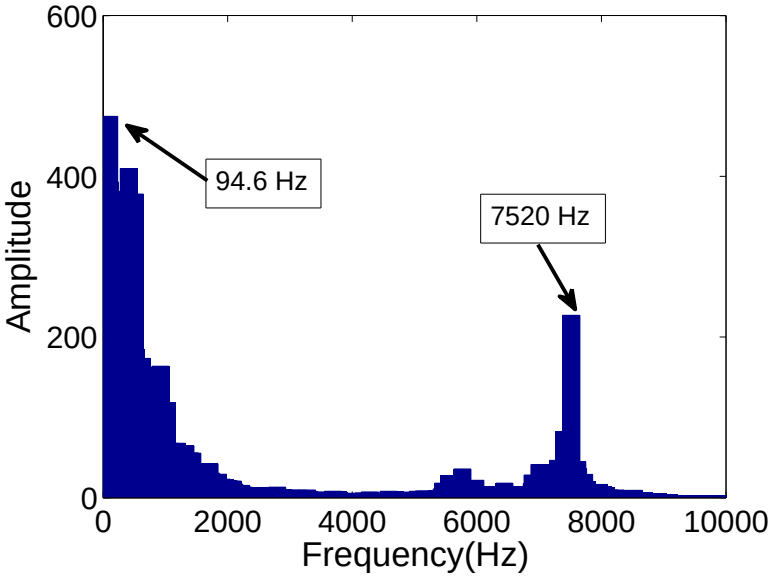

Figure 6.41: Fourier Transform Components from one of the numerical sensor at the inlet of R3 for case with VSVs mal-schedule

axial velocity on an axial cut plane near the trailing edge of R3 at different times. After a regular pattern was predicted, the stall cell was completely detached from the casing.

Rotating stall cell was also found in S3 as shown in Figure 6.45. Stall cell had the same shape as in R3. It could be seen that a few stalled regions were close to the hub of S3. That was caused by the design of this stator as discussed before in the Nominal case and also reported in the experimental work. Therefore, the rotating stall pattern in R3 was also affected by this feature. With blade rotation, rotating stall cell in R3 had a "parabolic" shape due to the centrifugal effects. The stalled flow near the tip region in S3 was affected by that due to the downstream effects of R3.

To sum up, spike type rotating stall was also predicted for the IDAC compressor. It was found in all three rotors with the same propagation speed which was half of the shaft speed, suggesting that rotating stall in downstream stages was caused by the one in stage 1. Rotating stall started first in R1 which indicated that it was responsible for the rotating in this compressor. That also confirms the hypothesis in the stall indicator study discussed at the beginning of the chapter. The radial

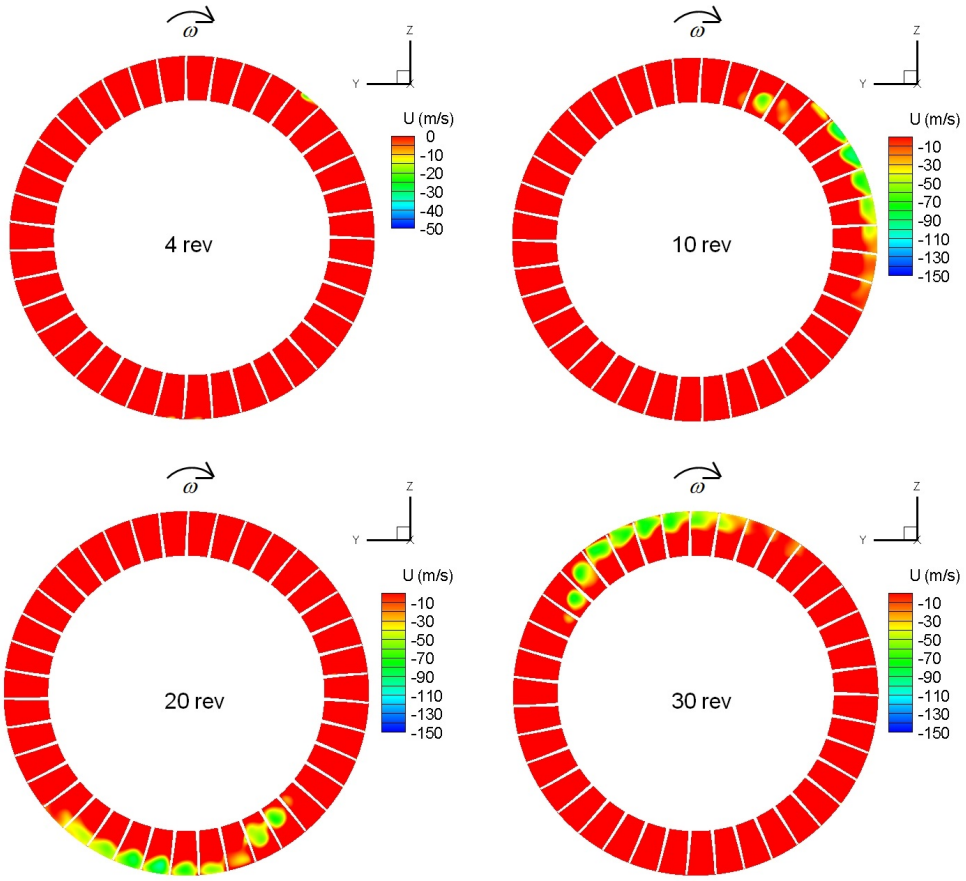

Figure 6.42: Instantaneous negative axial velocity on the axial plane near the leading edge of R3 at different time frames for the MS case

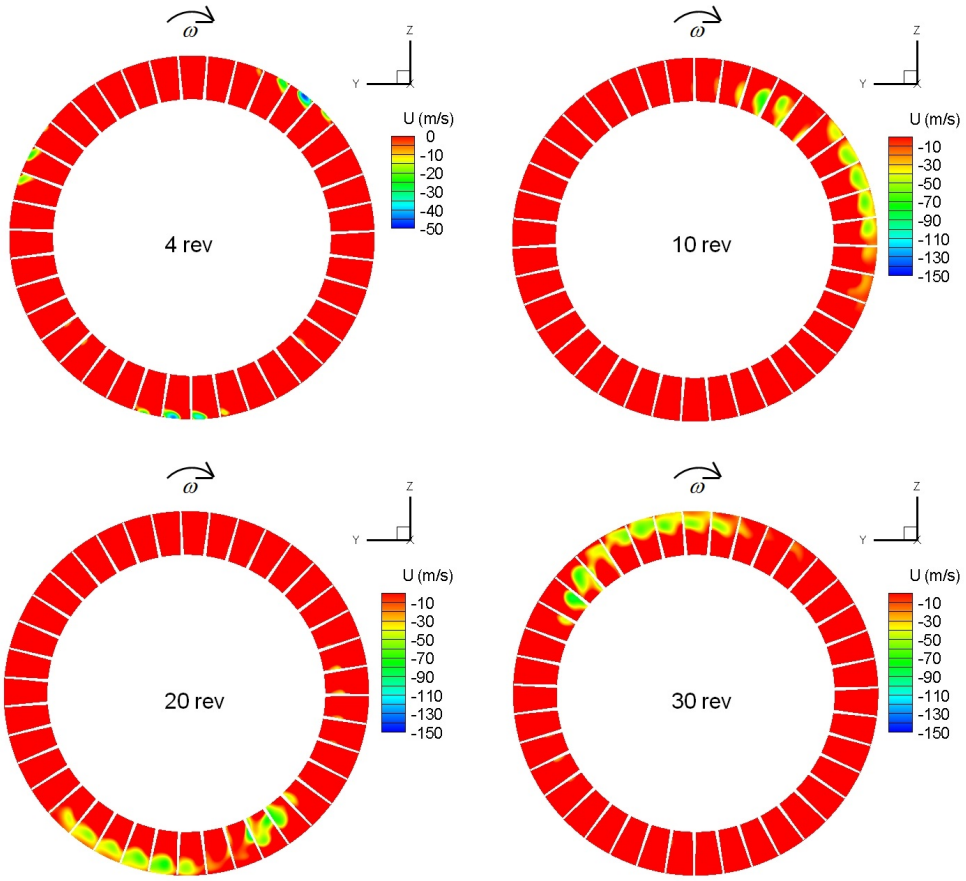

Figure 6.43: Instantaneous negative axial velocity on the axial plane in the middle of R3 at different time frames for the MS case

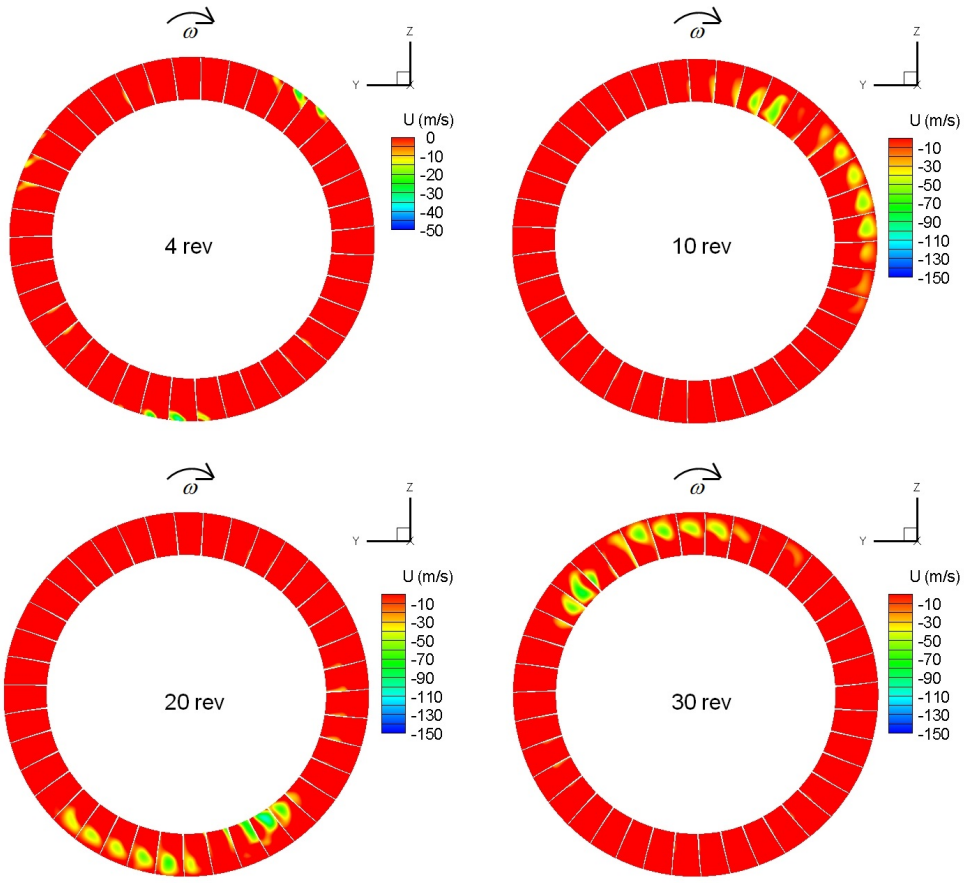

Figure 6.44: Instantaneous negative axial velocity on the axial plane near the trailing edge of R3 at different time frames for the MS case

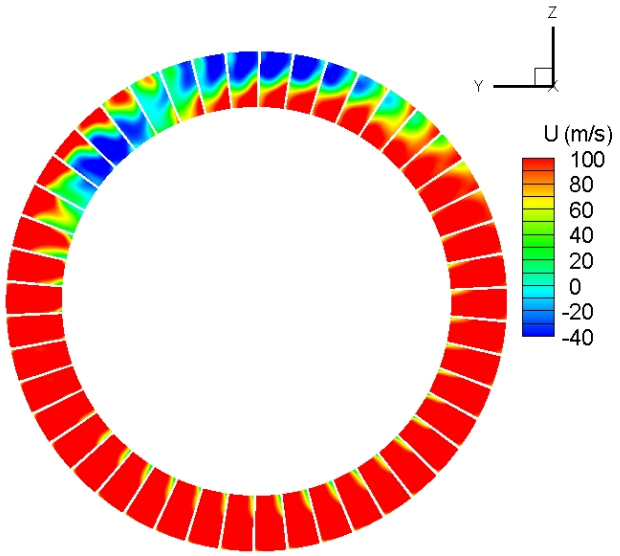

Figure 6.45: Negative axial velocity on the axial plane in the middle S3 after 30 rev for the MS case

vertices for all rotors were attached to the casing and the pressure side of the blades near the leading edge. They were detached from the casing and moved to the middle of the passages towards trailing edge. Furthermore, stall cells predicted in stators were also propagating from time to time due to the effects of upstream and/or downstream rotors.

6.7 Summary

In this chapter, a 3.5 stage high speed axial flow compressor is used to study the VSVs mal-schedule effect on compressor aerodynamics. By analysing the steady state solutions at near stall conditions, it was assumed that R1 could be responsible for the initiation of rotating stall if the compressor is throttled further close to the stall boundary. The main reason for this was that R1 was operating at a higher throttling line with higher incidence compared with downstream rotors for both the Nominal case and the MS case.

Unsteady full annulus simulations were performed at 68% of rotor speed for both two different blade configurations. They were investigated with the same upstream and downstream boundary conditions. The Nominal case was investigated for comparison purposes to study VSVs mal-schedule effects. Surge cycles were predicted with a frequency of 108 Hz. S3 was found to be the reason triggering surge agrees with the general principle and the literature.

In the MS case, part span spike type initiated rotating stall was predicted. The formation and propagation mechanisms were the same as the one in NASA Rotor 37. Rotating stall was predicted in all rotor bladerows and the one in R2 and R3 were believed to be caused by the the one in R1 which was acting as an inlet rotating distortion. All stall cells rotate around the annulus at approximately 50% of shaft speed. Only one large stall cell covering several blade passages was predicted in all rotor bladerows.

The MS case was expected to be less stable than the Nominal case. However, surge cycles were predicted in the Nominal case while rotating stall was predicted in

the MS case. It seemed that the Nominal case was less stable due to the particular design of S3 which was originally designed to be highly loaded and had separations near the hub even at design condition. In the MS case, flow condition in S3 was improved due to the opening of S2. Furthermore, the geometry was completely altered by the MS mal-schedule. Even though the same downstream nozzle size was used for both the Nominal case and the MS case, they did not have the same operating condition in terms of mass flow and pressure ratio on the characteristic map. Without the whole overall characteristic from unsteady simulations, it is not possible to study the MS effect on the rotating stall characteristics and surge margin based on the available data.

Chapter 7

Conclusions and recommendations

In this research, the effects of compressor deterioration, including blade damage and VSVs mal-schedule, on compressor performance especially at near stall boundary were investigated through time-accurate unsteady simulations at off-design conditions. Blade damage effects were investigated firstly using a transonic single stage axial compressor rotor, NASA Rotor 37. Two aspects were investigated: 1) study of different degrees of one damaged blade; 2) study of multiple damaged blades with identical medium degree of damage. Before the time-accurate unsteady simulations, the inhouse CFD code SURF used was validated with experimental data using steady state simulations. Secondly, the effect of VSVs mal-schedule was investigated using a 3.5 stage axial compressor at 68% of design speed. Although there were no VSVs in the original design, the first two stators were assumed to be VSVs. Steady state simulations were performed firstly in an attempt to find the indicators for rotating stall, particularly by analysing the flow at near stall conditions. Then time-accurate unsteady simulations were analysed and discussed for the assemblies with nominal blade settings (the Nominal case) and the case with VSVs mal-schedule (the MS case). The main findings will be listed first for both studies and then recommendations will be given based on the outcomes of this research.

7.1 Main findings of the blade damage study

The blade damage study was presented in Chapters 4 and 5 through time-accurate unsteady simulations. All unsteady simulations were performed at 60% of the design speed. For comparison purposes, a case without damaged blades was also investigated. For that case, it was firstly investigated away from stall boundary. Time averaged solutions were then compared with steady state solution with the same inlet and outlet boundary conditions. Results show that they have very good agreement including overall performance and blade pressure profiles at different spans. It further validated the unsteady feature of the numerical methods which provided confidence in the unsteady simulations.

Then the case without damaged blades was investigated at near stall condition. From its overall performance during rotating stall, mass flow rate was found to be similar to the near stall point from steady state solutions and settled to a very small range with time after a fully developed rotating stall pattern was achieved. However, the pressure ratio during rotating stall was reduced by approximately 1%. The reason for the mass flow being less affected is that it was compensated in other unstalled regions. The circumferentially averaged axial velocity near the tip region with rotating stall was higher than the steady state solution. It resulted from that increased mass flow was achieved in the unstalled passages near the tip due to reduced incidence which compensated for the deficit from the stalled passages.

Part span spike type rotating stall was predicted in the undamaged case. From the initiation to the fully developed pattern, three different rotating stall patterns were encountered which could be seen from the pressure signals and mass flow variation time history and flow animations. The regular pattern has 6 stall cells rotated along the rotor annulus in the same direction of rotor rotation with a propagation speed of 83% of shaft speed.

Stall cells confined to the tip region is one of the characteristics of spike type rotating stall as reported by Day [1993]. The mechanism of this type of rotating stall and the role of tip clearance flow are consistent with proposals reported by Vo et al.

[2008]. Stall cells are approximately equally spaced and cover two rotor passages in the circumferential direction and about 17% in the span-wise direction. The similarity of flow feature regarding the radial vortex and its propagation mechanism conforms to those reported by Inoue et al. [2000], Weichert and Day [2012] and Pullan et al. [2012].

A compressor rotor assembly with three different blade damage settings were then investigated and they were also compared with the undamaged case. It was found that damaged blades do not have significant effects on this compressor's overall performance for the damage analysed. Spike type initiated rotating stall was predicted in all cases and the corresponding flow features were found to be similar to those reported in the literature. For the assembly with one medium damaged blade and the nominal blade settings, two operating points on the compressor characteristics were investigated: one away from stall boundary and the other near stall boundary. When the compressor was operating away from stall, the flow separation was restricted to the surrounding passages of the damaged blade and flow was compensated in other passages.

At near stall condition, the assembly with one medium damaged blade has a similar stable and clear rotating stall pattern except one non-rotating stall region caused by the damaged blade. When increasing the degree of damage on the blade, spike type rotating stall was found as well but with a different pattern. Both the number of stall cells and the non-rotating stall region were increased. In the case with six damaged blades with identical medium damage, a large stationary stalled region was found which covered approximately quarter of the annulus and three other cells rotated around the annulus at irregular patterns. It was found that it was more difficult for the flow to settle and achieve a regular pattern when the degree of damage or number of damaged blades was increased. For all cases with rotating stall, mass flow was not significantly affected compared with the steady-state simulations because the flow deficit was also compensated by increased flow in the unstalled passages.

For one damaged blade with two different degrees of damage the stall cells rotated in the same direction of rotor rotation with the same propagation speed as the undamaged case. Stall cells were also approximately equally spaced and covered two rotor passages in the circumferential direction and with similar radial extent of the passage in the span-wise direction. The flow features regarding the radial vortex and its propagation mechanism also conform to those reported in the literature for undamaged assemblies.

To conclude, the numerical method is capable to simulate rotating stall phenomenon with blade damage. However, tip curl damaged blades investigated did not have significant effects on compressor overall performance. Since the unsteady full annulus simulations require extensive computational resources, it was not possible to perform a detailed parametric study to find the degree of damage which would have detrimental aerodynamic effects on the compressor.

7.2 Main findings of the VSVs mal-schedule study

In this study, a 3.5 stage high speed axial flow compressor was used to study the VSVs mal-schedule effects on compressor aerodynamics, especially at near stall boundary at off-design condition. By analysing the steady state solutions near stall boundary, it was expected that R1 would be responsible for the initiation of instabilities if the compressor is throttled further. The main reason for this was that R1 was operating at a higher throttling line with higher incidence compared with downstream rotors for both the Nominal case and the MS case.

Unsteady full annulus simulations were performed at 68% of rotor speed for both two different blade configurations. They were investigated with the same upstream and downstream boundary conditions. The Nominal case was investigated for comparison reason to study VSVs mal-schedule effects. Surge cycles were predicted with a frequency of 108 Hz with nominal vane settings. It is possible that this case would never go to rotating stall. However, it cannot be proved by one simulation. S3 was found to be the trigger for surge which agrees with the general principle for surge

in the literature.

In the MS case, spike-type initiated rotating stall was predicted for this compressor. The formation and propagation of spike structure were similar to the one predicted in the blade damage study. Rotating stall was predicted in all rotor bladerows and the one in R2 and R3 were believed to be caused by the one in R1 which was acting as an rotating inlet distortion for downstream stages. All stall cells rotate around the annulus at about 50% of shaft speed. Only one large stall cell covering several blade passages was predicted in all rotor bladerows.

The MS case was expected to be less stable than the Nominal case. Contrary to expectation, surge cycles were predicted in the Nominal case while rotating stall was predicted in the MS case. Further analysis shows that the Nominal case was less stable due to the particular design of S3 which was originally designed to be highly loaded and had separations near the hub even at design conditions. In the MS case, the flow condition in S3 was improved due to the opening of S2. Furthermore, the geometry was completely altered by the VSVs mal-schedule.

To conclude, the numerical method is capable of predicting surge cycles and simulating rotating stall phenomenon with VSVs mal-schedule. Even though the same downstream nozzle size was used for both the Nominal case and the MS case, however they did not have the same operating condition in terms of mass flow and pressure ratio on the characteristic map. Without the whole overall characteristic from unsteady simulations, it is not possible to study the MS effect on the rotating stall characteristics and surge margin.

7.3 Recommendations for future work

The research presented in this thesis has provided information that are important to compressor designers. However, there are some limitations for this research which needed to be taken into account to improve the understanding of the effects of blade damage and VSVs mal-schedule in axial flow compressors. The following suggestions would help further understanding in this research area.

Specific recommendations regarding blade damage and VSVs mal-schedule

In the blade damage study, two different degrees of tip curl damaged blades and multiple damaged blades with identical damage located next to each other were investigate. However, results showed that they did not have significant degradation on the overall compressor performance. Therefore, it is recommended that to investigate damage on different locations in the span-wise direction and different damaged blade arrangement with heavy degree of damage in the circumferential direction.

For the VSVs mal-schedule study, only one configuration of stator vane settings was investigated. Furthermore, it is possible for the case with nominal blade settings to operate at slightly different conditions even with the same size downstream nozzle. Therefore, it is desirable to investigate the Nominal case to find the operating condition for rotating stall to happen, by slightly opening the nozzle. On the other hand the compressor investigated, IDAC, was not a representative design for high speed compressors with the highly loaded design for the last stator. In the meantime, the first two stators were assumed to be VSVs although it does not have VSVs for the original design. Thus, investigations on a different compressor configuration are highly recommended. Moreover, in actual engines, VSVs are bolted to the casing and hub with small radial tip and hub clearances between the vanes and the wall. That configuration could cause flow spoiling features near those gap regions and these should be taken into account in the future work.

Unsteady validation using experimental data

In this thesis, one of the limitations is that there are no experimental data available for the unsteady time accurate simulations. Even though the numerical method used was validated for steady state simulations with experimental data discussed in Chapter 3 and the unsteady features were also validated by other researchers as reported in the literatures, it is still desirable and will be very helpful to investigate a compressor with rotating stall experimental data available.

Unsteady verification using other turbulence models

All analyses conducted during the course of the research were performed using the one equation Spalart-Allmaras turbulence model. Although it was shown to be capable of providing a good compromise between cost and accuracy reported by Gourdain et al. [2010] as discussed in Chapter 2. With the fast development in computing technology and parallelisations of CFD simulations, investigations are recommended to find or develop more accurate turbulence models for this type of simulations.

Coupling with aeroelasticity investigations

As reported by Vahdati et al. [2008], blade vibrations or deflections could be generated by periodically extra forces or loading and unloading on the blades which are synchronized when the compressor is operating during rotating stall and surge in real engines. That is why aeroelasticity investigations are important under those conditions. However, there are difficulties for the coupling of flow model with structural model. Nevertheless, it is still desirable to have aeroelasticity models together with flow model for rotating stall investigations.

References

E. H. Abed, P. K. Houpt, and W. M. Hosny. Bifurcation analysis of surge and rotating stall in axial flow compressors. *Technical Research Report: TR 90-27r2, University of Maryland*, 1991. 11

A. A. Ameri. NASA Rotor 37 CFD code validation. *NASA/CR-2010-216235*, 2010. 34

A. Arnone, M.-S. Liou, and L. A. Povinelli. Integration of Navier-Stokes equations using dual time stepping and multigrid method. *AIAA Journal*, 33(6):985–990, 1995. 32

S. Audic, M. Berthillier, H. Bung, and A. Letellier. Bird impact analysis on aero-engine fan blades. *ISABE 99-7082*, 1999. 23

V. S. Beknev, A. V. Zemlyanskiy, and Tumashev R. Z. Experimental study of rotating stall in high-pressure stages of an axial-flow compressor. *NACA TT F-15,115*, 1973. 12

M. A. Bennington and J. Du. An experimental and computational investigation of tip clearance flow and its impact on stall inception. *Proceedings of ASME Turbo Expo 2010: Power for Land, Sea and Air*, 2010. 15, 21

W. A. Benser. Analysis of part-speed operation for high-pressure-ratio multistage axial-flow compressors. *NACA RM E53115*, 1953. 11

J. Bergner, M. Kinzel, and H. Schiffer. Short length-scale rotating stall inception in

a transonic axial compressor-experimental investigation. *Proceedings of GT2006 ASME Turbo Expo 2006: Power for Land, Sea and Air*, 2006. 18, 21

S. Bindl, M. Stobel, and R. Niehuis. Stall detection within the low pressure compressor of a twin-spool turbofan engine by tip flow analysis. *Proceedings of ASME Turbo Expo 2009: Power for Land, Sea and Air*, 2009. 11

B. Bohari and A. I. Sayma. CFD analysis of effects of damage due to bird strike on fan performance. *Porceedings of ASME Turbo Expo: Power for Land, Sea and Air*, 2010. 24

A. Bohne and R. Niehuis. Experimental off-design investigation of unsteady secondary flow phenomena in a three-stage axial compressor at 68% nominal speed. *Porceedings of ASME Turbo Expo 2004: Power for Land, Sea and Air*, 2004. 99, 102, 121, 123

N. Cai, A. Benaissa, and W. D. Allan. Aerodynamic-aeroacoustic investigation of rotating stall in conventional and skewed rotors. *Proceedings of ASME Turbo Expo 2004: Power for Land, Sea and Air*, 2004. 14

T. R. Camp and I. J. Day. A study of spike and modal stall phenomena in a low-speed axial compressor. *Transactions of the ASME, Journal of Turbomachinery*, 120:393–401, 1998. 5

C. E. Campbell. Performance of basic XJ79-GE-1 turbojet engine and its components. *Natinoal advisory commitee for aeronautics*, 1958. 6, 24

S. R. Chakravarthy. Relaxation method for unfactored implicit upwind schemes. *AIAA Paper No. 84-0165*, 1984. 32

J. P. Chen, M. D. Hathaway, and G. P. Herrick. Pre-stall behavior of a transonic axial compressor stage via time-accurate numerical simulation. *ASME: Journal of Turbomachinery*, 130:041014–1–12, 2007. 20

R. V. Chima. A three-dimensional unsteady CFD model of compressor stability. *NASA/TM-2006-214117*, 2006. 19

M. Choi, H. O. Seong, Y. K. Han, and J. H. Baek. Effects of the inlet boundary layer thickness on rotating stall in an axial compressor. *Proceedings of ASME Turbo Expo 2008: Power for Land, Sea and Air*, 2008. 13

M. Choi, M. Vahdati, and M. Imregun. Effects of fan speed on rotating stall inception and recovery. *Journal of Turbomachinery*, 133:041013–1–8, 2011. 14

M. Choi, N. H. S. Smith, and M. Vahdati. Validation of numerical simulation for rotating stall in a transonic fan. *Proceedings of ASME Turbo Expo 2011*, 2011b. 22

D. Christensen, P. Cantin, D. Gutz, P. N. Szucs, A. R. Wadia, J. Armor, M. Dhingra, Y. Neumeier, and J. V. R. Prasad. Development and demonstration of a stability management system for gas turbine engines. *ASME: Journal of Turbomachinery*, 130:031011–1–9, 2008. 11

V. Cyrus. An experimental study of stall in four axial compressor stages. *Proceedings of ASME TURBO EXPO 2000*, 2000. 15

I. J. Day. Stall inception in axial flow compressors. *ASME Journal of Turbomachinery*, 115:1–9, 1993. 16, 71, 146

I. J. Day and C. Freeman. The unstable behaviour of low and high speed compressors. *ASME Journal of Turbomachinery*, 116:194–201, 1994. 71

B. de Jager. Rotating stall and surge control: A survey. *Proceedings of the 34th Conference on Decision & Control*, 1995. 2

J. D. Denton. Lessons from Rotor 37. *Journal of Thermal Science*, 6:1–13, 1996. 38, 44

S. Dhandapani, M. Vahdati, and M. Imregun. Forced response and surge behaviour of IP core-compressors with ice-damaged rotor blades. *Proceedings of ASME Turbo Expo: Power for Land, Sea and Air*, 2008. 24

R. W. Eustace, B. A. Woodyatt, G. L. Merrington, and A. Runacres. Fault signatures obtained from fault implant tests on an F404 engine. *ASME J. Eng. Gas Turbines Power*, 116:178–183, 1994. 25

M. R. Feulner, G. J. Hendricks, and J. D. Paduano. Modelling for control of rotating stall in high-speed multistage axial compressors. *ASME: Journal of Turbomachinery*, 118:1–10, 1996. 11

C. Freeman. Stall in axial flow aero engine compressors. *Axial Flow Compressors, von Karman Institute for Fluid Dynamics*, 1992. 14

J. Frischbier and A. Kraus. Multiple stage turbofan bird ingestion analysis with ALE and SPH methods. *MTU Aero Engine GmbH,D-80976,Germany*, 2005. 24

K. Goebel, N. Eklund, and B. Brunell. Rapid detection of faults for safety critical aircraft operation. *IEEE*, 2004. 25

Y. Gong. A computational model for rotating stall and inlet distortions in multistage compressors. *Doctorate thesis from Massachusetts Institute of Technology*, 1999. 4

N. Gourdain, S. Burguburu, F. Leboeuf, and H. Miton. Numerical simulation of rotating stall in a subsonic compressor. *Aerospace Science and Technology*, 10: 9–18, 2006a. 19

N. Gourdain, S. Burguburu, G. J. Michon, N. Ouayahya, F. Leboeuf, and S. Plot. About the numerical simulation of rotating stall mechanisms in axial compressors. *Proceedings of GT2006 ASME Turbo Expo 2006: Power for Land, Sea and Air*, 2006b. 19

N. Gourdain, S. Burguburu, F. Leboeuf, and G. J. Michon. Simulation of rotating stall in a whole stage of an axial compressor. *Computers & Fluids*, 39:1644–4655, 2010. 21, 151

E. M. Greitzer. Surge and rotating stall in axial flow compressors, Part I: Theoretical compression system model. *Journal of Engineering for Power*, 98:190–198, 1976. 11

E. M. Greitzer. The stability of pumping systems-The 1980 Freeman Scholar Lecture. *ASME J. Fluids Eng.*, 103(2):193–242, 1981. 2

E. M. Greitzer and F. K. Moore. A theory of post-stall transients in axial compression systems: Part II-application. *ASME J. Eng. for Gas Turbines and Power*, 108:231–239, 1986. 11

Y. Guan, Zh. Zhao, W. Chen, and D. Gao. Foreign object damage to fan rotor blades of aeroengine Part II: Numerical simulation of bird impact. *Chinese Journal of Aeronautics*, 21:328–334, 2008. 24

C. Hah. Large eddy simulation of transonic flow field in NASA Rotor 37. *NASA/TM-2009-215627*, 2009. 20, 49

C. Hah and D. C. Rabe. Role of tip clearance flows on flow instability in axial flow compressors. *ISABE-2001-1223*, 2001. 15

C. Hah, R. Schulze, S. Wagner, and D. K. Hennecke. Numerical and experimental study for short wavelength stall inception in a low-speed axial compressor. *ISABE 99-7033*, 1999. 17

M. D. Hathaway, J. Chen, R. S. Webster, and G. P. Herrick. Time accurate unsteady simulation of the stall inception process in the compression system of a US army helicopter gas turbine engine. 2004. 16

B. Hoss, D. Leinhos, and L. Fottner. Stall inception in the compressor system of a turbofan engine. *Transactions of the ASME*, 122:32–44, 2000. 14

M. Inoue, M. Kuroumaru, T. Tanino, , and M. Furukawa. Propagation of multiple short-length-scale stall cells in an axial compressor rotor. *ASME: Journal of Turbomachinery*, 122:45–54, 2000. 18, 73, 147

M. Inoue, M. Kuroumaru, S. Yoshida, , and M. Furukawa. Short and long length scale disturbances leading to rotating stall in an axial compressor stage with different stator/rotor gaps. *Transactions of the ASME*, 124:376–384, 2002. 13

H. Jiang, Y. Lu, Y. Wei, and Q. Li. Experimental investigation of the influence of inlet distortion on the stall inception in a low speed axial compressor. *Proceedings of ASME Turbo Expo 2009: Power for Land, Sea and Air*, 2009. 15

H.-P. Kau. Compressor matching and designing for tip clearance. *The RTO AVT lecture series on "Integrated multidisciplinary design of high pressure multistage compression systems"*, 1998. 25

M. K. Khalil and M. A. Hongwei. High speed inlet stage for an advanced high-pressure ratio core compressor: Numerical flow field prediction and verification. *13th International conference on Aerospace science and Aviation technology*, ASAT-13, 2009. 34

M. Kim, M. Vahdati, and M. Imregun. Aeroelastic stability analysis of a bird-damaged aeroengine fan assembly. *Aerospace Science and Technology*, 5:469–482, 2001. 23

C. Lakhwani. Rotating stall and casing wall boundary layers in an axial flow compressor. *Ministry of Defence (Procurement Executive) Aeronautical Research Council, C.P. No. 1255*, 1973. 13

J. Lepicovsky and E. P. Braunscheidel. Measurement of flow pattern within a rotating stall cell in an axial compressor. *NASA/TM-2–6-214270*, 2006. 19

P. Levine. Axial compressor performance and maintenance guide. *Electric Power Research Institute, Inc.*, 1998. 1, 2, 5, 6

G. W. Lewis, F. C. Jr Schwenk, and G. K. Serovy. Experimental investigation of transonic axial-flow-comopressor rotor with double-circular-arc airfoil. *NACA RM E53L21a*, 1954. 12

Y. Li and A. I. Sayma. Effects of blade damage on the performance of a transonic axial compressor rotor. *Porceedings of ASME Turbo Expo: Power for Land, Sea and Air*, 2012. 9, 105

Y. Li and A. I. Sayma. Numerical investigation of VSVs mal-schedule effects in a three-stage axial compressor. *Porceedings of ASME Turbo Expo: Turbine Technical Conference and Exposition*, 2014. 9

F. Lin, M. Li, and J. Chen. Long-to-short length scale transition: A stall inception phenomenon in an axial compressor with inlet distortion. *Porceedings of GT2005 ASME Turbo Expo 2005: Power for Land, Sea and Air*, 2005. 15

J. P. Longley. A review of nonsteady flow models for compressor stability. *ASME Journal of Turbomachinery*, 116:202–215, 1994. 11

J. P. Longley and T. P. Hynes. Stability of flow through multistage axial compressors. *ASME Journal of Turbomachinery*, 112:126–132, 1990. 12

J. P. Longley, H.-W. Shin, R. E. Plumley, P. D. Silkowski, I. J. Day, E. M. Greitzer, and C. S. Tan. Effects of rotating stall inlet distortion on multistage compressor stability. *ASME Journal of Turbomachinery*, 118:181–188, 1996. 17, 133

R. Mailach, I. Lehmann, and K. Vogeler. Rotating instabilities in an axial compressor originating from the fluctuating blade tip vortex. *ASME: Journal of Turbomachinery*, 123:453–463, 2001. 15

J. Marz, C. Hah, and W. Neise. An experimental and numerical investigation into the mechanisms of rotating instability. *ASME: Journal of Turbomachinery*, 124: 367–375, 2002. 18

S. A. Meguid, R. H. Mao, and T. Y. Ng. FE analysis of geometry effects of an artificial bird striking an aeroengine fan blade. *International Journal of Impact Engineering*, 35:487–498, 2008. 24

G. L. Merrington. Fault diagnosis in gas turbines using a model-based technique. *ASME J. Eng. Gas Turbines Power*, 116:374–380, 1994. 25

S. R. Montgomery and J. J. Braun. Investigation of rotating stall in a single-stage axial compressor. *National Advisory Committee for Aeronautics*, Technical note 3823, 1957. 13

F. K. Moore and E. M. Greitzer. A theory of post-stall transients in axial compression systems: Part I-development of equations. *ASME J. Eng. for Gas Turbines and Power*, 108:68–76, 1986. 11

R. D. Moore and L. Reid. Performance of single-stage axial flow transonic compressor with rotor and stator aspect rotors of 1.19 and 1.26, respectively, and with design pressure ratio of 2.05. *NASA Technical Paper 1659*, 1:1, 1980. 34, 44

D. E. Muir, H. I. H. Saravanamuttoo, and D. J. Marshall. Health monitoring of variable geometry gas turbines for the Canadian navy. *ASME J. Eng. Gas Turbines Power*, 111:244–250, 1989. 25

T. Nakano, H. Kodama, and K. Imanari. Numerical simulations of instability inception and development in high-speed multi-stage axial-flow compressors. *ISOABE 99-7228*, 1999. 12

C. Nie. An experimental investigation on different radial loading distribution and patterns of stall inception in a single-stage low-speed axial compressor. *Proceedings of ASME Turbo Expo 2003 Power for Land, Sea, and Air*, 2003. 14

R. Niehuis, A. Bohne, and A. Hoynacki. Experimental investigation of unsteady flow phenomena in a three-stage axial compressor. *Proc. Instn Mech. Engrs Part A: J. Power and Energy*, 217:341–348, 2003. 100, 106, 118, 121

P. Nucara and A. I. Sayma. Effects of using hydrogen-rich syngas in industrial gas turbines while maintaining fuel flexibility on a multistage axial compressor design. *Proceedings of ASME Turbo Expo 2012*, 2012. 105

E. Outa, Y. Ohta, D. Kato, and K. Chiba. Two-dimensional study on evolution of deep rotating stall under uniform inlet conditions in an axial compressor cascade. *ISOABE*, 1999. 17

C. Peng. Numerical predictions of rotating stall in an axial multi-stage-compressor. *Proceedings of ASME Turbo Expo*, 2011. 25

G. Pullan, A. M. Young, I. J. Day, E. M. Greitzer, and S. Spakovszky. Origins and structure of spike-type rotating stall. *Proceedings of ASME Turbo Expo*, 2012. 23, 26, 73, 74, 125, 129, 147

L. Reid and R. D. Moore. Design and overall performance of four highly loaded, high-speed inlet stages for an advanced high-pressure-ratio core compressor. *NASA Technical Paper 1337*, 1978. 34

A. I. Sayma. Towards virtual testing of compression systems in gas turbine engines. *The NAFEMS International Journal of CFD Case Studies*, 1:1, 2009. 105

A. I. Sayma, M. Vahdati, and M. Imregun. An integrated nonlinear approach for turbomachinery forced response prediction. Part I: Formulation. *Journal of Fluids and Structures*, 14:87–101, 2000a. 31, 32

A. I. Sayma, M. Vahdati, and M. Imregun. Multi-bladerow fan forced response predictions using an integrated three-dimensional time-domain aeroelasticity model. *Proceedings of the Institution of Mechanical Engineers Part C - Journal of Mechanical Engineering Science*, 214(12):1467–1483, 2000b. 31

A. I. Sayma, M. Vahdati, L. Sbardella, and M. Imregun. Modelling of 3D viscous compressible turbomachinery flows using unstructured hybrid grids. *AIAA Journal*, 38(6):945–954, 2000c. 31

R. Schulze and D. K. Hennechke. Design of an active stall avoidance system for a subsonic axial compressor. *Design Principles and Methods for Aircraft Gas Turbine Engines*, 1998. 11

P. D. Silkowski. Measurements of rotor stalling in a matched and mismatched multistage compressor. *GTL Report No. 221, Massachusetts Institute of Technology, Cambridge, MA*, 1995. 71

A. K. Simpson and J. P. Longley. An experimental study of the inception of rotating stall in a single-stage low-speed axial compressor. *Porceedings of GT2007 ASME Turbo Expo 2007: Power for Land, Sea and Air*, 2007. 20

P. R. Spalart and S. R. Allmaras. A one equation turbulence model for aerodynamic flows. *30th Aerospace science meeting and exhibit*, pages AIAA paper 92–0439, 1992. 30

A. Stamatic, K. Mathioudakis, M. Smith, and K. Papailiou. Gas turbine component fault identification by means of adaptive performance modelling. *ASME Paper 90-GT-376*, 1990. 25

K. L. Suder. Blockage development in a transonic, axial compressor rotor. *NASA TM-113115*, 1997. x, 44, 49, 51, 52, 53

N. Tahara, M. Kurosaki, Y. Ohta, E. Outa, T. Nakakita, and Y. Tsurumi. Early stall warning technique for axial flow compressors. *Proceedings of ASME Turbo Expo 2004 Power for Land, Sea, and Air*, 2004. 11

B. Tu, J. Hu, and Y. Zhao. 3D unsteady computation of stall inception in axial compressors. *Proceedings of ASME Turbo Expo 2010: Power for Land, Sea, and Air*, 2010. 21

M. Vahdati, Sayma A. I., C. Freeman, and M. Imregun. On the use of atmospheric boundary conditions for axial-flow compressor stall simulations. *ASME: Journal of Turbomachinery*, 127:349–351, 2005. 58

M. Vahdati, G. Simpson, and M. Imregun. Unsteady flow and aeroelasticity behaviour of aeroengine core compressors during rotating stall and surge. *ASME: Journal of Turbomachinery*, 130, 2008. 25, 58, 151

H. D. Vo, Ch. S. Tan, and E. M. Greitzer. Criteria for spike initiated rotating stall. *ASME: Journal of Turbomachinery*, 130, 2008. 5, 15, 20, 21, 26, 73, 75, 146

P. P. Walsh and P. Fletcher. Gas Turbine Performance. *Blackwell Science*, 2nd ed.: p470, 2004. 3

S. Weichert and I. Day. Detailed measurements of spike formation in an axial compressor. *Proceedings of ASME Turbo Expo 2012*, 2012. 22, 26, 73, 147

X. Wu, M. Vahdati, A. I. Sayma, and Imregun M. A numerical investigation of aeroacoustic fan blade flutter. *Proceedings of ASME Turbo Expo 2003*, 2003. 59

Y. Wu, Q. Li, J. Tian, and W. Chu. Investigation of pre-stall behavior in an axial compressor rotor-Part 2: Flow mechanism of spike emergence. *Proceedings of ASME Turbo Expo 2011*, 2011. 22

K. Yamada, K. Funazaki, and H. Sasaki. Numerical investigation of relation between unsteady behavior of tip leakage vortex and rotating disturbance in a transonic axial compressor rotor. *Proceedings of ASME Turbo 2008: Power for Land, Sea and Air*, 2008. 16

K. Yamada, H. Kikuta, and K. Iwakiri. An explanation for flow features of spike-type stall inception in an axial compressor rotor. *Proceedings of ASME Turbo Expo 2012*, 2012. 23

J. Zhang, F. Lin, J. Chen, and Ch. Nie. A study of stall inceptions in a low-speed axial-flow compressor with various radial loadings. *Proceedings of ASME Turbo Expo 2009: Power for Land, Sea and Air*, 2009a. 15

J. Zhang, F. Lin, J. Chen, and Ch. Nie. The role of tip leakge flow in triggering

rotating stall of a low speed compressor under inlet distortion. *Journal of Thermal Science*, 18:33–39, 2009b. 15

Y. Zhang, X. Lu, W. Chu, and J. Zhu. Numerical investigation of the unsteady tip leakage flow and rotating stall inception in a transonic compressor. *Journal of Thermal Science*, 19:310–317, 2010. 71, 75